

2008/1 vol.5



ACTA GEO TECHNICA SLOVENICA

2008/1

A. S. Nossan

ADVANCES AND UNCERTAINTIES IN THE
DESIGN OF ANCHORED RETAINING WALLS
USING NUMERICAL MODELLING

s. škrabl.

THE LIMIT VALUES AND THE DISTRIBUTION
OF THREE-DIMENSIONAL PASSIVE EARTH PRESSURES

s. Lenart

THE RESPONSE OF SATURATED
SOILS TO A DYNAMIC LOAD

T. pliberšek & A. umek

GREEN'S FUNCTION FOR TANGENTIALLY LOADED
HORIZONTAL LAYERED HALF-SPACE

ISSN 1854-0171



**ACTA
GEOTECHNICA
SLOVENICA**

ISSN: 1854-0171

ustanovitelji

founders

Univerza v Mariboru, Fakulteta za gradbeništvo
University of Maribor, Faculty of Civil Engineering



Univerza v Ljubljani, Fakulteta za gradbeništvo in geodezijo
University of Ljubljana, Faculty of Civil
and Geodetic Engineering



Univerza v Ljubljani, Naravoslovnotehniška fakulteta
University of Ljubljana, Faculty of Natural
Sciences and Engineering



Slovensko geotehniško društvo
Slovenian Geotechnical Society



Društvo za podzemne in geotehniške konstrukcije
Society for Underground and Geotechnical
Constructions



Izdajatelj

publisher

Univerza v Mariboru, Fakulteta za gradbeništvo
University of Maribor, Faculty of Civil Engineering

odgovorni urednik

editor-in-chief

Ludvik Trauner
Univerza v Mariboru

urednika

co-editors

Stanislav Škrabl
Univerza v Mariboru
Bojan Žlender
Univerza v Mariboru

tehnična urednika

desk editors

Bojana Dolinar
Univerza v Mariboru
Borut Macuh
Univerza v Mariboru

lektor

proof-reader

Paul McGuinness

naklada

circulation

500 izvodov - issues

tisk

print

Tercia tisk d.o.o. Ptuj

Revija redno izhaja dvakrat letno. Članki v reviji so recenzirani s strani priznanih mednarodnih strokovnjakov. Baze podatkov v katerih je revija indeksirana: SCIE - Science Citation Index Expanded, JCR - Journal Citation Reports / Science Edition, ICONDA - The international Construction database, GeoRef
Pri financiranju revije sodeluje Javna agencija za raziskovalno dejavnost republike Slovenije.

uredniški odbor

editorial board

Darinka Battelino
Università degli Studi di Trieste
József Farkas
Budapesti Műszaki és Gazdaságtudományi Egyetem
Theodoros Hatzigogos
Aristotle University of Thessaloniki
Rolf Katzenbach
Technische Universität Darmstadt
Zlatko Langof
Univerzitet u Sarajevu
Jakob Likar
Univerza v Ljubljani
Janko Logar
Univerza v Ljubljani
Bojan Majes
Univerza v Ljubljani
Milan Maksimović
Univerzitet u Beogradu
Borut Petkovšek
Zavod za gradbeništvo Slovenije
Mihael Ribičič
Univerza v Ljubljani
César Sagaseta
Universidad de Cantabria
Stephan Semprich
Technische Universität Graz
Abdul-Hamid Soubra
Université de Nantes
Ivan Vaniček
České vysoké učení technické v Praze
Franjo Verič
Sveučilište u Zagrebu

naslov uredništva

address

ACTA GEOTECHNICA SLOVENICA
Univerza v Mariboru, Fakulteta za gradbeništvo
Smetanova ulica 17
2000 Maribor
Slovenija
Telefon / Telephone: +386 (0)2 22 94 300
Faks / Fax: +386 (0)2 25 24 179
E-pošta / E-mail: ags@uni-mb.si

spletni naslov

web address

<http://www.fg.uni-mb.si/journal-ags>

The journal is published twice a year. Papers are peer reviewed by renowned international experts. Indexation data bases of the journal: SCIE - Science Citation Index Expanded, JCR - Journal Citation Reports / Science Edition, ICONDA - The international Construction database, GeoRef
Financially supported also by Slovenian Research Agency.

VSEBINA

2	Ludvik Trauner UVODNIK
4	Antun Szavits Nossan NAPREDEK IN NEZANESLJIVOSTI PRI NUMERIČNEM MODELIRANJU SIDRNIH KONSTRUKCIJ
20	Stanislav Škrabl MEJNE VREDNOSTI IN RAZPOREDITEV 3D PASIVNIH ZEMELJSKIH PRITISKOV
36	Stanislav Lenart ODZIV ZASIČENIH ZEMLJIN NA DINAMIČNO OBREMENITEV
50	Tomaž Pliberšek in Andrej Umek GREENOVA FUNKCIJA TANGENCIALNO OBREMENJENEGA HORIZONTALNO SLOJEVITEGA POLPROSTORA
70	NAVODILA AVTORJEM

CONTENTS

Ludvik Trauner EDITORIAL	3
Antun Szavits Nossan ADVANCES AND UNCERTAINTIES IN THE DESIGN OF ANCHORED RETAINING WALLS USING NUMERICAL MODELLING	5
Stanislav Škrabl THE LIMIT VALUES AND THE DISTRIBUTION OF THREE-DIMENSIONAL PASSIVE EARTH PRESSURE	21
Stanislav Lenart THE RESPONSE OF SATURATED SOILS TO A DYNAMIC LOAD	37
Tomaž Pliberšek in Andrej Umek GREEN'S FUNCTION FOR TANGENTIALY LOADED HORIZONTALLY LAYERED HALF-SPACE	51
INSTRUCTIONS FOR AUTHORS	71

UVODNIK

Člani uredniškega odbora revije Acta Geotechnica Slovenica z veseljem sporočamo, da smo v petem letu izhajanja revije dosegli pomemben cilj, to je njeno vključitev v Thomsonovi bazi Science Citation Index Expanded in Journal Citation Reports/Science Edition, kjer sedaj poteka preverjanje člankov za določitev faktorja vpliva. Ob tej priliki se zahvaljujemo vsem, ki ste nas podpirali in vseskozi trdno verjeli v uspeh revije.

Druga novost je odločitev uredniškega odbora revije in vodstva Slovenskega geotehniškega društva (SloGeD), da bodo odslej teme vabljenih predavanj na Šukljetovih dnevih predstavljene v obliki člankov v reviji Acta Geotechnica Slovenica. Šukljetove dneve vsako leto organizira SloGeD v spomin na pionirja slovenske geotehnike, akademika prof. dr. Luja Šukljeta. V duhu tega velikega raziskovalca so izbrane tudi vsebine vabljenih predavanj. Doslej so bili na Šukljetove dneve povabljeni naslednji predavatelji iz tujine: M. Jamiolkowski (2000), G. Sanglerat (2001), D.D.Potts (2002), H. Brandl (2003), R. Katzenbach (2004), S. Semprich (2005), S. Leroueil (2006), D. Žnidarčič (2007) in A. Szavits Nossan (2008).

Pričujoča številka revije prinaša štiri zanimive prispevke avtorjev Antuna Szavits Nossana, Stanislava Škrabla, Stanislava Lenarta ter Tomaža Pliberška in Andreja Umeka.

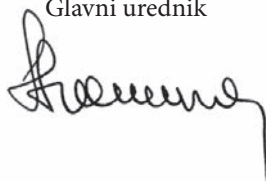
V prispevku A. Savitz Nossana je predstavljena možnost napovedovanja horizontalnih premikov in notranjih statičnih količin v sidranih podpornih konstrukcijah za zaščito izkopov z uporabo standardnih terenskih in laboratorijskih preiskav ter komercialnega programa s končnimi elementi. Slednji vsebuje konstitutivni model zemljine, ki simulira osnovne aspekte obnašanja tal na lokaciji gradbene jame.

Članek S. Škrabla obravnava izvirni pristop določanja kritične razporeditve in mejnih vrednosti pasivnih zemeljskih tlakov za tri-dimenzionalne primere po metodi mejne analize in teorema zgornje vrednosti. Za določanje kritične razporeditve pasivnih tlakov vzdolž višine podporne konstrukcije je uporabljena metoda mejne analize z množico tri-dimenzionalnih kinematično dopustnih hiperboličnih rotacijskih porušnih mehanizmov po metodi postopnega določanja intenzitete pasivnih tlakov od zgoraj navzdol.

Avtor tretjega prispevka S. Lenart predstavlja dva najbolj izrazita načina deformiranja dinamično obremenjenih zasičenih zemljin in sicer likvifikacijo s tečenjem in ciklično mobilnost. Oba pojava sta bila preiskana na meljnih peskih in prodno peščenih meljih, ki izhajajo z območja potopljenega nasipa železniške proge zaradi novozgrajenega akumulacijskega bazena na reki Savi v Boštanju in velikega plazju, ki se je sprožil na področju Stože v Julijskih Alpah.

Članek T. Pliberška in A. Umeka obravnava nov pristop k evalvaciji integralne predstavitve Greenove funkcije za slojevit pol-prostor, ki je na površini obremenjen s harmonično tangencialno točkovno silo.

Ludvik Trauner
Glavni urednik



EDITORIAL

I am very pleased to be able to report that Acta Geotechnica Slovenica has been selected for coverage in Thomson Reuters products and custom information services. Beginning with Vol.4 (1) 2007, Acta Geotechnica Slovenica will be indexed and abstracted in the Science Citation Index Expanded (also known as SciSearch®) and the Journal Citation Reports/Science Edition. I would like to take this opportunity to thank all of you who have supported us and contributed to the continued success of our journal.

Other news is the decision of journal's editorial board and the Slovenian Geotechnical Society (SloGeD) that the invited lectures of Šuklje's Days, which are organized every year by SloGeD in memory of the pioneer of Slovene geotechnics, academician professor Lujo Šuklje, will be published in Acta Geotechnica Slovenica. In this way the journal will have the opportunity to be the first to publish the results of these important scientific studies. The publication of the contents of the invited lectures in the form of papers is a great advantage for the authors also, who will now have the opportunity to acquaint a broader circle of interested readers with their achievements, since these articles can be found in the Thomson databases. In recent years, the invited lecturers on Šuklje's Days were M. Jamiolkowski (2000), G. Sanglerat (2001), D.D. Potts (2002), H. Brandl (2003), R. Katzenbach (2004), S. Semprich (2005), S. Leroueil (2006), D. Žnidarčič (2007) and A. Szavits Nossan (2008).

The first issue of Year 5 contains four interesting articles authored by Antun Szavits Nossan, Stanislav Škrabl, Stanislav Lenart, and Tomaž Pliberšek and A. Umek.

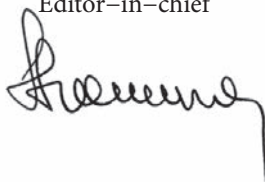
In his paper, A. Szavits Nossan presents a prediction of the horizontal displacements and the internal forces in an anchored wall for the protection of an excavation using standard field and laboratory tests and a finite-element program. The last of these includes a constitutive soil model that can simulate the key aspects of the soil's behaviour at a construction site.

The paper of S. Škrabl deals with a novel approach to the determination of the critical distribution and limit values of three-dimensional passive soil pressures acting on flexible walls, following the upper-bound method within the framework of the limit-analysis theory. The method of limit analysis with a set of three-dimensional cinematically admissible hyperbolic translational failure mechanisms is used to determine the critical distribution of the passive pressures along the retaining structure's height.

The author of the third paper, S. Lenart, treats the two most marked types of deformation behaviour for dynamically loaded saturated soil, i.e., flow liquefaction and cyclic mobility. Both phenomena were researched in silty sand and lacustrine carbonate silt, which are found in the area of a submerged railway line, due to the newly built Sava-river accumulation reservoir in Boštanj, and where the large landslide occurred in the Stože area of the Julian Alps.

The topic of the paper by T. Pliberšek and A. Umek is a novel evaluation of the integral representation of a surface Green's function for a layered half-space, loaded on its surface by a harmonic tangential point force.

Ludvik Trauner
Editor-in-chief



NAPREDEK IN NEZANESLJIVOSTI PRI NUMERičNEM MODELIRANJU SIDRANH PODPORNIH KONSTRUKCIJ

ANTUN SZAVITS NOSSAN

o avtorju

Antun Szavits Nossan
Univerza v Zagrebu,
Fakulteta za gradbeništvo
Kačićeva 26, 10 000 Zagreb, Hrvaška
E-pošta: szavits@grad.hr

izvleček

V članku je predstavljena možnost napovedovanja horizontalnih premikov in notranjih statičnih količin v sidranih podpornih konstrukcijah za zaščito izkopov z uporabo standardnih terenskih in laboratorijskih preiskav ter komercialnega programa s končnimi elementi. Slednji vsebuje konstitutivni model zemljine, ki simulira osnovne aspekte obnašanja tal na lokaciji gradbene jame. V prispevku je prikazano, da se mora uporabnik dobro seznaniti s konstitutivnim modelom vključenim v program ter da predstavlja odločilen del modeliranja izbira primernih parametrov zemljin za numerične analize. Za izbiro primernih parametrov za simulacijo dejanskih pogojev prisotnih med gradnjo je koristna izvedba numeričnih simulacij standardnih laboratorijskih preizkusov, ki jih je potrebno primerjati s poznanim obnašanjem zemljine.

V članku je prikazano, da izmerjene hitrosti strižnih valov, iz katerih lahko določimo strižno togost tal pri majhnih deformacijah, lahko uporabimo tudi za določitev statične togosti tal za velikosti deformacij obravnavane geotehnične konstrukcije, tako v koherentnih kot tudi nekoherentnih tleh.

Raziskovalno delo je bilo izvedeno za primer iz geotehnične prakse z detajlno analizo zaščite izkopa s sidrano armirano betonsko steno v relativno togi zemljini. Deformacije stene so bile merjene z vgrajenim inklinometrom.

Pretežni del članka predstavlja izbiro parametrov konstitutivnega modela, še posebej parametrov togosti tal. Za potrditev ocene zmanjšanja sekantnega deformacijskega modula zaradi povečanja mobilizirane strižne trdnosti za trde gline z objavljenimi empiričnimi odnosi iz literature je bila uporabljena simulacija triosnega konsolidacijskega nedreniranega preizkusa. Prikazano je, da je s takšno izbiro parametrov togosti v konstitutivnem modelu tal možno dobiti sprejemljivo napoved deformacij sidrane stene. Čeprav je predstavljen samo en primer uspešne analize, le ta daje vzpodbudo, saj prikazuje možnost relativno zanesljive napovedi deformacij samo na osnovi terenskih in laboratorijskih preizkusov in z uporabo razpoložljivih računalniških programov z realnim modelom zemljine.

ključne besede

sidrana stena, model tal, strižna togost, numerično modeliranje, merjene deformacije

ADVANCES AND UNCERTAINTIES IN THE DESIGN OF ANCHORED RETAINING WALLS USING NUMERICAL MODELLING

ANTUN SZAVITS NOSSAN

About the author

Antun Szavits Nossan
University of Zagreb,
Faculty of Civil Engineering
Kačićeva 26, 10 000 Zagreb, Croatia
E-mail: szavits@grad.hr

Abstract

This paper describes research on the prediction of horizontal displacements and internal forces in an anchored wall for the protection of an excavation, using standard field and laboratory tests and a finite-element programme with a soil model that can simulate the key aspects of soil behaviour at a construction site. It is important to be acquainted with the constitutive model incorporated in the programme, and the selection of the appropriate soil parameters for the numerical analysis is a crucial part of the modelling. As a result, it is useful to carry out numerical simulations of standard laboratory tests with well-known soil behaviour in order to select the relevant parameters for the simulation of the actual construction process.

It is shown in this paper that the measurements of the shear-wave velocities, which can provide the soil's stiffness at very small strains, can also be useful for determining the static stiffness at a magnitude of the strains relevant for the geotechnical structure under consideration, for both cohesive and noncohesive soils.

The research was carried out by a detailed analysis of a case history involving an anchored, reinforced concrete wall supporting the walls of an excavation in a relatively stiff soil. The wall displacements were monitored using an installed inclinometer.

The major part of the paper is devoted to an analysis of the selection of parameters, especially the stiffness parameters. The simulation of the triaxial, consolidated, undrained tests was used in order to assess the reduction of the secant stiffness modulus with an increase of the relative mobilized shear strength for the hard clay layer according to the published empirical evidence. It is shown that by selecting the appropriate stiffness parameters for the soil model used

in the numerical analysis, it is possible to get an acceptable prediction of the anchored-wall displacements. This is just one example of a successful analysis, but it is encouraging in the way that it shows how it is possible to make reliable predictions based on standard field and laboratory tests and with the use of an available computer programme with a realistic soil model.

Keywords

anchored wall, soil model, shear stiffness, numerical modelling, measured displacements

1 INTRODUCTION

Anchored, retained structures are often used as temporary protection for deep excavations in urban areas. Their role is to ensure the stability of the soil around the excavation and to prevent any damage to surrounding buildings that might be caused by the excavation. The successful design of such structures depends a great deal on a realistic solution to the interaction between the structure, the anchors and the soil, taking into consideration the mechanical characteristics of the surrounding soil as well as the manner and the sequence of the construction. Gaba et al. [1] gave an overview of the available numerical methods, together with an assessment of their advantages and drawbacks. A detailed solution to the interaction problems is becoming increasingly more accessible with the use of commercial, numerical tools based primarily on the finite-element method, which allows for the use of complex, constitutive soil models [2], [3]. There are, however, serious problems with the practical use of these tools. Schweiger [4] describes a detailed benchmarking experiment in which several experts were invited to numerically model the behaviour of an anchored diaphragm wall. The results were scattered over an alarmingly wide range, which is not acceptable in practice, due to the selection of different constitutive models and soil parameters. De Vos and Whenham [5] have shown the results of a survey among a large number of users of geotechnical

finite-element programmes that show the problems they were encountering. The first item on the list of problems is the determination of soil parameters (23% of answers), followed by the determination of the initial conditions in the soil, the selection of the constitutive soil model, the interpretation of the results, the numerical discretization, the boundary conditions and the selection of the type of analysis. The first three items represent the core of the geotechnical design, supported by numerical modelling, and so they appeared at the top of the list in more than 50% of the answers. Gaba et al. [1] state, among others, the following reasons for these problems: the inadequate constitutive models, where the simple ones are not realistic; the data on soil strength; the stiffness and initial stresses that are not of sufficient quality; the insufficient user experience with the particular programme; and the inadequate modelling of the undrained conditions in cohesive soils. They claim that "Ground movements cannot be predicted accurately. It is essential that optimum use is made of precedent in comparable conditions through the use of good-quality case-history data. Case-history-based empirical methods of prediction are to be preferred to the use of complex analyses, unless such analyses are first calibrated against reliable measurements of well-monitored comparable excavations and wall systems." In any case, finite-element analyses should be used with caution, but they remain the only tool in cases of unusual structures for which there is no comparable experience.

Studies in which complex numerical models are calibrated against the monitoring data of a case history can be helpful in resolving the above-mentioned problems related to the use of commercial finite-element programmes for geotechnical structures. This paper describes such a case history and the subsequent numerical modelling. The case history comprises an excavation protected by an anchored, retaining structure, of which there are several examples constructed recently in Zagreb, Croatia. Standard geotechnical investigations of average quality were carried out along with measurements of the shear-wave velocities with respect to depth. It was intended to use these measurements for the prediction of the anchored-wall displacements, based on the significance of this aspect of soil behaviour, which has recently gained attention [6], related to the soil-structure interaction [7] and particularly to the interaction of the soil with the anchored walls [8]. Shear-wave velocities provide a direct in-situ measure of the soil stiffness without the necessity to retrieve undisturbed soil samples or use problematic correlations. The anchored-wall displacements were monitored during construction, and the excavation was successfully completed. Subsequent numerical analyses were carried

out using the finite-element programme Plaxis V8 [9], which is widely used in Croatia. Its option of small strain was used in order to take advantage of the shear-wave velocity measurements and the resulting soil stiffness at very small strains. It was decided, for practical reasons, to use Plaxis V8, even though sophisticated analyses of anchored walls at small strains have been reported [10], but using a commercially unavailable programme.

Designers in Croatia are familiar with the use of Plaxis for modelling anchored structures. Their predictions of displacements based on the standard recommendations for the selection of soil parameters usually turn out as a significant overestimation in comparison with the measured wall displacements. As a result they use a higher soil stiffness, based on the argument of available data on similar structures in similar soils. This type of reasoning, which is not based on serious studies, makes the use of complex finite-element calculations questionable, because they do not seem to have a significant advantage over, for example, the method of a beam resting on elasto-plastic springs, where the springs' characteristics are determined empirically from displacement measurements on similar anchored walls.

2 THE CASE HISTORY

The excavation, 14.5 m deep, is located in a rapidly expanding commercial area in Zagreb, and is intended for the construction of underground storeys of a commercial building. An existing, old, brick house, sensitive to soil displacements, is located near to the excavation. A 17.5-m-high and 0.6-m-thick wall of reinforced concrete, embedded in the soil 4 m below the bottom of the excavation, provided protection. The wall was cast in place prior to the excavation works.

Three rows of BBR 1860/1660 pre-stressed ground anchors were installed at a horizontal distance of 2.5 m in each row. The upper, first row anchors consist of 4 strands of high-strength steel, 0.6" in diameter. The second and third row anchors consist of 5 strands. Each anchor in the first two rows was pre-stressed to 500 kN, whereas the anchors in the third row were pre-stressed to 650 kN. Inclinator measurements of the relative horizontal wall displacements were taken during the excavation works. The inclinometer tube was installed in the wall concrete along its whole height at the location of the brick house. The vertical excavation section with the wall and the neighbouring house is shown in Fig. 1.

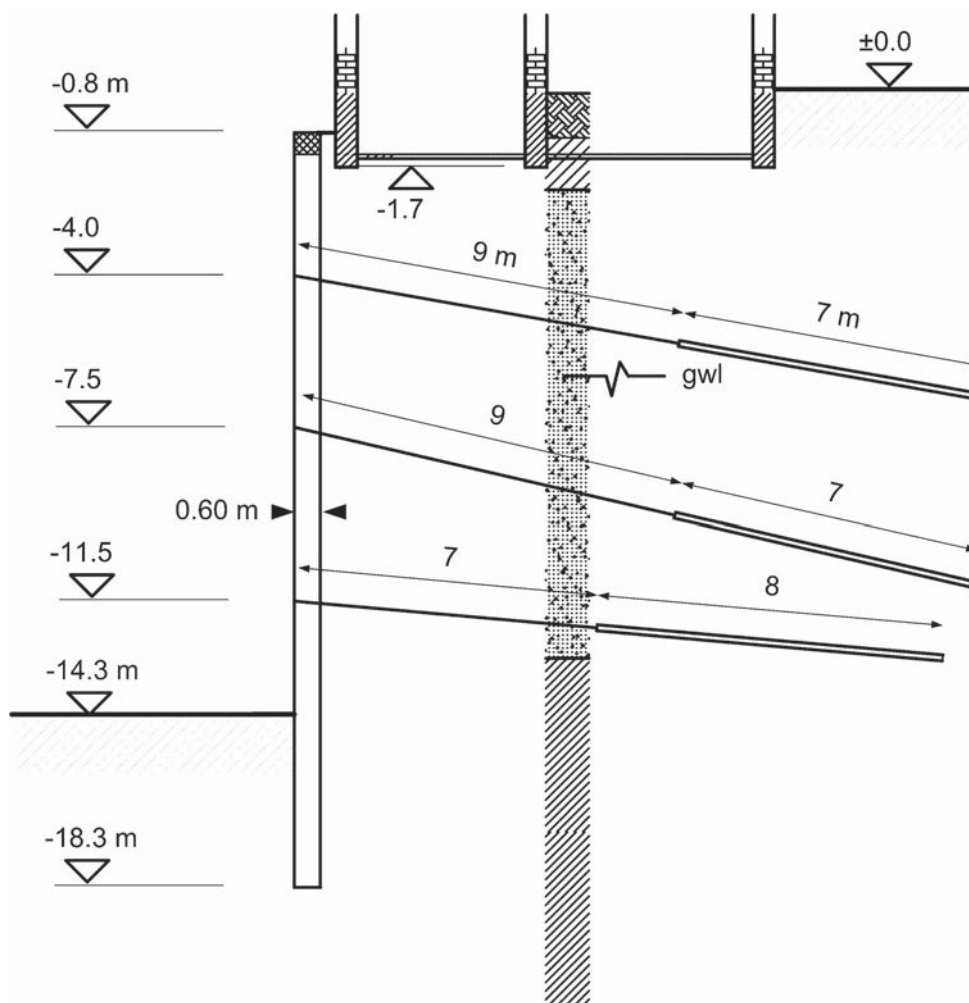


Figure 1. Vertical excavation section, reinforced concrete wall with three rows of anchors and the neighbouring brick house.

The ground surface at the location is horizontal and the underlying ground is horizontally layered. The surface layer is around 2 m thick and it consists of medium dense fill and clay underlain by a layer of poorly graduated medium dense gravel down to a depth of 14 m. Below this depth is a thick layer of hard, overconsolidated clay. The geotechnical field investigation was carried out in several 30-m-deep boreholes. Disturbed and undisturbed samples were retrieved and SPT measurements were taken. The shear-wave velocities were measured in two boreholes using the down-hole method. The underground water level was determined in the gravel layer at 7 m below the ground surface.

Standard classification tests were carried out in the laboratory on disturbed samples, and undisturbed clay samples were used for the triaxial, consolidated, undrained (CIU) and unconsolidated, undrained (UU) tests. The CIU tests were performed with pore-water

pressure measurements in order to determine the effective shear-strength parameters. The undrained shear strength was determined in the UU tests and with the use of a pocket penetrometer. The undisturbed clay samples were also used for oedometer tests. The results of the field and laboratory tests are presented in Fig. 2.

The SPT blow count N was corrected by the standard hammer impact energy of 60% and the normalized vertical effective stress, where $p^{\text{ref}} = 100$ kPa, according to Skempton [11]

$$(N_1)_{60} = N_{60} \sqrt{\frac{p^{\text{ref}}}{\sigma'_v}} \quad (1)$$

The full line in Fig. 2 represents the selected characteristic value of the design parameter $(N_1)_{60}$ according to Eurocode 7 [12]. The same characteristic value of

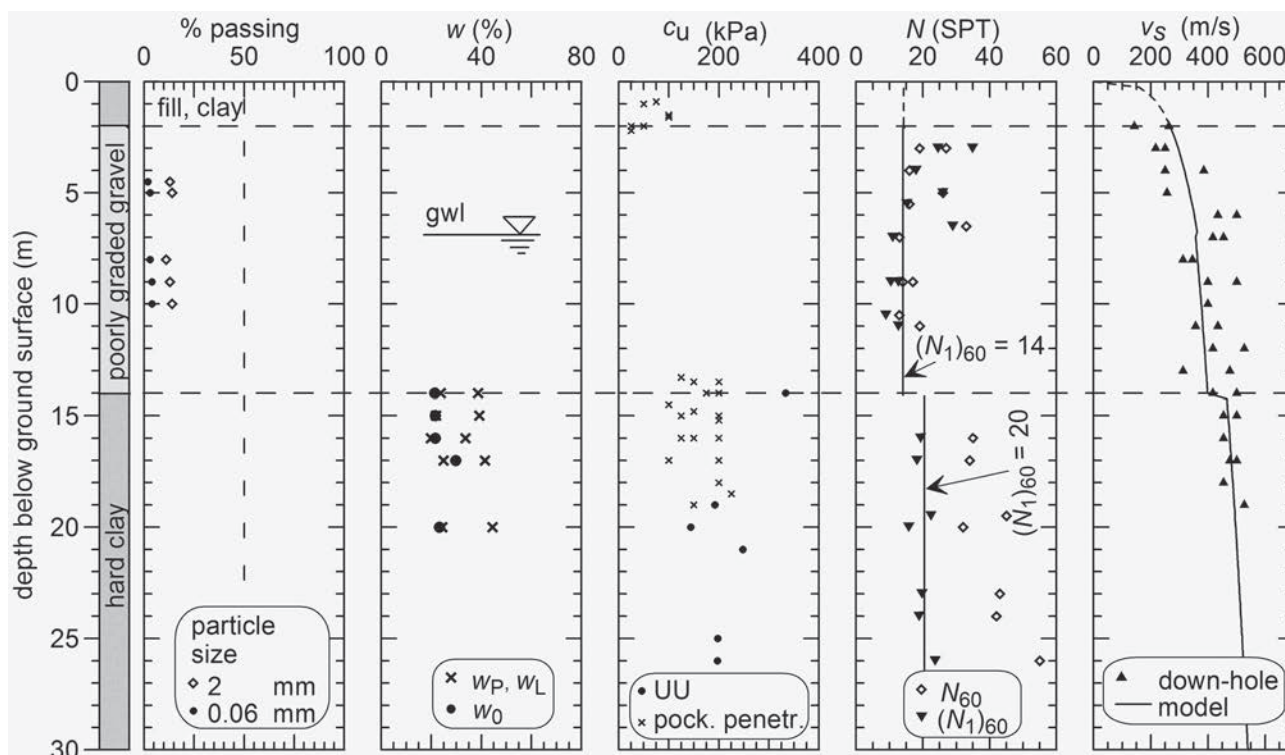


Figure 2. Soil profile with the fines and sand content in the gravel, the water content (w_0), the liquid limit (w_L) and the plastic limit (w_p), the undrained shear strength (c_u), the corrected SPT blow count (N_1 and $(N_1)_{60}$) and the shear-wave velocity (v_s).

this parameter was selected for the gravel for reasons of simplicity, even though a larger value could have been selected for the gravel above the water level. It also seemed reasonable to select a unique value of this parameter for the entire clay layer.

The characteristic value of the shear modulus for very small strains, G_0 , was determined from the shear-wave velocity through $G_0 = \rho v_s^2$, where ρ is the soil density. The distribution of this modulus with depth was assumed according to the following expression

$$G_0 = G_0^{\text{ref}} \sqrt{\frac{\sigma'_v}{p^{\text{ref}}}} \quad (2)$$

where G_0^{ref} is the reference shear modulus at a vertical effective stress of 100 kPa. Two distinct values of G_0^{ref} were allocated to the entire layers of gravel and clay. No such parameter was allocated to the thin surface layer because it was assumed that its influence on the behaviour of the anchored wall was negligible. The full line in Fig. 2 shows the design characteristic shear-wave velocities, which result from the above assumptions.

The characteristic value of the effective angle of internal friction φ' for the gravel layer was determined through the correlation with $(N_1)_{60}$ proposed by Hatanaka and Uchida [13]

$$\varphi'(^{\circ}) = 20^{\circ} + \sqrt{15.4 (N_1)_{60}} \quad (3)$$

which gives a characteristic value of $\varphi' = 35^{\circ}$ for $(N_1)_{60} = 14$. Even though this correlation was derived for sandy soils, there were no reliable data for gravel available.

The characteristic values of the effective cohesion, c' , and the effective angle of internal friction for the clay layer were determined by the interpretation of the triaxial CIU tests. The shear-strength parameters were selected at the point where the ratio of the major and minor principal effective stresses reaches a maximum. The test results and the selected values of the shear-strength parameters are shown in Fig. 3. The other characteristic parameter values depend on the selected soil model, and their determination will be described in the next section.

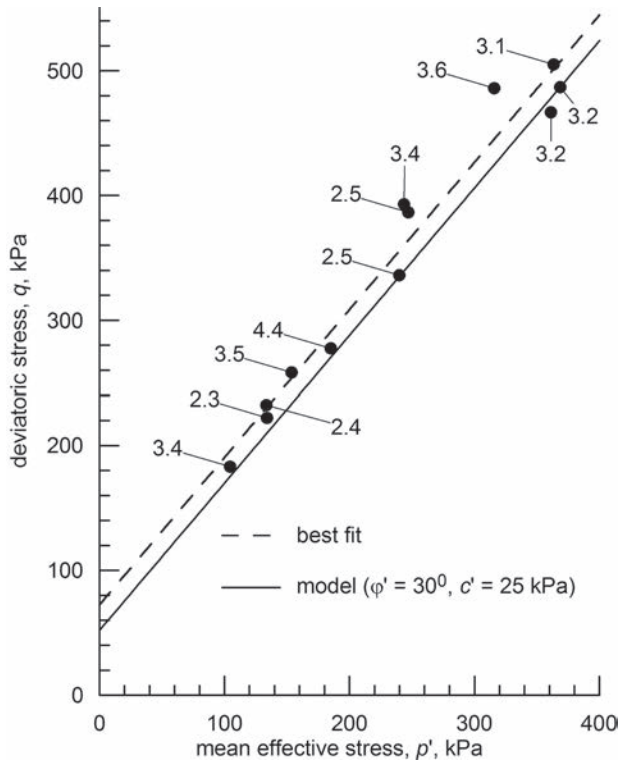


Figure 3. Clay shear-strength parameters from the results of the CIU tests and selected characteristic values. The numbers connected to the symbols represent the vertical strains ε_1 (%) at the maximum value of σ'_1/σ'_3 .

3 THE SOIL MODEL

The hardening-soil model with the option of using the soil stiffness at small strains was selected from the Plaxis V8 programme. This model is described in the programme manual [9] and in much more detail by Schanz et al. [14] and Benz [15]. It is described here only to the extent of explaining the selection of the required parameters. The original hardening model, which did not have the option for small strain stiffness, is described first.

This soil model is of the elasto-plastic isotropic hardening type with two hardening laws, each with its own yield surface and plastic potential. It satisfies the Mohr-Coulomb strength criterion with a constant effective cohesion c' and a constant effective angle of internal friction φ' . The first hardening law is related to shear (S) with a convex yield surface that crosses the Mohr-Coulomb envelope at the point where the deviatoric stress $q = 0$. It is used to model irreversible strains due to primary deviatoric loading. The second hardening law is related to the compression (C) and it is used to model irreversible plastic strains due to primary compression in the oedometer loading and the isotropic loading. When the loading phase results in the effective stress path reaching the two yield surfaces, they are “dragged” along with the stress path, thus producing both elastic and plastic strains. The development of the plastic

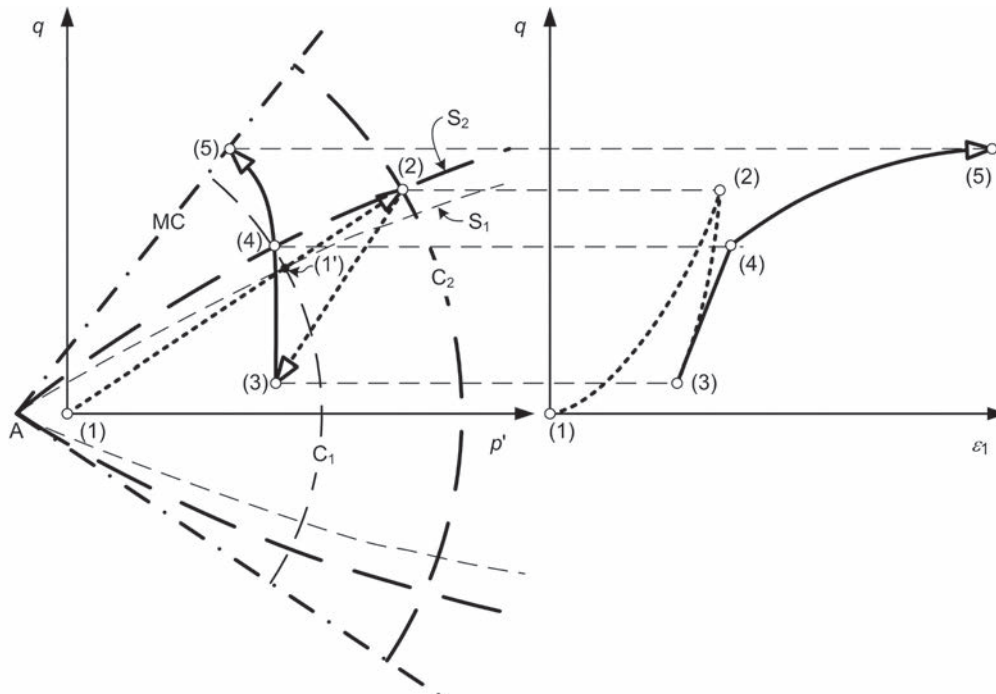


Figure 4. Stress path and yield surfaces for the hardening model from Plaxis V8 for a soil going through its geologic phases of sedimentation, overconsolidation and triaxial undrained shear.

strains significantly reduces the value of the tangent soil stiffness compared to its value in the elastic region. The yield surfaces do not move during the unloading phase; they remain at the previously reached location, bounding the elastic region, so that the resulting strains are fully elastic.

Fig. 4 shows the stress path and the yield surfaces for the hardening model from Plaxis V8 for a soil going through its geologic phases of sedimentation, overconsolidation and triaxial undrained shear; the last of these being such as the imposed loading to the geotechnical structure under consideration. The stress path in the left part of Fig. 4 is drawn in a (p', q) diagram, where p' and q are the effective stress invariants depending on the vertical, σ'_v , and horizontal, σ'_h , effective stresses. The mean effective stress $p' = (\sigma'_v + 2\sigma'_h)/3$ and the deviatoric stress $q = \sigma'_v - \sigma'_h$. MC denotes the Mohr-Coulomb envelope; S_1 and S_2 are two positions of the shear yield surface; and C_1 and C_2 are two positions of the compression yield surface. During sedimentation the soil follows the stress path from point (1) to point (2). When it is at the point (1'), for example, on yield surfaces C_1 and S_1 , both the yield surfaces are “dragged” with the stress path to the new positions denoted by C_2 and S_2 to the point (2). The geologic unloading from point (2) to point (3) leads to the actual overconsolidated state of the soil. The yield surfaces remain at their positions C_2 and S_2 . The undrained shear phase is shown by the stress path from point (3) to point (5). At point (4) it reaches the yield surface S_2 , thus producing plastic deformations and a reduction of the soil stiffness, which is demonstrated in the right part of Fig. 4 by a significant increase in the vertical deformation ε_1 from point (4) to point (5).

The slope of the Mohr-Coulomb envelope for triaxial compression is given by

$$M = \frac{6 \sin \varphi'}{3 - \sin \varphi'} \quad (4)$$

and the envelope crosses the p' axis at the point with the coordinate

$$p' \Big|_{q=0} = -\frac{c'}{\tan \varphi'} \quad (5)$$

This complex behaviour is, however, governed by the soil parameters, which are familiar in geotechnical practice. The user has to define the Mohr-Coulomb strength parameters c' and φ' , the angle of dilatancy at the drained failure ψ , the three reference values of the Young's modulus, the power coefficient for the determination of the soil stiffness, and some additional

advanced parameters, which can be left at their default settings.

Rowe's stress-induced dilatancy theory is used in the model for the determination of the volumetric plastic strains during shear loading. According to this theory, the material behaviour is governed by the critical state friction angle φ_{cv} , which is the slope of the Mohr-Coulomb envelope corresponding to the critical state line in the (p', q) diagram. The material contracts for the values of the mobilized friction angle smaller than φ_{cv} , whereas it dilates for values higher than φ_{cv} . At the point of failure, the mobilized friction angle equals φ' , and the angle of dilatancy is determined from

$$\sin \psi = \frac{\sin \varphi' - \sin \varphi_{cv}}{1 - \sin \varphi' \sin \varphi_{cv}} \quad (6)$$

The soil stiffness is determined through the reference values of E_{ur}^{ref} for the elastic stiffness, E_{50}^{ref} for the secant stiffness at 50% of the mobilized compressive strength in the standard drained triaxial test, and E_{oed}^{ref} for the tangent oedometer modulus during the loading of a normally consolidated soil in an oedometer test. These reference values are related to the reference confining the effective stress $\sigma'_3 = p^{ref} = 100$ kPa. The values of the three Young's moduli for different confining effective stresses are defined by

$$E_{ur} = E_{ur}^{ref} \left(\frac{c' \cos \varphi' + \sigma'_3 \sin \varphi'}{c' \cos \varphi' + p^{ref} \sin \varphi'} \right)^m \quad (7)$$

$$E_{50} = E_{50}^{ref} \left(\frac{c' \cos \varphi' + \sigma'_3 \sin \varphi'}{c' \cos \varphi' + p^{ref} \sin \varphi'} \right)^m \quad (8)$$

$$E_{oed} = E_{oed}^{ref} \left(\frac{c' \cos \varphi' + \sigma'_3 \sin \varphi'}{c' \cos \varphi' + p^{ref} \sin \varphi'} \right)^m \quad (9)$$

where m is the power coefficient defined by the user.

The advanced parameters include Poisson's ratio, ν_{ur} , for which the default value is set at 0.2, which corresponds to numerous published recommendations, the coefficient of the earth pressure at rest for normally consolidated soil K_0^{nc} , with the default value determined from $K_0^{nc} = 1 - \sin \varphi'$, and the failure ratio R_f with the default value of 0.9.

The basic idea for the formulation of the hardening-soil model is the hyperbolic relationship between the vertical strain ε_1 and the deviatoric stress q during the standard

isotropically consolidated drained shear, which can be approximated by

$$\varepsilon_1 \approx \frac{2-R_f}{2E_{50}} \frac{q}{1-\frac{q}{q_a}} \quad (10)$$

where q_a is the asymptotic value of the shear strength, related to the deviatoric stress at failure, q_f , through $q_a = q_f/R_f$, and the deviatoric stress at failure is defined by

$$q_f = (c \cot \varphi' + \sigma'_3) \frac{2 \sin \varphi'}{1 - \sin \varphi'} \quad (11)$$

The recently developed new version of the Plaxis programme has the possibility to model the soil stiffness at small strains. This option requires two additional soil parameters, the reference shear modulus at very small strains, G_0^{ref} , and the reference shear strain, $\gamma_{0.7}$. The first parameter serves for a determination of the shear modulus at very small strains G_0 through

$$G_0 = G_0^{\text{ref}} \left(\frac{c' \cos \varphi' + \sigma'_1 \sin \varphi'}{c' \cos \varphi' + p^{\text{ref}} \sin \varphi'} \right)^m \quad (12)$$

The reference shear strain is the value of the shear strain attained when the shear modulus, G_0 , reduces to 70% of its initial value. The Plaxis manual recommends the following expression for its determination

$$\gamma_{0.7} = \frac{1}{9G_0} [2c'(1 + \cos 2\varphi') + \sigma'_1(1 + K_0) \sin 2\varphi'] \quad (13)$$

where K_0 is the coefficient of the earth pressure at rest. K_0 and the overconsolidation ratio OCR may be defined by the user in order to define the initial stresses.

4 DETERMINATION OF THE SOIL PARAMETERS AND THE INITIAL STRESS STATE

Due to the complex constitutive relationship used in the numerical modelling, the determination of the soil parameters for the hardening-soil model deserves special attention. The intention in this research was to use those parameters that were readily available, either from tests and measurements performed at the construction site and in the laboratory or from correlations published in the literature. It has to be emphasized that the parameters were not adjusted so as to get the best agreement between the measured and the calcu-

lated displacements for a class-C prediction, after the completion of construction, instead, they were selected as if a class-A prediction were to be made prior to the construction.

The determination of the parameters for the hard clay layer is described first, because it required an analysis in both the drained and the undrained conditions, as the two limiting states for the development of the deformations. The undrained conditions are required because of the clay's low permeability and the high rate at which the excavation proceeded.

For the undrained conditions, the designer can make a total stress analysis with the determined, undrained shear strength, or an effective stress analysis with the requirement that there are no volumetric strains during the excavation. The second approach was chosen for this research because it was estimated that the undrained shear strength of the hard clays, determined in laboratory tests on undisturbed samples, is not sufficiently reliable because such samples might contain fissures. These fissures lead to an unrealistically fast consolidation and, thus, a too fast transition from the undrained to the drained state. This approach is on the safe side and it represents a cautious estimate of the characteristic values in terms of Eurocode 7 [12].

The hardening-soil model is, however, very limited in terms of the choice of the effective stress analysis in undrained conditions. This is especially so for hard, overconsolidated clays, for which the undrained shear strength is larger than the drained shear strength. The soil parameters that successfully model the shear strength and the dilatancy characteristics in drained conditions lead to an unrealistic, extremely large, undrained shear strength. The only way to avoid this is to set the angle of dilatancy $\psi = 0$ for the hard clay, which ensures that the material volume does not change during the shear loading at the drained failure. The result is a significantly lower undrained shear strength for the numerical model than the one determined from laboratory tests, as shown in Fig. 5. Curve (1) represents the assumed effective stress path in undrained conditions from the initial state at point A to failure at point B1 on the Mohr-Coulomb envelope (MC) in the grey area, which shows the range of measured values for the undrained shear strength in the UU tests. Curve (2) is the effective stress path in undrained conditions, from the initial state to the failure at point B2 for the hardening-soil model with an angle of dilatancy $\psi = 0$. Curve (3) is the effective stress path in drained conditions for the idealized case of Rankine active pressures on the wall. It is obvious from Fig. 5 that the stress path (2) gives a much lower value for the undrained shear

strength than the stress path (1). The same holds true for the passive state.

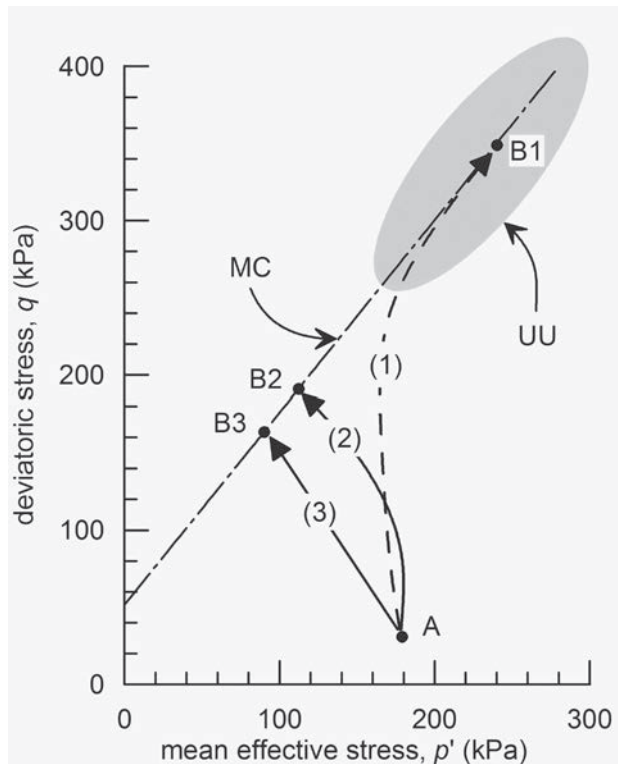


Figure 5. Effective stress paths for the hard clay.

Oedometer tests on samples of hard clay, the values of measured undrained shear strength, and the correlation between the preconsolidation pressure and the measured shear-wave velocities after Mayne et al. [16]

$$\sigma_p \text{ (kPa)} = 0.106 [v_s \text{ (m/s)}]^{1.47} \quad (14)$$

all indicate that the hard clay is overconsolidated with an overconsolidation ratio $2 \leq OCR = \sigma_p / \sigma'_v \leq 4$, where the larger values correspond to the upper parts of the clay layer. The value of $OCR = 3$ was adopted for the numerical analysis.

With the use of Jaky's expression $K_0^{nc} = 1 - \sin \varphi' = 0.5$, the coefficient of the earth pressure at rest was determined according to the recommendation by Mayne and Kulhawy [17]

$$K_0 = K_0^{nc} OCR^{\sin \varphi'} \quad (15)$$

which gives $K_0 = 0.87$ for the hard clay.

The selection of the stiffness parameters for the hard clay was not so straightforward. The starting point was the determination of the shear modulus at very small strains from the measured shear-wave velocities. The comparison of the values of G_0 obtained in this way with equation (12) gave $m = 0.5$ and $G_0^{ref} = 308 \text{ MPa}$.

The reduction of the initial shear modulus at very small strains with increasing strain values was the most demanding part of the parameter determination. It was not possible to deduce this reduction from the triaxial tests because the strains were not measured directly on the sample. Even though there are many published triaxial test results with measurements of small strains, few of them cover the entire strain range, from very small strains to the point of failure. As a result, it was decided to use the recommendations given by Mayne et al. [16], who suggest the following secant modulus E reduction with the increase of the deviatoric stress q

$$\frac{E}{E_0} = 1 - \left(\frac{q}{q_f} \right)^g \quad (16)$$

where the parameter g should be in the range $0.2 \leq g \leq 0.4$. This range is shown in Fig. 6 by the grey area. Fig. 6 also shows the curves resulting from the different numerical simulations for the hard clay in the process of determining the clay's stiffness parameters, which will be commented on in the following paragraphs.

The next step was to select the value of the parameter E_{50}^{ref} , and the research of Stroud (after Clayton [17]) was used for this purpose. According to this research, the values of the ratio E' / N_{60} for $q / q_f = 0.5$ are in the range between 1 and 2 for normally consolidated and overconsolidated clays and sands. If it is assumed that $E' \approx E_{50}$, it follows that the values of the ratio $E_{50}^{ref} / (N_1)_{60}$ are within a similar range, because, according to equations (1) and (8), the square root of K_0 is also involved in the ratio, but its value is close to 1. From Fig. 2, $(N_1)_{60} = 20$ for the hard clay, so that $E_{50}^{ref} = 40 \text{ MPa}$ was taken as the first choice.

The Plaxis manual recommends using $E_{oed}^{ref} = E_{50}^{ref}$, and with the selection of $E_{ur}^{ref} = 2E_{50}^{ref}$, which is close to the initial modulus for the hyperbolic relationship given by equation (10), the simulation of the isotropically consolidated undrained triaxial test can be carried out with $OCR = 3$ and an initial isotropic stress of 200 kPa. This stress value approximately corresponds to the vertical effective stress just below the interface between the gravel and the hard clay layers. The undrained modulus of elasticity at very small strains was determined from

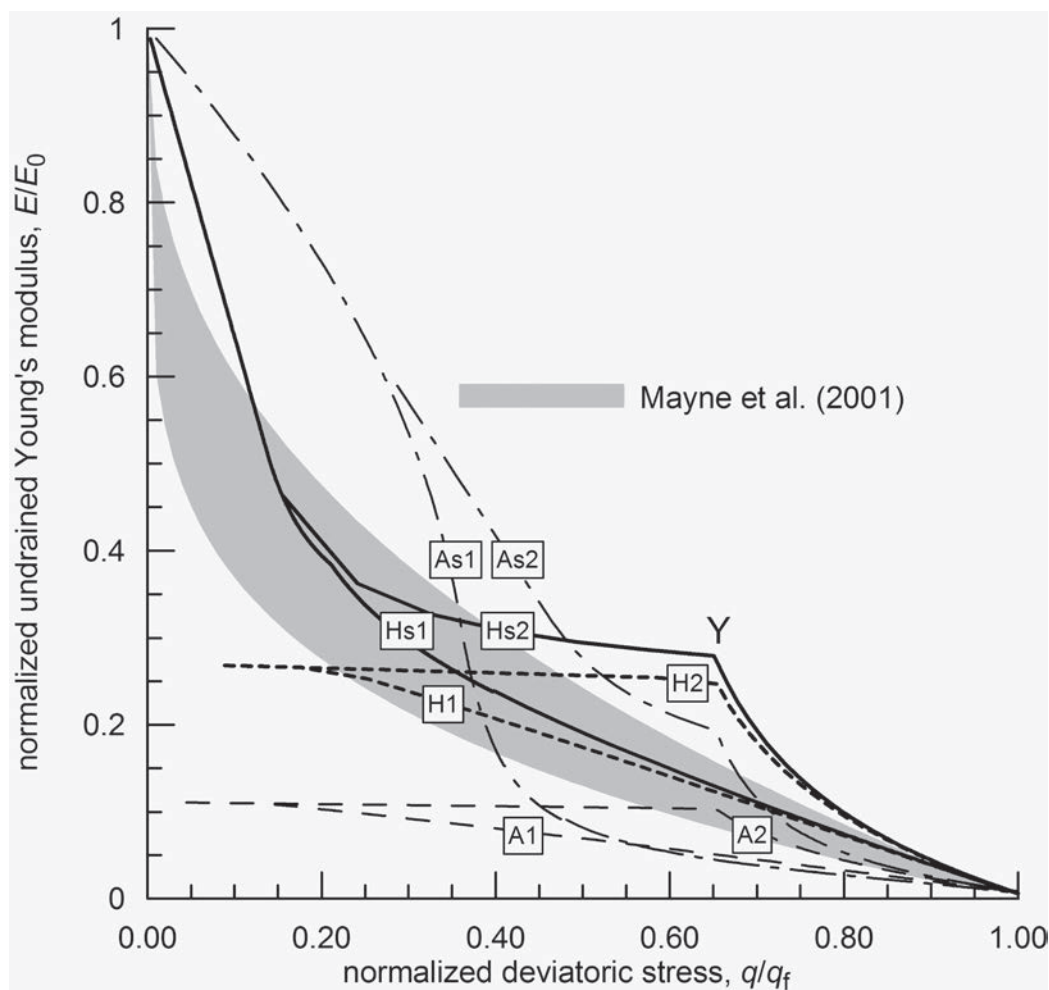


Figure 6. Reduction of the normalized secant modulus E/E_0 with the increase of the normalized deviatoric stresses in undrained conditions after Mayne et al. [16], and different numerical simulations for the hard clay.

$$E_0 = 2G_0(1 + \nu) \quad (17)$$

with $\nu = 0.5$.

This simulation with the hardening-soil model, which did not include the behaviour at small strains, gives the secant modulus reduction curve denoted by A1 in Fig. 6. Curve A2 shows a similar simulation in which the soil is anisotropically consolidated, the state closer to the one at the construction site. It is obvious from Fig. 6 that both curves, A1 and A2, are well below the grey area recommended by Mayne et al.

When the option for small strains is included, with the reference shear strain $\gamma_{0.7} = 10^{-4}$ according to equation (13), as recommended in the manual, curve As1 is

obtained for the isotropic consolidation and curve As2 for the anisotropic consolidation. Again, both curves depart from the recommendations in the grey area, which resulted in the rejection of the first selected value of E_{50}^{ref} .

The second choice of E_{50}^{ref} was made with the aim to obtain a match between the simulated, consolidated, undrained triaxial test results and the recommendations by Mayne et al. The first value of E_{50}^{ref} was multiplied by a factor of 2.5, giving $E_{50}^{\text{ref}} = 100 \text{ MPa} \approx G_0^{\text{ref}} / 3$, with $E_{\text{oed}}^{\text{ref}} = E_{50}^{\text{ref}}$, $E_{\text{ur}}^{\text{ref}} = 2E_{50}^{\text{ref}}$. Curve H1 in Fig. 6 was now obtained with the hardening-soil model, which did not include the behaviour at small strains, for the isotropic consolidation, and curve H2 for the anisotropic consolidation. For the small strain analysis, the

recommended equation (13) was not applied for the determination of the reference shear strain, but a value of $\gamma_{0.7} = 2 \cdot 10^{-5}$ was chosen instead. Curve Hs1 was the result for the isotropic consolidation and curve Hs2 for the anisotropic consolidation. These two curves provide a much better comparison with the Mayne et al. grey area, particularly the curve for the isotropic consolidation.

The deviations of the curve Hs2 from the grey area, with a sharp break at point Y, are the consequences of the characteristics of the hardening-soil model, i.e., the values of q/q_f lower than the one at point Y are below the yield surface S2 in Fig. 4. At point Y, the stress path reaches this yield surface at point (4) from Fig. 4, after which, it was shown, the reduction of stiffness occurs all the way to the point of failure when q/q_f equals 1. Even though similar research could not be found in the literature, it is not likely that the break at point Y reflects the actual soil behaviour. It seems more likely that the real Hs2 curve passes much closer to the grey area. It is interesting to note that a similar approach for the determination of the modulus reduction as a function of q/q_f was adopted by Mayne [19] for the calculation of settlements of spread foundations. They reported good agreement with the observed settlement of the experimental foundation.

The additional verification of the validity of the numerical simulations was carried out by comparing calculated vertical strains ε_1 with the values measured in laboratory triaxial tests. It was noted that in simulated triaxial tests, where the behaviour at small strains was not included (curves H1 and H2 in Fig. 6), the vertical strains at the point of failure, defined by the maximum value of the ratio σ'_1/σ'_3 , differ by a small margin from the results of the simulated triaxial tests with small strains (curves Hs1 and Hs2). This means that the small strain behaviour in the range $0 \leq q/q_f \leq 0.2$, where the modulus reduction is most important, does not have a significant influence on the strains close to the point of failure. Even though there are significant differences between curves H1 and H2, on the one hand, and Hs1 and Hs2 on the other, the anisotropic consolidation does not dominate over the isotropic consolidation for strains at the point of failure.

The calculated vertical strains at the point of failure for curves H1, H2, Hs1 and Hs2 are in the range between 2.8% and 3.2%. This is in very good agreement with the measured strains in the laboratory triaxial tests, which were in the range between 2.4% and 4.4% (Fig. 3). This is another indicator that the numerically simulated hard clay behaviour was within the measured values.

The stiffness parameters for the poorly graded gravel were determined in a similar way as for the hard clay, except for the dilatancy during shear, which was not disregarded. The gravel dilatancy was estimated based on the assessment of its critical state friction angle φ_{cv} which, in turn, was determined through the roundness parameter R . For predominantly sub-rounded to rounded grains, $0.5 \leq R \leq 0.7$, and by using the correlation suggested by Santamarina and Cho [20]

$$\varphi_{cv} (^{\circ}) = 42^{\circ} - 17R \quad (18)$$

With the use of equation (6), the angle of dilation $\psi = 6^{\circ}$.

It was also estimated that due to its geologic age in the zone of strong local seismicity (IXth zone of the MCS intensity scale), the gravel would probably exhibit preconsolidation characteristics. It was just assumed that the preconsolidation ratio has a value of $OCR = 2$. The coefficient of the earth pressure at rest could then be calculated from equation (15) as $K_0 = 0.6$. The effect of the selection of the assumed values was tested, and it turned out that the influence of the value of OCR on the wall displacements was negligible, which was not the case for the hard clay.

$G_0^{\text{ref}} = 226 \text{ MPa}$ was determined from the measured shear-wave velocity with $m = 0.5$. The other stiffness parameters were determined using the same equations as for hard clay, $E_{50}^{\text{ref}} = 75 \text{ MPa} \approx G_0^{\text{ref}} / 3$, $E_{\text{ocd}}^{\text{ref}} = E_{50}^{\text{ref}}$ and $E_{\text{ur}}^{\text{ref}} = 2E_{50}^{\text{ref}}$.

Table 1 lists the user-provided gravel and hard-clay parameters for the numerical analysis using the hardening-soil model, and Table 2 gives the parameters for the calculation of the initial stresses.

It is interesting to note that for both the gravel and the hard clay, the following two ratios gave approximately the same values

$$\frac{E_{50}^{\text{ref}} (\text{MPa})}{(N_1)_{60}} \approx 5 \text{ MPa} \quad (19)$$

$$\frac{G_0^{\text{ref}} (\text{MPa})}{(N_1)_{60}} \approx 15 \text{ MPa} \quad (20)$$

Since the top fill layer is of small thickness, it was disregarded in the analysis in a way that it was assumed that the gravel layer extended from the ground surface.

As for the required parameters for the supporting wall and anchors, the modulus of elasticity of the reinforced

Table 1. Soil parameters for the analysis with the hardening-soil model.

Parameter	Symbol	Unit	Value	
			gravel	hard clay
Reference stress	P_{ref}	kPa	100	
Saturated density	ρ_{sat}	kN/m ³	21	21
Density above GWL	ρ_{unsat}	MkN/m ³	20	21
Permeability	k	m/day	100	10 ⁻⁴
Reference Young's modulus at 50% mobilized strength	E_{50}^{ref}	Mpa	75	100
Reference oedometer modulus	E_{oed}^{ref}	Mpa	75	100
Reference elastic Young's modulus	E_{ur}^{ref}	Mpa	150	200
Elastic Poisson's ratio (effective)	ν_{ur}	-	0.2	0.2
Power coefficient	m	-	0.5	0.5
Effective cohesion	c'	kPa	2	25
Effective friction angle	φ'	degree	35	30
Angle of dilatancy at drained failure	ψ	degree	6	0
Coefficient of earth pressure at rest (normally consolidated soil)	K_0^{nc}	-	0.426	0.5
Failure ratio	R_f	-	0.9	0.9
Tension cut off	-	-	yes	yes
Reference shear strain	$\gamma_{0.7}$	-	2 · 10 ⁻⁵	2 · 10 ⁻⁵
Reference small strain shear modulus	G_0^{ref}	Mpa	226	308

Table 2. Soil parameters for the initial stress state.

Parameter	Symbol	Unit	Value	
			gravel	hard clay
Coefficient of earth pressure at rest	K_0	-	0.6	0.87
Overconsolidation ratio	OCR	-	2	3
Depth of phreatic surface	-	m	-7	-7

concrete was taken as $E_{ic} = 2.5 \cdot 10^4$ MPa, and the design concrete section bending resistance at the occurrence of a plastic hinge as $M_{Rd} = 0.4$ MNm/m according to Eurocode 7. The anchor modulus of elasticity was taken as $E_s = 1.95 \cdot 10^5$ MPa, the stiffness of the anchors with four strands as $E_s A = 1.17 \cdot 10^2$ MN, and those with five strands as $E_s A = 1.46 \cdot 10^2$ MN. The design anchor resistance to steel extension was taken as $R_{ad} = 0.844$ MN for the anchors with four strands and $R_{ad} = 1.06$ MN for the anchors with five strands.

5 SIMULATION OF THE CONSTRUCTION AND THE COMPUTED DISPLACEMENTS

The soil-structure interaction was analysed in phases that simulated the real construction stages. After the calculation of the initial stresses and the pore-water pressures was completed, the excavation was simulated as shown in Table 3. The load of the neighbouring house was estimated to be 720 kN/m, uniformly distributed on strip foundations and acting vertically. Each excavation phase, except for the last one, was subdivided into two parts, the first part comprising the excavation to the

Table 3. Construction calculation phases.

No.	Phase	Depth below ground level m	Anchors	
			Pre-stressing force (kN)	Spacing (m)
0	initial state	-	-	-
0a	load from the adjacent house	-1.7	-	-
1	excavation	-5	-	-
1a	anchor pre-stressing	-4	500	2.5
2	excavation	-8	-	-
2a	anchor pre-stressing	-7.5	500	2.5
3	aexcavation	-12	-	-
3a	anchor pre-stressing	-11.5	650	2.5
4	excavation	-14.3	-	-
5	consolidation	-	-	-

selected depth, and the ground-anchor pre-stressing in the second part. Drained conditions were assumed for the gravel layer and undrained conditions were assumed for the hard clay layer in all the construction phases.

As the excavation reached under the underground water level, the water level was lowered to the bottom of the excavation and the pore-water pressures were calculated as

$$u = u_0 + u_e \quad (21)$$

where u_0 are the pressures due to seepage and u_e are the excess pore pressures developed in undrained conditions. For drained conditions in gravel $u_e = 0$ at all times. The last calculation phase consisted of consolidation to the fully drained state in all the soil layers. The time development of the consolidation process was not simulated because of the unreliable data on the coefficient of consolidation. No measurements of pore-water pressure in the clay were taken during the construction.

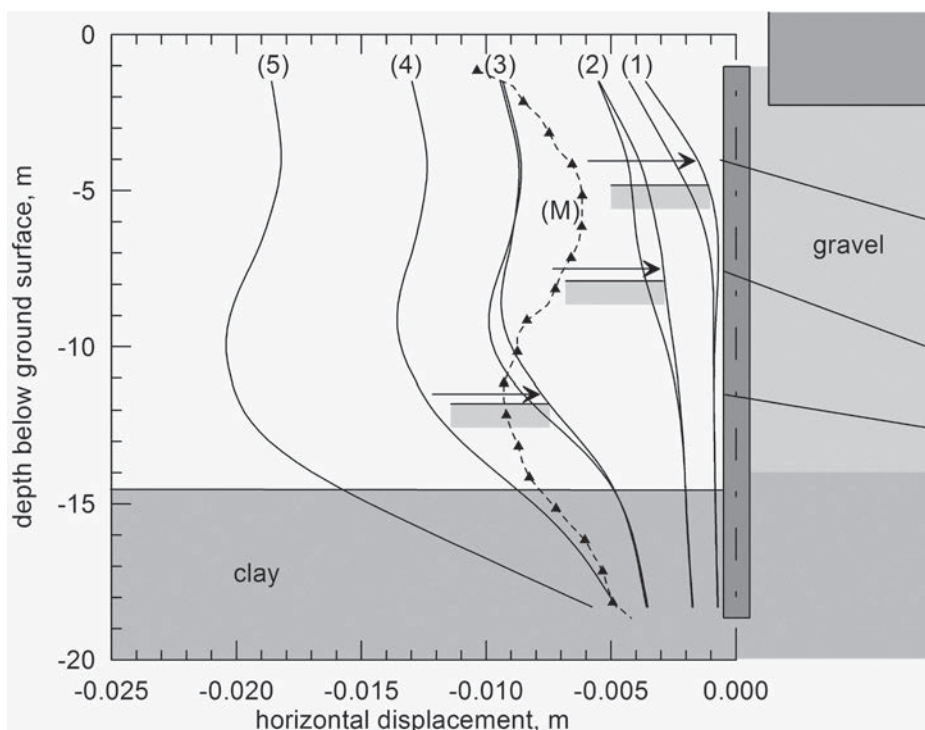


Figure 7. Calculated horizontal wall displacements in phases and measured displacements (M).

Fig. 7 shows the calculated development of the horizontal displacements of the anchored wall in phases denoted by the numbers in the brackets. The analysis was performed with the hardening-soil model and the small strains. The measured relative horizontal wall displacements after the last excavation phase are also shown by the curve (M). These displacements are relative because the inclinometer does not record the rigid-body wall translation. Thus, the bottom measured value is attached to curve (4) for undrained conditions after the completion of the excavation because it is assumed that the measured displacements occurred in such conditions.

The calculated displacements in phase 4 deviate significantly from the measured displacements. However, the calculated shape of the wall bending seems to be well in accordance with the measured one. Also, when the deviations are regarded in the light of the parameter-selection process and the generally negative experience in the prediction of displacements, then the obtained calculation results do seem to be encouraging and, from the point of view of the designer, acceptable. This particularly holds true when the fact that the displacement prediction was simulated on the basis of the available data and literature, and not actually a class-C prediction, is taken into account.

It has, however, to be noted that the measured displacements indicate the wall is bending more than the calculations are showing. This means that savings on the reinforcement of the wall should not be made.

Fig. 8 shows the comparison of the wall horizontal displacements calculated with (full lines) and without (dashed lines) small strains near and after the completion of the excavation. The differences between the corresponding curves with and without small strains are not significant, which might appear surprising, but previously described simulations of triaxial, consolidated, undrained tests showed that vertical strains at the point of failure do not differ much between the two options, which explains the results in Fig. 8. The generalization of these results would lead to the conclusion that for practical purposes it is not necessary to include the soil behaviour at small strains for similar walls and similar ground conditions. However, the shear modulus at very small strains is still the most important parameter for the determination of other stiffness parameters. If it were not used, the accurate prediction of wall displacements would not have been feasible. This fact emphasizes the importance of measuring the shear-wave velocity *in situ*.

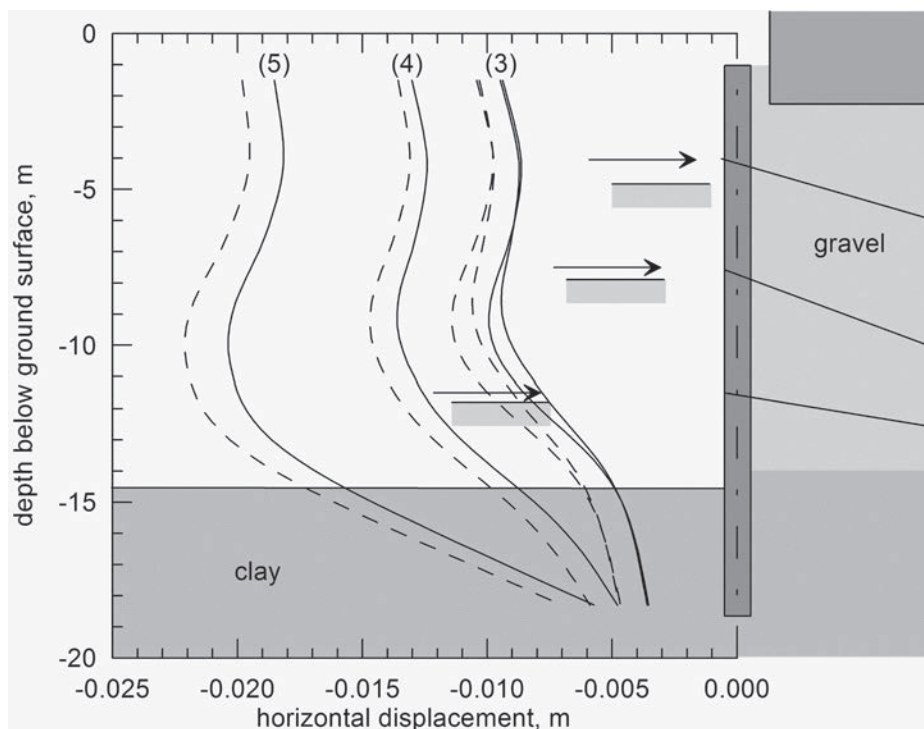


Figure 8. Comparison of horizontal wall displacements near and after the completion of the excavation with (full lines) and without (dashed lines) small strains.

When comparing the wall bending moments with and without small strains, the differences are more significant, the bending moments being smaller in the analysis with small strains than in the one without small strains. Similar results are obtained for the anchor forces.

Another comparison was made in order to determine the influence of the overconsolidation ratio on the behaviour of the gravel. Fig. 9 shows the results for the overconsolidation ratio of 2 and for normally consolidated gravel with $OCR = 1$ and $K_0 = K_0^{nc} = 0.426$. The full lines correspond to the overconsolidated gravel and the dashed lines to the normally consolidated gravel, all calculated with the option for small strains. It is clear that the differences between the corresponding curves are negligible, so that the overconsolidation ratio for the gravel does not influence its behaviour. The same does not hold true for the hard clay, but this analysis is of minor importance because the overconsolidation ratio for the clay was determined with sufficient certainty.

The stability analysis was also performed using the option of reducing the soil's strength parameters by a common factor, which can then be taken as the safety factor for the soil. For undrained conditions the safety factor was $F \approx 1.6$, and for drained conditions $F \approx 1.3$. It has to be emphasized that the performed analyses

lead to the mobilization of the wall resistance, and for the undrained conditions also the mobilization of the anchor steel resistance. While this is not especially important for the wall, due to its ductility, it is of utmost importance for the anchor steel, because it has brittle behaviour, which leads to an annulment of the anchor forces at failure. As a result, it is essential to determine at exactly which point the anchor steel resistance is mobilized. In the undrained conditions, this occurred for a safety factor of a little below 1.6.

6 CONCLUSIONS

The described research of a case history involving the construction of an anchored wall for the protection of an excavation showed that it is possible to adequately predict wall displacements and stability based on standard geotechnical investigations, soil data from the literature and a finite-element computer programme with a realistic soil model. It was shown that it is very important to clearly understand the functioning of the selected soil model. This can be achieved by numerical simulations of a standard laboratory test with stress paths that are relevant for the geotechnical structure under consideration.

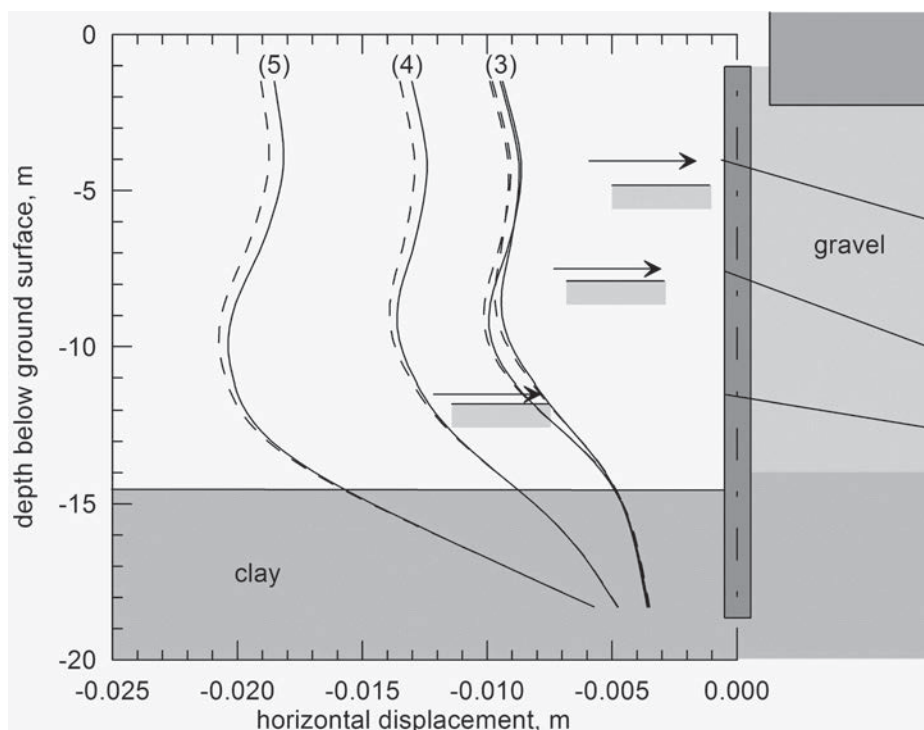


Figure 9. Comparison of horizontal wall displacements near and after the completion of the excavation for the overconsolidated (full lines) and the normally consolidated (dashed lines) gravel.

The soil-parameter determination for numerical simulations has the most important role in this type of analysis and the most valuable parameter is the shear modulus at very small strains, obtained from field measurements of the shear-wave velocity. The reduction of the shear modulus with increasing strains was obtained by using published evidence. The soil behaviour was analysed with and without the option of small strains. It is clear that it is not necessary to use modelling with small strains in order to get a satisfactory prediction of the wall displacements because the differences in the two types of analysis are within the general uncertainties of modelling. However, the determination of the soil stiffness at larger strains has to be very detailed and based on solid arguments, because it greatly influences the results.

This is just one example of an analysis of a case history, but it is encouraging, and further similar research might lead to more reliable and more economic designs. Until then, the prediction of soil behaviour in similar situations will still be a challenge for designers who have to take into consideration that the use of finite-element programmes requires a studious approach.

ACKNOWLEDGEMENTS

This research was conducted with the help of G. Plepelić from Prizma, Zagreb, and I. Sokolić and V. Szavits-Nossan from the Faculty of Civil Engineering of the University of Zagreb, to whom I would like to express my deep gratitude.

REFERENCES

- [1] Gaba, A. R., Simpson, B., Powrie, W. Beadman, D. R. (2003). *Embedded retaining walls – guidance for economic design*. CIRIA Report C580, London.
- [2] Potts, D. M., Zdravkovic, L. (2001). *Finite element analysis in geotechnical engineering: Application*. Thomas Telford, London.
- [3] Potts, D., Axelsson, K., Grande, L., Schweiger, H., Long, M. (2002). *Guidelines for the use of advanced numerical analysis*. Thomas Telford, London.
- [4] Schweiger, F. H. (2002). *Benchmarking in geotechnics 1*. Report No.CGG_IR006_2002. Computational Geotechnics Group, Institute for Soil Mechanics and Foundation Engineering, Graz University of Technology, Austria.
- [5] De Vos, M., Whenham, V. (2006). Workpackage 3 – Innovative design methods in geotechnical engineering. Background document to part 2 of the final WP3 report on the use of finite element and finite difference methods in geotechnical engineering. Geotechnet (<http://www.geotechnet.org>)
- [6] Burland, J.B. (1989). Small is beautiful-the stiffness of soils at small strains. *Canadian Geotechnical Journ.*, Vol. 26, 499-516.
- [7] Jardine, R.J., Potts, D.M., Fourie, A.B. & Burland, J.B. (1986). Studies of the influence of non-linear stress-strain characteristics in soil-structure interaction. *Géotechnique*, Vol. 36 (3): 377-396.
- [8] Simpson, B. (1992). Retaining structures: Displacement and design. *Géotechnique*, Vol. 42 (4), 541-576.
- [9] Brinkgreve, R.B., Broere, W., Waterman, D. (2006). *PLAXIS 2D Version 8*. Plaxis bv, Delft.
- [10] Szavits-Nossan, A., Kovačević, M.S., Szavits-Nossan, V. (1999). Modeling of an anchored diaphragm wall. *Proc. Internatl. FLAC Symposium on Numerical Modeling in Geomechanics: FLAC and Numerical Modeling in Geomechanics*. Minneapolis. eds.: Detournay & Hart, Balkema, Rotterdam, 451-458.
- [11] Skempton, A.W. (1986). SPT procedures and the effects in sands of overburden pressure, relative density, particle size, aging, and overconsolidation. *Géotechnique*, Vol. 36 (3), 425-447.
- [12] BSI (2004). BS EN 1997-1:2004; *Eurocode 7: Geotechnical design – Part 1: General rules*. British standard.
- [13] Hatanaka, M. and Uchida, A. (1996). Empirical correlation between penetration resistance and effective friction of sandy soil. *Soils & Foundations*, Vol. 36 (4), 1-9.
- [14] Schanz, T., Vermeer, P.A. & Bonnier, P. G. (1999). The hardening soil model - formulation and verification. *Plaxis Symposium "Beyond 2000 in Computational Geomechanics"*, Balkema, Amsterdam, 281-296.
- [15] Benz, T. (2007). *Small-Strain Stiffness of Soils and its Numerical Consequences*. Dr-Ing Thesis. Institute of Geotechnics, University of Stuttgart, Stuttgart.
- [16] Mayne, P. W., Christopher, B. R., De Jong, J. (2001). *Manual on Subsurface Investigations*. National Highway Institute, Publication No. FHWA NHI-01-031, Federal Highway Administration, Washington, DC.
- [17] Mayne, P.W. and Kulhawy, F.H. (1982). K0-OCR relationships in soil. *Journal of Geotechnical Engineering*, Vol. 108 (GT6), 851-872.
- [18] Clayton, C. R. I. (1995). *The Standard Penetration Test (SPT): Methods and Use*. Report 143, CIRIA, London.
- [19] Mayne, P. W. (2000). Enhanced geotechnical site characterization by seismic piezocone penetration tests. Invited lecture. *Fifth International Geotechnical Conference*, Cairo University, Cairo, 95-120.
- [20] Santamarina, J. C., Cho, G. C. (2004). Soil behaviour: The role of particle shape. *Advances in Geotechnical Engineering: The Skempton Conference*. Thomas Telford, London, Vol. 1, 604-617.

MEJNE VREDNOSTI IN RAZPOREDITEV 3D PASIVNIH ZEMELJSKIH PRITISKOV

STANISLAV ŠKRABL

o avtorju

Stanislav Škrabl
Univerza v Mariboru,
Fakulteta za gradbeništvo
Smetanova ulica 17,
2000 Maribor, Slovenija
E-pošta: stanislav.skrabl@uni-mb.si

izvleček

Članek obravnava izvorni pristop določanja kritične razporeditve in mejnih vrednosti pasivnih zemeljskih tlakov za tri-dimenzionalne primere po metodi mejne analize in teorema zgornje vrednosti. Za določanje kritične razporeditve pasivnih tlakov vzdolž višine podporne konstrukcije je uporabljena metoda mejne analize z množico tri-dimenzionalnih kinematično dopustnih hiperboličnih rotacijskih porušnih mehanizmov po metodi postopnega določanja intenzitete pasivnih tlakov od zgoraj navzdol. Določena je kritična razporeditev, prijemališče in rezultatna vrednost pasivnih zemeljskih tlakov, ki se z ozirom na izbrani kinematični model lahko aktivirajo ob mejnem stanju. Rezultati analiz kažejo, da je skupna vsota pasivnih tlakov z upoštevanjem kritične razporeditve manjša od dosedaj objavljenih primerljivih vrednosti v literaturi, višina prijemališča rezultante pa je neodvisna od trenja med podpornimi konstrukcijami in zalednimi zemljinami.

ključne besede

mejna analiza, zemeljski tlak, pasivni tlak, porušna površina, interakcija zemljina-konstrukcija

THE LIMIT VALUES AND THE DISTRIBUTION OF THREE-DIMENSIONAL PASSIVE EARTH PRESSURES

STANISLAV ŠKRABL

about the author

Stanislav Škrabl
University of Maribor,
Faculty of Civil Engineering
Smetanova ulica 17,
2000 Maribor, Slovenia
E-mail : stanislav.skrabl@uni-mb.si

abstract

This paper presents a novel approach to the determination of the critical distribution and limit values of three-dimensional passive soil pressures acting on flexible walls following the upper-bound method within the framework of the limit-analysis theory. The method of limit analysis with a set of three-dimensional kinematically admissible hyperbolic translational failure mechanisms is used to determine the critical distribution of the passive pressures along the retaining structure's height. The intensity of the passive pressures is gradually determined with the mentioned translational failure mechanisms in the top-down direction. Thus, the critical distribution, the trust point and the resultant of the passive pressures that can be activated at the limit state for the chosen kinematic model are obtained. The results of the analyses show that the total sum of passive pressures, considering the critical distribution, is lower than the comparable values published in the literature. Furthermore, the trust point of the passive pressure resultant is independent of the friction between the retaining structures and the soil.

keywords

limit analysis, earth pressure, passive pressure, failure surface, soil-structure interaction

1 INTRODUCTION

In geotechnical practice, the results of three-dimensional analyses of passive earth pressures are used to design some anchor systems, to ensure the stability of the foundations of arching and bridging structures, to design embedded caissons and other retaining structures with spaced out vertical supporting elements, etc.

It is only logical that research into passive earth pressures is frequently presented in the literature. The major part of the research deals with 2D stability analyses, while much less attention is paid to 3D analyses. The magnitudes of the earth pressures for the active and passive limit states can be determined by different methods: the limit-equilibrium method (Terzaghi 1943), the slip-line method (Sokolovski 1965) and the limit-analysis method (Chen 1975). In the limit-equilibrium and slip-line methods the static equilibrium and failure conditions are considered, while the expected movements of the retaining structures are not directly considered in the analysis. Generally, a limit analysis serves for determining the upper and lower bounds of the true collapse load by taking into account the supposed movements. The results of the analyses can differ essentially, because they depend on the chosen failure mechanism or the kinematic model of the limit state. Irrespective of the chosen procedure and the method used, the considered static or kinematic model should be in equilibrium when the limit state is reached.

Researchers have used many different methods to determine earth pressures, among them Coulomb (1776), Brinch Hansen (1953), Janbu (1957), Lee and Herington (1972), Shields and Tolunay (1973), Kérisel and Absi (1990), Kumar and Subba Rao (1997), Soubra and Regenass (2000), Soubra (2000), Škrabl and Macuh (2005) and Vrecl-Kojc and Škrabl (2007).

The above-cited, published research mainly considers the 2D problem of passive earth pressures. The results of 3D analyses have been presented only by Blum (1932),

and to a restricted extent. Extensive 3D analyses were treated by Ovesen (1964), who presented the procedure for determining the bearing capacity of different anchor plates based on 2D solutions of passive earth pressures and the results of several experimental studies in 3D conditions.

Soubra and Regenass (2000) published the results of an analysis for determining the 3D passive pressure according to the limit-state analysis using the upper-bound theorem for the translational kinematic admissible multi-block failure mechanism. Duncan and Mokwa (2001) treated the procedures for determining the bearing capacities for anchor plates and presented the results of several experimental studies. Škrabl and Macuh (2005) presented the procedure for a spatial passive pressure analysis based on the hyperbolic kinematic admissible failure mechanism and the upper-bound theorem.

The authors of all the above-mentioned works considered the presumed distribution of passive pressure along the retaining wall height (a triangular distribution for the determination of the self-weight contribution, γ , and a rectangular distribution for the determination of the surcharge contribution, q).

This paper considers the distribution of passive earth pressures along the retaining structure height. The passive pressures distribution is determined numerically with simultaneous analyses of twenty different kinematically admissible translational spatial failure mechanisms.

The results of the analyses show that the resultants of the passive pressures obtained by the presented, proposed procedure give values, lower than those published in the literature for almost all cases; only for the case when $\delta = 0^\circ$ and $\phi \leq 30^\circ$ are the differences minimal, where the values are a little lower or equal to the values presented by Soubra and Regenass (2000), and Škrabl and Macuh (2005).

The application of the upper-bound theorem ensures that the actual values of the passive soil pressures cannot be higher than the values presented in the continuation of this paper.

2 ASSUMPTIONS AND LIMITATIONS

It is a characteristic of passive earth pressures under 3D conditions that they increase as the width of the wall decreases. The value depends on the ground properties and the height/width relationship of the wall. It can be several times higher than the value for 2D cases. The

presented geomechanical analysis is based on the following suppositions and limitations:

- the structure discussed is a vertical, flexible wall with an area of $b \cdot h$ (b = width; h = height) and a horizontal backfill,
- the distribution of the passive pressures (p_p) along the wall height is defined by:

$$p_p = e_{p\gamma} \cdot \gamma \cdot (y - y_0) + e_{pq} \cdot q + e_{pc} \cdot c \quad (1)$$

where factors $e_{p\gamma}$, e_{pq} and e_{pc} define the distribution of the passive pressures along the height of the vertical wall, and y and y_0 are the coordinates (see Fig. 1),

- the resulting value of the passive earth pressure is defined by:

$$P_p = K_{p\gamma}^* \cdot \gamma \frac{h^2}{2} b + K_{pc}^* \cdot c \cdot h \cdot b + K_{pq}^* \cdot q \cdot h \cdot b \quad (2)$$

where $K_{p\gamma}^*$, K_{pc}^* and K_{pq}^* are comparative coefficients of the passive earth pressure due to the soil-weight influence, the cohesion influence, and the surcharge influence, respectively, for a standard, assumed passive pressure distribution,

- the value of the factor $e_{p\gamma}$ at the top of the wall ($y=y_0$) is equal to 0, its appurtenant values e_{pq} and e_{pc} are determined with a two-dimensional model ($b/h = \infty$) considering the boundary condition for the 3D kinematic admissible failure mechanism,
- the discussed translational failure mechanism is bounded by the log spiral in the region of the retaining wall, and by the hyperbolic surfaces defined by the envelope of the connected hyperbolic half-cones at the lateral sides,
- the lateral surfaces coincide with the margins of the considered retaining wall,
- the backfill is homogenous, the soil is isotropic and considered as a Coulomb material with the associative flow rule obeying Hill's maximal work principle.

3 THE UPPER- AND LOWER-BOUND THEOREMS

The upper-bound theorem ensures that the rate of the work due to the external forces of the kinematic systems in equilibrium is smaller than, or equal to, the rate of dissipated internal energy for all kinematically

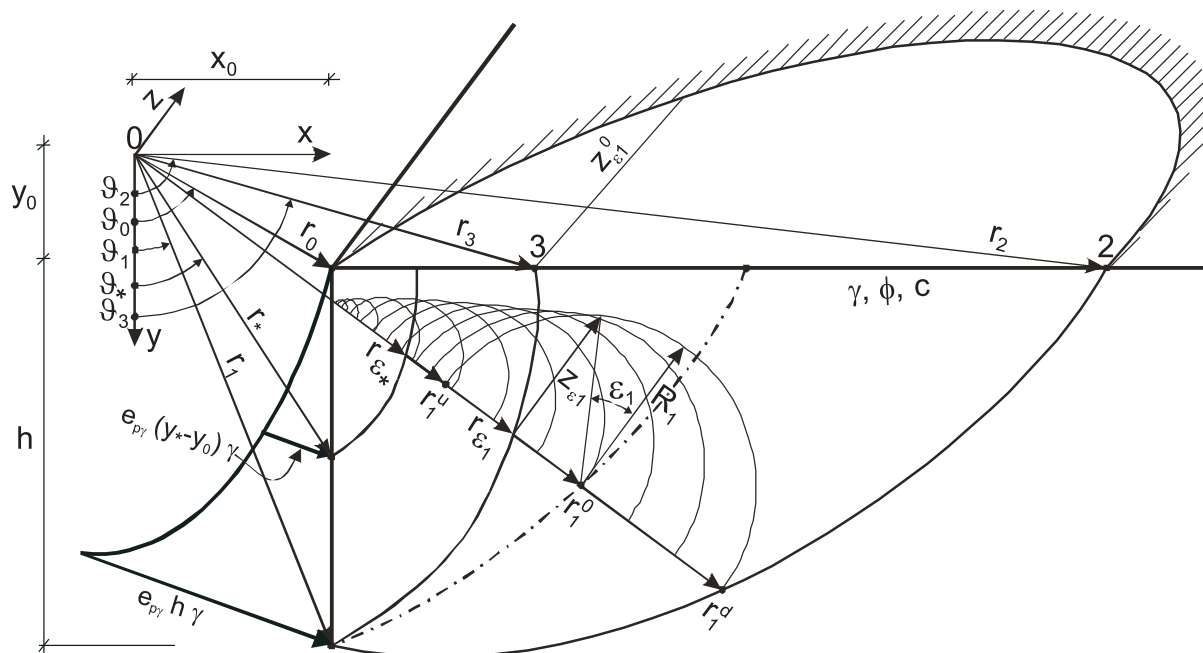


Figure 2. The scheme of the spatial failure mechanism.

All hyperbolic half-cones whose infinite set represents the lateral surface of the failure mechanism are also kinematically admissible when the additional geometry condition is satisfied:

$$\vartheta_0 \leq [\pi/2 - \phi] \quad (7)$$

which ensures that there exists no half-cone with its apex on the vertical wall (1-0, see Fig. 2) that could intersect the vertical wall under point (r_0, ϑ_0) .

Since all the hyperbolic half-cones are kinematically admissible, then using the additional condition (7) the lateral surface, which is the envelope of the infinite set of all half-cones defined by expressions (8), (9) and (10), is also kinematically admissible.

$$r_{\varepsilon} = r \cdot \cosh[(\vartheta - \vartheta_0) \tan \phi] - r \cdot \sinh[(\vartheta - \vartheta_0) \tan \phi] \sin(\varepsilon_0) \quad (8),$$

$$z_{\varepsilon_0} = r \cdot \sinh[(\vartheta - \vartheta_0) \tan \phi] \cos(\varepsilon_0) \quad (9),$$

$$\varepsilon_0 = \arcsin(dR / dr) = \arcsin \left\{ \frac{\tanh[(\vartheta - \vartheta_0) \tan \phi] + \tan \phi \tan \vartheta_0}{1 + \tanh[(\vartheta - \vartheta_0) \tan \phi] \tan \phi \tan \vartheta_0} \right\} \quad (10).$$

Considering $r = r_1$ and $\vartheta = \vartheta_1$, expressions (8), (9) and (10) define the coordinates of the envelope on the leading half-cone.

The coordinate z_f of the lateral failure surface can be expressed:

$$\forall r \geq \frac{x_0}{\sin \vartheta} \wedge r \leq r_{\varepsilon_1}; \quad (11)$$

$$z_f = z_{\varepsilon_0} = r \cdot \sinh[(\vartheta - \vartheta_0) \tan \phi] \cos(\varepsilon_0)$$

$$\forall r \geq r_{\varepsilon_1} \wedge r \leq r_1 e^{(\vartheta - \vartheta_1) \tan \phi}; \quad (12)$$

$$z_f = z(r, \vartheta) = \sqrt{2rr_1 \cosh[(\vartheta - \vartheta_1) \tan \phi] - r^2 - r_1^2}$$

5 WORK EQUATION

The considered failure mechanism on the width b is limited on the left by a vertical wall, on the right by a curved surface in the shape of a log spiral, and above by an even surface on which the surcharge can act. Both lateral surfaces are defined by the curved surfaces of the leading half-cone and the envelope of all the other hyperbolic half-cones (see Fig. 2).

At each point on the so-formed failure surface the normal vector of the surface encloses with the plane r - z shear angle ϕ and also defines the direction of the normal stress to the surface (see Fig. 3).

$$dN = \sigma dA, \quad dT_\phi = dN \tan \phi, \quad dQ_\phi = \sqrt{dN^2 + dT_\phi^2} \quad (13)$$

where σ and A denote the normal stress and the area of the lateral surface, and N and T_ϕ denote the resultant

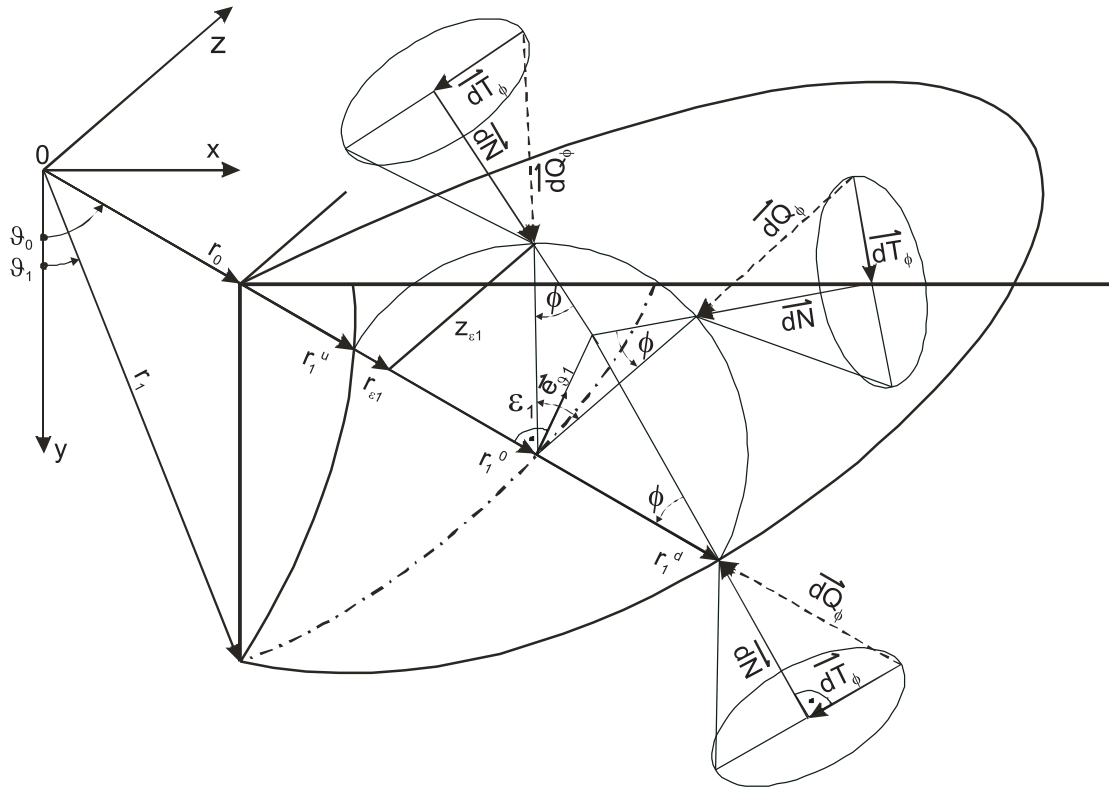


Figure 3. The forces on the failure surface.

values of the normal and the shear-stress components on the spatially formed failure surface.

The shear cones on the failure surface define all the real or admissible directions of the forces dT_ϕ and dQ_ϕ (see Fig. 3). According to the upper-bound theorem the analyses should consider those directions of shear-strength activation that are kinematically admissible and ensure the highest possible value of the passive pressure for the chosen failure mechanism.

The considered spatially formed failure body is certainly symmetrical in the symmetry plane $r-\vartheta$ that runs through the centre of the rectangular wall surface, and should be in equilibrium, considering all the forces that act on it.

Certainly, all the forces dQ_ϕ act in the plane $r-z$, and so they do not cause any momentum around the z axis,

which runs through the coordinate system's origin.

Like in the 2D analyses, the equilibrium condition of all the momentums around the z axis is chosen for the work equation. From Fig. 3 it is evident that the maximum possible passive pressures arise when the shear force dT_ϕ acts at each point of the failure surface in a direction that is defined by the cross-section of the normal plane through the centre of the hyperbolic half-cone and the tangent plane to the failure plane through the considered point.

The coefficients of the individual parts of the passive pressure $e_{p\gamma}$ and e_{pq} (let us call them the coefficients of passive pressure distribution) in the 3D problem are not constant along the wall height h . Certainly, they increase non-linearly with increased ratios of b/h . If $\gamma \neq 0$, $\phi \neq 0$, $\delta \neq 0$ and $q = c = 0$ the work equation can be given in the following integral form:

$$\int_{\vartheta_1}^{\vartheta_0} e_{p\gamma} \left(\frac{x_0^3}{\tan \vartheta} - \frac{x_0^3}{\tan \vartheta_0} \right) \left(\frac{\cos \delta \cos \vartheta}{\sin^3 \vartheta} - \frac{\sin \delta}{\sin^2 \vartheta} \right) d\vartheta - \int_{\vartheta_1}^{\vartheta_0} \int_{x_0/\sin \vartheta}^{r_1 e^{(\vartheta-\vartheta_1)\tan \phi}} (1 + 2z_f/b) \sin \vartheta r^2 dr d\vartheta - \int_{\vartheta_0}^{\vartheta_2} \int_{y_0/\cos \vartheta}^{r_1 e^{(\vartheta-\vartheta_2)\tan \phi}} (1 + 2z_f/b) \sin \vartheta r^2 dr d\vartheta = 0 \quad (14)$$

$$f_{p\gamma}^m = \frac{(y_m - y_{m-1})}{2} \left[\cos \delta \frac{(y_{m-1} + 2y_m)}{3} - x_0 \sin \delta \right] \quad (18),$$

$$f_{pq}^m = \frac{(y_m - y_{m-1})}{2} \left[\cos \delta \frac{(y_{m-1} + 2y_m)}{3} - x_0 \sin \delta \right] \quad (19),$$

where $f_{p\gamma}^{m-1}$ and f_{pq}^{m-1} define the momentums of the already known values of the passive pressures, and $f_{p\gamma}^m$ and f_{pq}^m , the momentums of the passive pressures for $e_{p\gamma}^m = 1$ and $e_{pq}^m = 1$, according to the origin of the coordinate system x - y - z . The appurtenant momentum of the unit weight of the ground ($\gamma = 1$) and the surcharge ($q = 1$), above the failure surface are determined using expressions (20) and (21).

$$g_{p\gamma} = - \sum_{j=1}^n \sum_{k=1}^o A_{xy}^j w_{jk} (1 + 2z_f^{jk}/b) r_{jk} \sin \vartheta_{jk} \quad (20)$$

where A_{xy}^j denotes the area of the triangular or rectangular element j in the plane x - y (see Fig. 4), w_{jk} is

the weight coefficient for Gauss's integration point k , z_f^{jk} is the coordinate z on the envelope of the hyperbolic half-cones, r_{jk} is the radius of the integration point k on element j in the plane x - y , and ϑ_{jk} is the appurtenant angle of the radius r_{jk} . In the numerical integration of the considered problem in plane x - y , 514 rectangular and 42 triangular elements with 9 and 6 Gauss's integration points were used (see Fig. 4).

$$g_{pq} = - \sum_{l=1}^p \sum_{k=1}^r L_{xy}^l w_{lk} (1 + 2z_f^{lk}/b) r_{lk} \sin \vartheta_{lk} \quad (21),$$

where L_{xy}^l denotes the length of a one-dimensional integration element l on the ground surface $y = y_0$ in the plane x - y (see Fig. 4), w_{lk} is the weight coefficient for Gauss's integration point k , z_f^{lk} is the coordinate z of the integration point on the envelope of the hyperbolic half-cones in the plane $y = y_0$, r_{lk} is the radius of the integration point k on element l in the plane x - y , and ϑ_{lk}

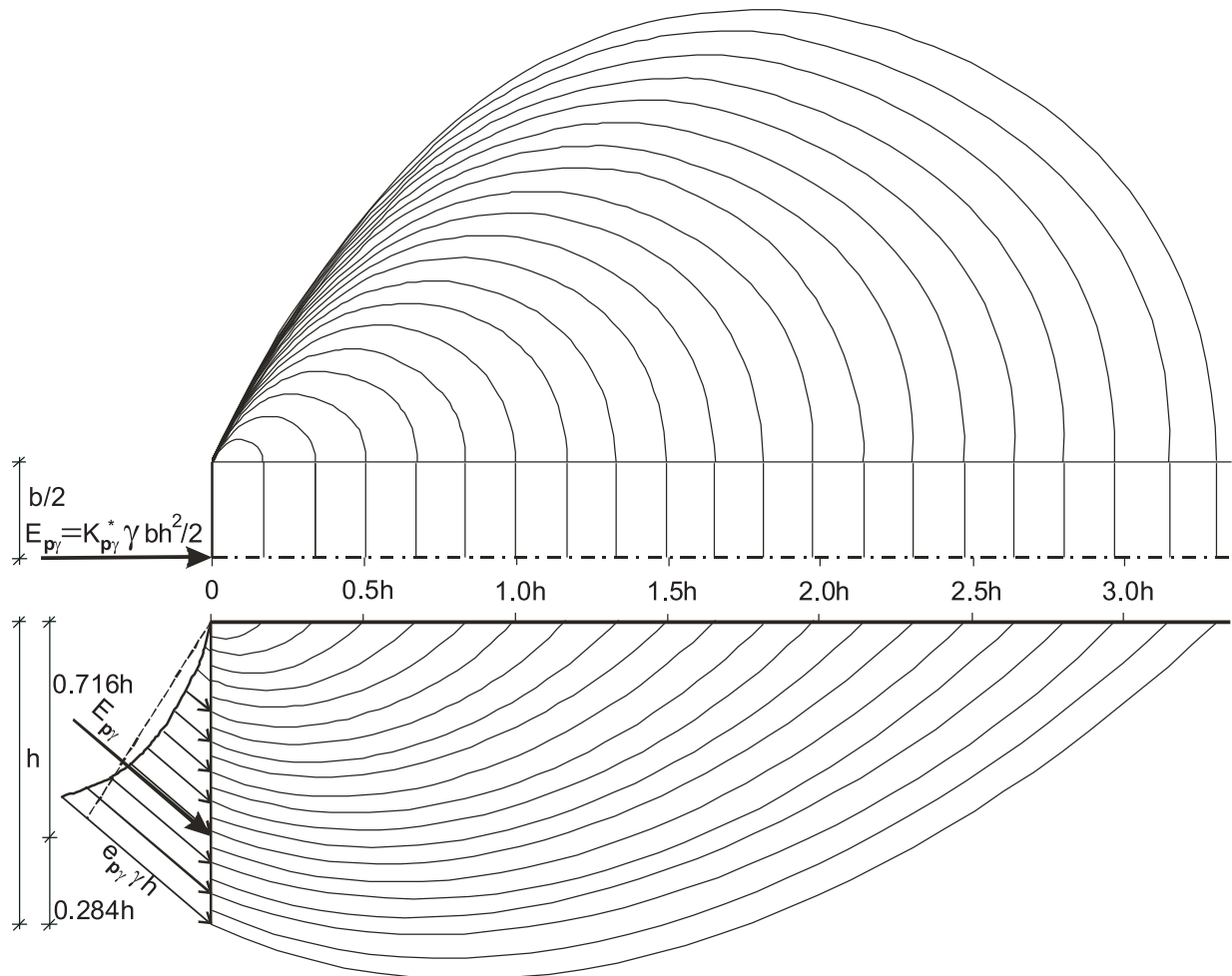


Figure 5. Set of spatial failure surfaces.

is the appurtenant angle of the radius r_{ik} . In the numerical integration of the considered problem in the plane, 42 one-dimensional integration elements with 3 Gauss's integration points were used.

The unknown values of the passive pressure distribution factors are determined using:

$$e_{p\gamma}^m = \frac{g_{p\gamma} - f_{p\gamma}^{m-1}}{f_{p\gamma}^m}; \quad e_{pq}^m = \frac{g_{pq} - f_{pq}^{m-1}}{f_{pq}^m} \quad (22),$$

In the numerical procedure determining the minimal value of the passive pressure distribution factors $e_{p\gamma}^m$ and e_{pq}^m , the starting failure surface in the optimization procedure is determined with the initial values of the parameters ϑ_1 and ϑ_2 , which should satisfy the following boundary conditions:

$$x_0 \geq 0, \quad y_0 \geq 0, \quad \vartheta_0 \geq (\pi/2) - \phi \quad (23).$$

Mathematical optimization was used to determine the unknown parameters ϑ_1 and ϑ_2 of the critical failure surface, which defines, in the considered calculation step, the minimal value of the unknown factor of the passive pressure distribution, $e_{p\gamma}^m$ and e_{pq}^m , at the toe of the wall.

The Solver Optimization Tool (Microsoft Excel) with the generalized-reduced-gradient method was used in the minimization process.

The result of the gradual determination of the passive pressure distribution factors from the top of the wall downwards are the numerical values of the factors $e_{p\gamma}$ and e_{pq} , and a set of spatial failure surfaces that are presented in Fig. 5 for the case when $\phi = 40^\circ$ and $\delta/\phi = 1$.

The values of the factors of the passive pressure distribution, $e_{p\gamma}$ and e_{pq} , for different values of ϕ , δ/ϕ and b/h are presented in Figs. 6 and 7.

The values of the comparative passive pressure coefficients, $K_{p\gamma}^*$ and K_{pq}^* , and the distances of the handling points of the resultants, a_γ , and a_q , from the surface of the backfill soil are presented in Tables 1 and 2.

The values of the handling points are given for individual shear angles and given ratios b/h , where the numerically obtained results for different shear ratios δ/ϕ do not deviate by more than 0.5% from their average value.

The appurtenant values of the substitutive coefficient and the distances of the resultants from the surface of the backfill soil are determined with the expressions (24) to (27).

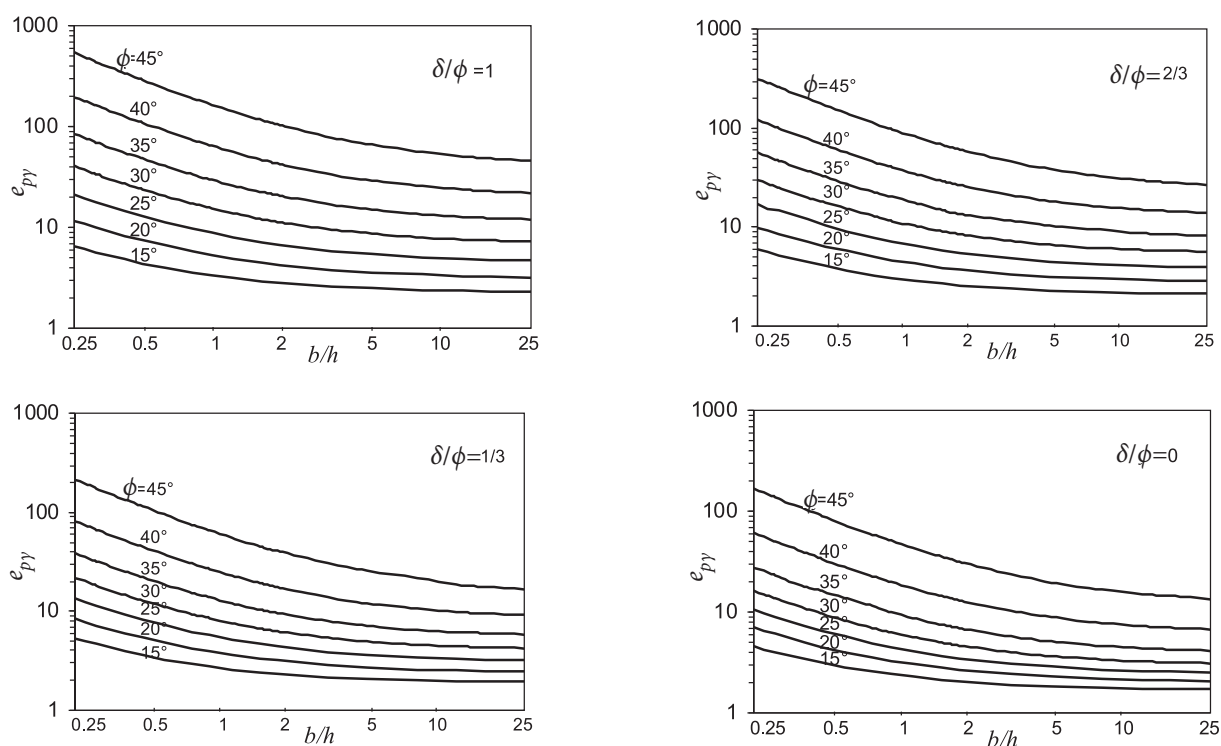


Figure 6. The factors of passive pressure distribution $e_{p\gamma}$ for different values of ϕ , δ/ϕ and b/h .

$$K_{p\gamma}^* = \sum_{i=1}^{m-1} (e_{p\gamma}^i (y_i - y_0)(y_{i+1} - y_{i-1}) + e_{p\gamma}^m (y_m - y_0)(y_m - y_{m-1})) \quad (24)$$

$$a_\gamma = \sum_{i=1}^{m-1} (e_{p\gamma}^i (y_i - y_0)(y_{i+1} - y_{i-1})(y_{i-1} + y_i + y_{i+1} - 3y_0)/3) + e_{p\gamma}^m (y_m - y_0)(y_m - y_{m-1})(y_{m-1} + 2y_m - 3y_0)/3 \quad (25)$$

$$K_{pq}^* = e_{pq}^0 (y_1 - y_0)/2 + \sum_{i=1}^{m-1} (e_{pq}^i (y_{i+1} - y_{i-1})/2 + e_{pq}^m (y_m - y_{m-1})/2) \quad (26)$$

$$a_q = e_{pq}^0 (y_1 - y_0)(y_1 - y_0)/6 + \sum_{i=1}^{m-1} (e_{pq}^i (y_{i+1} - y_{i-1})(y_{i-1} + y_i + y_{i+1} - 3y_0)/6) + e_{pq}^m (y_m - y_{m-1})(y_{m-1} + 2y_m - 3y_0)/6 \quad (27)$$

In the analyses of the spatial stability problems the theorem of corresponding states (Caquot and Kérisel 1948, Soubra and Regenass 2000) is still valid. The comparative coefficient of the passive earth pressure due to cohesion (K_{pc}^*) can be determined by using the comparative coefficient of passive earth pressure due to the surcharge (K_{pq}^*).

$$K_{pc}^* = \frac{K_{pq}^* - 1/\cos(\delta\phi)}{\tan(\phi)} \quad (28)$$

The values of K_{pc}^* for the purely cohesive soil ($c > 0$ and $\phi = 0$) with different ratios of c_a/c and with a centre of gravity of e_{pc} the pressures measured from the top of the wall are given in Table 3.

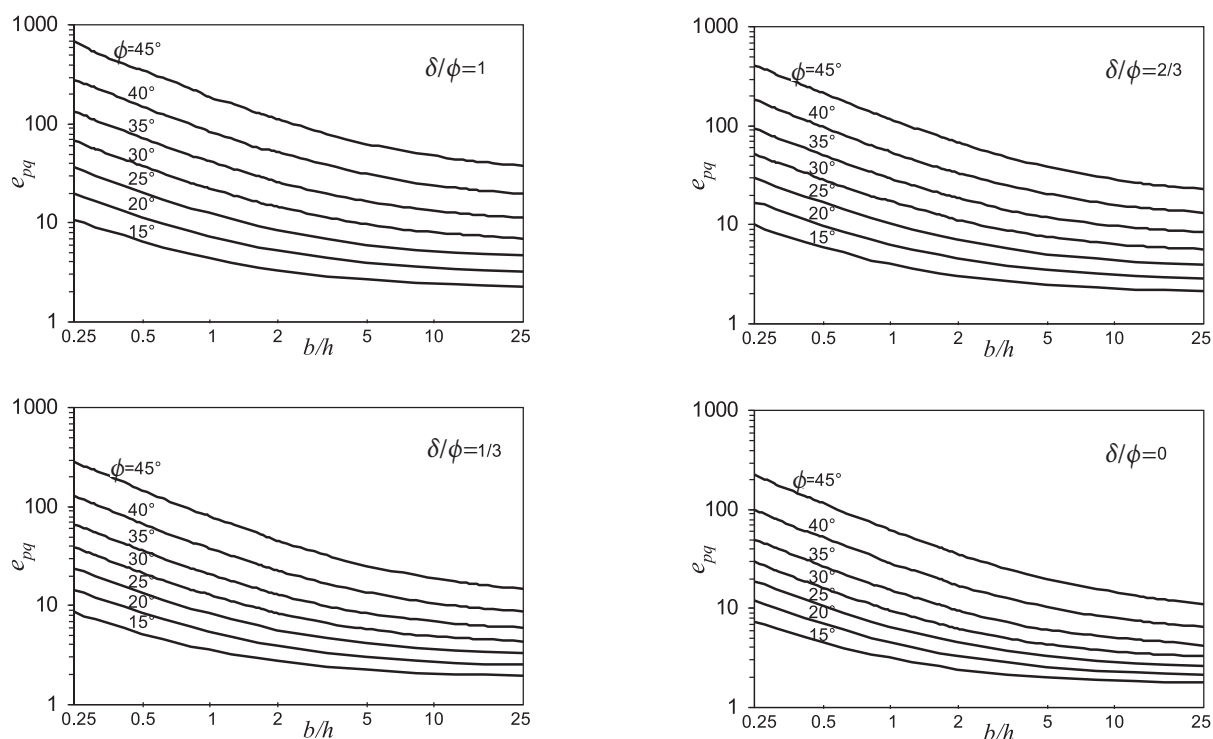


Figure 7. The factors of passive pressure distribution e_{pq} for different values of ϕ , δ/ϕ and b/h .

Table 1. Values of K_{py}^* for different values of the parameters ϕ , δ and b/h with the centre of gravity of the e_{py} pressures measured from the top of the wall

b/h	ϕ (deg)	δ/ϕ				center of gravity	
		0	1/3	1/2	1		
0.25	15	3.6279	4.1527	4.3864	4.6365	5.1458	0.712
	20	5.3933	6.4350	7.0004	7.5984	8.8877	0.712
	25	7.9261	10.0117	11.2456	12.6106	15.7108	0.725
	30	11.8711	15.9410	18.5946	21.7237	29.5912	0.730
	35	20.0486	27.6728	33.3372	40.5337	60.4985	0.734
	40	43.0671	57.3693	69.2222	85.9233	139.1175	0.738
	45	116.4677	149.3839	177.6761	220.0038	375.5334	0.741
0.5	15	2.6711	3.0260	3.2012	3.3775	3.7313	0.699
	20	3.7238	4.4311	4.8126	5.2130	6.0592	0.706
	25	5.2089	6.5721	7.3711	8.2474	10.2079	0.712
	30	7.4363	9.9335	11.6437	13.5710	18.3323	0.718
	35	11.9863	16.5711	19.9663	24.2567	36.0095	0.724
	40	24.6495	32.8951	39.7426	49.3782	79.7705	0.729
	45	64.2513	82.5392	98.8063	121.9540	208.4111	0.734
1	15	2.1892	2.4647	2.6014	2.7383	3.0092	0.687
	20	2.8862	3.4211	3.7071	4.0047	4.6270	0.693
	25	3.8439	4.8396	5.4156	6.0425	7.4308	0.698
	30	5.8439	7.0201	8.1663	9.4902	12.6793	0.704
	35	7.9191	11.0232	13.2817	16.1123	23.6998	0.710
	40	15.4367	20.6573	25.0023	31.1047	50.0679	0.716
	45	38.1335	49.1298	58.6535	72.9298	124.8263	0.723
2	15	1.8479	2.1801	2.2961	2.4114	2.6380	0.678
	20	2.4651	2.9099	3.1455	3.3890	3.8937	0.683
	25	3.1579	3.9637	4.4240	4.9214	6.0131	0.687
	30	4.1095	5.5370	6.4305	7.4462	9.8331	0.691
	35	5.9395	8.2498	9.9397	12.0356	17.5319	0.696
	40	10.8269	14.5378	17.6323	21.9686	35.1861	0.702
	45	25.0634	32.4150	38.8084	48.4179	83.0027	0.707
5	15	1.7980	2.0064	2.1091	2.2105	2.4084	0.672
	20	2.2106	2.5986	2.8021	3.0112	3.4411	0.674
	25	2.7423	3.4307	3.8182	4.2341	5.1395	0.676
	30	3.4441	4.6399	5.3717	6.1970	8.1113	0.679
	35	4.7302	6.5872	7.9347	9.5873	13.8072	0.682
	40	8.0584	10.8652	13.2127	16.4877	26.2246	0.686
	45	17.2046	22.3721	26.8925	33.7108	57.8700	0.691
10	15	1.7483	1.9478	2.0456	2.1422	2.3290	0.670
	20	2.1253	2.4935	2.6857	2.8827	3.2865	0.671
	25	2.6034	3.2508	3.6129	4.0005	4.8411	0.672
	30	3.2223	4.3370	5.0128	5.7721	7.5262	0.673
	35	4.3270	6.0335	7.2664	8.7689	12.5571	0.675
	40	7.1344	9.6407	11.7401	14.6610	23.2244	0.677
	45	14.5765	19.0171	22.9160	28.8085	49.4740	0.681
2D	15	1.6984	1.8886	1.9817	2.0736	2.2518	0.667
	20	2.0396	2.3876	2.5686	2.7541	3.1334	0.667
	25	2.4644	3.0696	3.4067	3.7670	4.5479	0.667
	30	3.0000	4.0321	4.6525	5.3492	6.9591	0.667
	35	3.6901	5.4448	6.5993	7.9724	11.3870	0.667
	40	4.5989	7.6224	9.8346	12.6613	20.3076	0.667
	45	5.8284	11.1974	15.6822	21.9144	40.6109	0.667

Table 2. Values of K_{pq}^* for different values of the parameters ϕ , δ and b/h with the centre of gravity of the e_{pq} pressures measured from the top of the wall

b/h	ϕ (deg)	δ/ϕ					center of gravity
		0	1/3	1/2	2/3	1	
0.25	15	4.5768	5.2900	5.6081	5.9280	6.5309	0.609
	20	7.0283	8.4840	9.2341	9.9907	11.5050	0.621
	25	10.7112	13.5556	15.1308	16.8518	20.5128	0.630
	30	16.2767	21.6076	25.0415	28.8780	37.6802	0.637
	35	26.9519	36.2461	42.7186	51.2493	72.8142	0.642
	40	52.6835	68.3932	81.3285	98.5627	151.3097	0.646
	45	116.5809	149.1632	176.9264	217.2506	349.3207	0.650
0.5	15	3.1488	3.5825	3.8054	4.0025	4.4002	0.582
	20	4.5447	5.4631	5.9108	6.3815	7.3299	0.596
	25	6.5956	8.3312	9.2904	10.3297	12.5242	0.608
	30	9.6385	12.8412	14.8706	17.1286	22.2471	0.618
	35	15.4244	20.8022	24.6109	29.5968	41.8059	0.625
	40	29.1399	37.9850	45.2969	55.1065	84.9392	0.632
	45	62.8494	88.6238	95.8063	118.0501	191.9431	0.638
1	15	2.4316	2.7450	2.9041	3.0424	3.3246	0.555
	20	3.3004	3.9297	4.2434	4.5715	5.2181	0.569
	25	4.5344	5.7128	6.3552	7.0497	8.4886	0.581
	30	6.3194	8.4512	9.7630	11.2191	14.4578	0.592
	35	9.6528	13.0803	15.5514	18.7062	26.1839	0.601
	40	17.3562	22.7883	27.2809	33.3902	51.4902	0.610
	45	35.9646	46.3732	55.2288	68.4366	112.5270	0.619
2	15	2.0703	2.3184	2.4440	2.5563	2.7758	0.534
	20	2.6753	3.1633	3.4047	3.6552	4.1404	0.545
	25	3.5038	4.3975	4.8749	5.3812	6.4281	0.555
	30	4.6598	6.2408	7.1807	8.2196	10.4893	0.565
	35	6.7730	9.2194	11.0219	13.1920	18.2517	0.575
	40	11.4902	15.1828	18.2730	22.5430	34.4973	0.585
	45	22.5171	29.1956	34.9820	43.6475	72.5151	0.598
5	15	1.8513	2.0600	2.1639	2.2564	2.4323	0.516
	20	2.2974	2.6965	2.8917	3.0896	3.4692	0.522
	25	2.8854	3.5970	3.9688	4.3579	5.1504	0.529
	30	3.6641	4.9014	5.6070	6.3809	8.0320	0.536
	35	5.0419	6.9032	8.2543	9.7985	13.3404	0.543
	40	7.9825	10.6136	12.8683	16.0172	23.9640	0.551
	45	14.4186	18.8594	22.8019	28.7468	47.8074	0.560
10	15	1.7775	1.9726	2.0678	2.1531	2.3132	0.509
	20	2.1705	2.5382	2.7169	2.8958	3.2362	0.512
	25	2.6793	3.3254	3.6605	4.0075	4.7070	0.516
	30	3.3322	4.4441	5.0746	5.7474	7.1781	0.521
	35	4.4630	6.1341	7.3062	8.6307	11.6245	0.526
	40	6.7878	9.0886	11.0668	13.7561	20.3108	0.531
	45	11.7060	15.4077	18.7082	23.7798	39.2151	0.538
2D	15	1.6984	1.8836	1.9685	2.0050	2.1969	0.500
	20	2.0369	2.3770	2.5400	2.7022	3.0107	0.500
	25	2.4644	3.0468	3.3495	3.6573	4.2786	0.500
	30	3.0000	3.9871	4.5357	5.1180	6.3569	0.500
	35	3.6903	5.3540	6.3516	7.4707	9.9784	0.500
	40	4.5990	7.4305	9.3077	11.5115	16.7775	0.500
	45	5.8284	10.7914	14.4498	19.0443	30.7851	0.500

Table 3. Values of K_{pc}^* for $\phi = 0^\circ$ and different values b/h and c_a/c with center of gravity of e_{pc} pressures measured from the top of the wall.

b/h	K_{pc}^*					center of gravity
	$c_a/c = 0$	$c_a/c = 1/3$	$c_a/c = 1/2$	$c_a/c = 1/3$	$c_a/c = 1$	
0.25	6.9282	7.4720	7.7231	7.9631	8.4156	0.6051
0.50	4.5691	5.0257	5.2356	5.4287	5.7541	0.5854
1.00	3.3302	3.7248	3.8942	4.0439	4.2737	0.5611
2.00	2.6822	3.0314	3.1760	3.3024	3.4925	0.5391
5.00	2.2783	2.5938	2.7217	2.8321	2.9997	0.5192
10.00	2.1402	2.4427	2.5646	2.6693	2.8249	0.5104

Table 4. Comparison of K_{py}^* and K_{pq}^* with K_{py} and K_{pq} for different values ϕ , δ/ϕ and b/h .

ϕ (°)	δ/ϕ	K_{py} (Soubra and Regenass 2000)			K_{py} (Škrabl and Macuh 2005)			K_{py}^* (proposed)		
		$b/h=0.5$	$b/h=1.0$	$b/h=10.0$	$b/h=0.5$	$b/h=1.0$	$b/h=10.0$	$b/h=0.5$	$b/h=1.0$	$b/h=10.0$
20	0.5	5.04	3.85	2.75	4.92	3.76	2.69	4.81	3.71	2.69
	1.0	6.99	5.14	3.35	6.35	4.77	3.30	6.06	4.63	3.29
40	0.5	53.74	31.22	14.75	41.55	25.92	11.85	39.74	25.00	11.74
	1.0	131.75	77.02	26.42	90.36	55.48	23.93	79.77	50.07	23.22
ϕ (°)	δ/ϕ	K_{pq} (Soubra and Regenass 2000)			K_{pq} (Škrabl and Macuh 2005)			K_{pq}^* (proposed)		
		$b/h=0.5$	$b/h=1.0$	$b/h=10.0$	$b/h=0.5$	$b/h=1.0$	$b/h=10.0$	$b/h=0.5$	$b/h=1.0$	$b/h=10.0$
20	0.5	6.22	4.45	2.75	6.10	4.35	2.73	5.91	4.24	2.72
	1.0	8.06	5.54	3.17	7.79	5.44	3.27	7.33	5.22	3.24
40	0.5	74.26	43.48	12.82	49.68	29.50	11.33	45.30	27.28	11.07
	1.0	130.19	73.35	21.22	104.80	61.07	21.36	84.94	51.49	20.31

7 COMPARISON WITH EXISTING SOLUTIONS

In the literature only 2D analyses of the soil-pressure-limit values using different approaches are presented, while the research results for 3D cases are very limited. The research results of 3D passive pressure analyses according to the theorem of the upper-bound value have been presented in Soubra and Regenass (2000), and Škrabl and Macuh (2005).

A comparison of the results for the coefficients K_{py}^* and K_{pq}^* for $\delta/\phi = 0.5$ and 1, $\phi = 20^\circ$ and 40° , $b/h = 0.5, 1, 10$ is presented in Table 4.

A comparison of the results indicates that, particularly at greater shear angles and greater ratios of δ/ϕ , the differences between the values of passive-earth-pressure coefficients for the compared failure mechanisms are the greatest. The coefficient K_{py} for the proposed translational failure mechanism is up to 11.72% smaller than the same coefficient for the failure mechanism (Škrabl

and Macuh, 2005) when $b/h = 0.5$, while the coefficient K_{pq} is up to 18.95% smaller for the same $b/h = 0.5$. For higher ratios of b/h the difference gradually decreases, and when $b/h > 20$ the solutions are almost equal.

8 CONCLUSIONS

This paper presents a procedure for determining 3D passive earth pressures according to the kinematic method of limit analysis. The set of three-dimensional kinematically admissible hyperbolic translational failure mechanisms with lateral surfaces bounded by the envelope of the hyperbolic half-cones is used to determine the critical distribution of passive pressure along a flexible retaining structure's height. The intensity of the passive pressures is gradually determined with the previously mentioned translational failure mechanisms from above, downwards. Thus, the critical distribution, the trust point and the resultant of the passive pressures that can be activated at the limit state for the chosen kinematic model are obtained.

Using the diagrams presented in Figs. 6 and 7 it is possible to determine the actual critical distribution of the passive pressure limit values for any arbitrary practical case (within the frame of given assumptions) that is applicable in geotechnical design.

The results of the numerical analyses indicate that, when considering the upper-bound theorem and the set of three-dimensional kinematically admissible hyperbolic translational failure mechanisms, the passive-earth-pressure coefficients are lower than in the case of the hyperbolic translational failure mechanism and the translational mechanisms published in the literature for $b/h < 10$. The upper-bound values of the comparative passive-earth-pressure coefficients with a calculated pressure distribution are lower than the existing solutions with an assumed pressure distribution obtained using the upper-bound method within the framework of the limit analysis. This means that the classically presumed passive-earth-pressure distribution in 3D analyses is not acceptable, because it can actually not be activated. Furthermore, the trust point of the passive pressures resultant is independent of the friction between the retaining structures and the soil. Therefore, the presented results are applicable in geotechnical practice.

L_{xy}^l	length of one dimensional integration element l on the ground surface;
N	resultant value of normal stress component on spatial formed failure surface;
Q_ϕ	resultant value of stress on spatial formed failure surface;
R_c	cone diameter;
r	polar co-ordinate;
r_*	polar co-ordinate of the apex of the curved cone;
r_{ε^*}	co-ordinate appurtenant to gradient angle of the envelope;
T_ϕ	resultant value of shear stress component on spatial formed failure surface;
w_{jk}	weight coefficients for Gauss's integration point k ;
z_{ε^*}	co-ordinate appurtenant to gradient angle of the envelope;
$z_{\varepsilon l}$	co-ordinate of the section of the envelope and the leading cone shaft in plane $r-\vartheta$;
γ	unit weight of the soil;
δ	friction angle at the soil-structure interface;
εl	gradient of the envelope in point $r_{\varepsilon l}$ which is defined in an arbitrary plane $r-z$;
ϕ	angle of internal friction of the soil;
ϑ	polar co-ordinate;
ϑ_*	polar co-ordinate of the apex of the curved cone.

LIST OF SYMBOLS

A_{xy}^j	area of triangular or rectangular element j in plane $x-y$;
b	width of the retaining wall;
c	cohesion;
c_a	adhesion along the soil-structure interface;
e_{pc}	factor of passive earth pressure distribution of the cohesion influence;
e_{py}	factor of passive earth pressure distribution of the soil weight influence;
e_{pq}	factor of passive earth pressure distribution of the surcharge influence;
$f_{p\gamma}^m$	momentums of passive pressures for $e_{p\gamma}^m = 1$
f_{pq}^m	momentums of passive pressures for $e_{pq}^m = 1$
g_γ	momentums due to unit weight of the ground;
g_q	momentums due to surcharge loading on the back-fill surface;
h	height of the retaining structure;
K_{pc}^*	comparative coefficient of passive earth pressure of the cohesion influence;
$K_{p\gamma}^*$	comparative coefficients of passive earth pressure of the soil weight influence;
K_{pq}^*	comparative coefficient of passive earth pressure of the surcharge influence;

REFERENCES

- [1] Blum, H. (1932). Wirtschaftliche Dalbenformen und deren Berechnung. *Bautechnik*, 10(5): 122-135 (in German).
- [2] Brinch Hansen, J. (1953). *Earth Pressure Calculation*, Danish Technical Press, Copenhagen.
- [3] Caquot, A., and Kérisel, J. 1948. *Tables for the calculation of passive pressure, active pressure and bearing capacity of foundations*, Gauthier-Villars, Paris.
- [4] Chen, W. F. (1975). *Limit analysis and soil plasticity*. Elsevier Scientific Publishing Company, Amsterdam, The Netherlands.
- [5] Coulomb, C. A. (1776). Essai sur une application des règles de maximis et minimis à quelques problèmes de statique relatifs à l'architecture. *Mémoire présenté à l'académie Royale des Sciences, Paris*, Vol. 7, 343-382 (in French).
- [6] Drescher, A., and Detournay, E. (1993). Limit load in translational failure mechanisms for associative and non-associative materials. *Géotechnique*, London, 43(3): 443-456.
- [7] Duncan, J. M. and Mokwa, R. L. (2001). Passive earth pressures: Theories and tests. *Journal of*

- Geotechnical and Geoenvironmental Engineering Division, ASCE, 127(3): 248-257.*
- [8] Janbu, N. (1957). Earth pressure and bearing capacity calculations by generalised procedure of slices. *In Proceedings of the 4th International Conference, International Society of Soil Mechanics and Foundation Engineering*: 207-213.
- [9] Lee, I. K., and Herington, J. R. (1972). A theoretical study of the pressures acting on a rigid wall by a sloping earth on rockfill. *Géotechnique, London, 22(1): 1-26.*
- [10] Kérisel, J., and Absi, E. (1990). *Tables for the calculation of passive pressure, active pressure and bearing capacity of foundations.* Gauthier-Villard, Paris, France.
- [11] Kumar, J., and Subba Rao, K. S. (1997). Passive pressure coefficients, critical failure surface and its kinematic admissibility. *Géotechnique, London, England, 47(1): 185-192.*
- [12] Michalowski, R. L. (1989). Three-dimensional analysis of locally loaded slopes. *Géotechnique, The Institution of Civil Engineering, London, England, 39(1): 27-38.*
- [13] Michalowski, R. L. (2001). Upper-bound load estimates on square and rectangular footings. *Géotechnique, The Institution of Civil Engineering, London, England, 51(9): 787-798.*
- [14] Mroz, Z., and Drescher, A. (1969). Limit plasticity approach to some cases of flow of bulk solids. *Journal of Engineering for Industry, Transactions of the ASME, 91: 357-364.*
- [15] Ovesen, N. K. (1964). *Anchor slabs, calculation methods, and model tests.* Bull. No. 16, Danish Geotechnical Institute, Copenhagen: 5-39.
- [16] Salençon, J. (1990). An introduction to the yield design theory and its applications to soil mechanics. *European Journal of Mechanics – A/Solids, Paris, 9(5): 477-500.*
- [17] Shields, D. H., and Tolunay, A. Z. (1973). Passive pressure coefficients by method of slices. *Journal of the Soil Mechanics and Foundation Division, ASCE, 99(12): 1043-1053.*
- [18] Škrabl, S., and Macuh, B. (2005). Upper-bound solutions of three-dimensional passive earth pressures. *Canadian Geotechnical Journal, Ottawa, 42: 1449-1460.*
- [19] Sokolovski, V. V. (1965). *Static of granular media.* Pergamon Press, New York.
- [20] Soubra, A. H. (2000). Static and seismic earth pressure coefficients on rigid retaining structures. *Canadian Geotechnical Journal, Ottawa, 37: 463-478.*
- [21] Soubra, A. H., and Regenass, P. (2000). Three-dimensional passive earth pressure by kinematical approach. *Journal of Geotechnical and Geoenvironmental Engineering Division, ASCE, 126(11): 969-978.*
- [22] Terzaghi, K. (1943). *Theoretical soil mechanics.* Wiley, New York.
- [23] Vrecl-Kojc, H., and Škrabl, S. (2007). Determination of passive earth pressure using three-dimensional failure mechanism. *Acta Geotechnica Slovenica, 4(1): 10-23.*

ODZIV ZASIČENIH ZEMLJIN NA DINAMIČNO OBREMNITEV

STANISLAV LENART

o avtorju

Stanislav Lenart
Zavod za gradbeništvo Slovenije,
Odsek za mehaniko zemljin in geotehnična opazovanja
Dimičeva 12, 1000 Ljubljana, Slovenija
E-pošta: stanislav.lenart@zag.si

izvleček

V članku sta predstavljena dva najbolj izrazita načina deformiranja dinamično obremenjenih zasičenih zemljin. Likvifikacija s tečenjem in ciklična mobilnost sta pojava, ki pritegneta posebno pozornost zaradi velikih deformacij, ki ju spremljajo.

Potopitev nasipa železniške proge zaradi novozgrajenega akumulacijskega bazena na reki Savi v Boštanju in velik plaz, ki se je sprožil na področju Stože v Julijskih Alpah predstavljata študiji primerov v Sloveniji, kjer sta bili analizirani tudi likvifikacija s tečenjem in ciklična mobilnost. Upoštevana je bila dinamična obremenitev zaradi železniškega prometa in morebitne potresne obtežbe. Materiali iz obeh lokacij: meljni pesek in prodnato-peščeni melj, so bili uporabljeni v obsežnih laboratorijskih preiskavah, katerih namen je bil določiti postopek za modeliranje generiranja dodatnega pornega pritiska v dinamično obremenjenih z vodo zasičenih zemljinah.

Novejše ugotovitve kažejo, da je sprememba pornega tlaka povezana s količino disipirane energije, ki jo določajo histerezne zanke dobljene z dinamičnim obremenjevanjem. Na osnovi eksperimentalnih rezultatov je bila predlagana enačba za empirično zvezo, ki definira generiranje pornega tlaka med dinamičnim obremenjevanjem. Enačba je sestavljena iz dveh delov, prvi opisuje generiranje nepovratnih sprememb pornega tlaka, drugi del pa opisuje prirastke in upade tlaka porne vode znotraj enega obremenjevalnega cikla, ti. povratne spremembe pornega tlaka. Z uporabo predlaganega energijskega numeričnega modela je mogoče določiti dejanske efektivne napetosti in s tem napetostno pot dinamično obremenjene zemljine. Predlagani model za porne tlake se lahko uporabi tudi za modeliranje deformacijskega obnašanja. Z eksperimenti je bilo ugotovljeno, da ima dinamično obremenjena zemljina po nekaj ciklih obtežbe na začetku cikla zelo nizko togost, ki pa se kasneje poveča. Deformacija, ki se razvije za časa trajanja te podajne faze zemljine, predstavlja glavnino deleža skupne deformacije. Pojav in trajanje te faze sta prav tako povezana z energijo, ki se disipira med cikličnim obremenjevanjem. Odnos med disipirano energijo in dodatnim pornim tlakom ter kratkotrajnim tečenjem med pojavom ciklične mobilnosti, omogoča preprosto modeliranje odziva dinamično obremenjenih zasičenih zemljin.

ključne besede

likvifikacija s tečenjem, ciklična mobilnost, dodatni porni tlak, disipirana energija

THE RESPONSE OF SATURATED SOILS TO A DYNAMIC LOAD

STANISLAV LENART

About the author

Stanislav Lenart
Slovenian National Building and Civil Engineering Institute,
Section for Soil Mechanics and Geotechnical Monitoring
Dimičeva 12, 1000 Ljubljana, Slovenia
E-mail: stanislav.lenart@zag.si

Abstract

This paper presents the two most significant types of deformation behavior for dynamically loaded, saturated soil. Flow liquefaction and cyclic mobility deserve special attention because of the large deformations that accompany these two phenomena. The submergence of a railway-line embankment due to the newly built Sava-river accumulation reservoir in Boštanj and the large landslide that occurred in the Stože area in the Julian Alps are case histories in Slovenia where flow liquefaction and cyclic mobility were analyzed. The dynamic loading caused by railway traffic and possible seismic activity were taken into account. Material from these two sites, silty sand and lacustrine carbonate silt, were used in extensive laboratory research, with the objective to define a procedure for excess pore-water pressure-generation modeling in dynamically loaded saturated soil.

It has been found recently that the change of the pore-water pressure is related to the dissipated energy density calculated from the hysteresis loops caused by dynamic loading. Based on the experimental results an empirical equation defining the generation of pore pressure during dynamic loading has been proposed. The equation is divided into two parts: the first part describing the residual pore-water pressure generation, and the second part describing the increment and decrement of pore-water pressure within the load cycle, the so-called temporary pore-water pressure change. The proper effective stresses and thus the stress path of the dynamically loaded soil can be defined by using the proposed energy-based numerical model.

The proposed pore-pressure model can also be used in deformation-behavior modeling. It was observed from the experimental results that after a few cycles of dynamic loading the saturated soil starts to exhibit a very low stiff-

ness at the beginning of a load cycle, after which it begins to strengthen. The strain developed during this softening phase represents the main share of the total strain. The occurrence and duration of this phase are related to the energy dissipated during the cyclic loading as well, and the relation between the dissipated energy, the excess pore pressure and the short-term flow during cyclic mobility, give us an opportunity for a simple response modeling of the dynamically loaded saturated soils.

Keywords

flow liquefaction, cyclic mobility, excess pore pressure, dissipated energy

1 INTRODUCTION

Due to the existing hydro-power potential, a chain of five new hydro-power plants is planned for the lower part of the Sava river. The construction of the first power plant started at the Boštanj site in November 2002 and it was completed in May 2006 [1].

The railway connection between Ljubljana and Zagreb runs along the Sava river. The construction of the accumulation reservoir caused the submergence of the railway-line embankment and raised questions about possible changes in the response of newly saturated soils resulting from the dynamic load caused by the railway. Therefore, the stability analyses considering a new ground-water level were required by the owner of the railway [2, 3]. Field and laboratory tests were carried out before the upheaval of the water in order to get the input parameters for the analyses. Two possible types of saturated soil behavior were in question: liquefaction and cyclic mobility. The following extensive research gives an opportunity for a detailed study of the liquefaction potential of silty sand from the lower Sava river at Boštanj.

The other case of material susceptible to liquefaction was found in the northern part of Slovenia – in the

Julian Alps. Lacustrine material of glacial origin has been recognized as very sensitive to various factors, such as water content and loading conditions, including seismic effects. A strong earthquake in April 1998, with its epicenter in the Krn mountains and a magnitude of $M_{WA}=6.0$, caused the collapse of an approximately 100-m-long section of the shore of the 20-km-distant Lake Bohinj. Saturated lacustrine soils were thought to be present. The same earthquake, in amplified form, caused serious damage to several buildings in the village of Mala vas, near Bovec, which were founded on saturated lacustrine soil [4]. Quite soon after the above-mentioned occurrences, in November 2000, a very severe landslide occurred in the area called Stože. It resulted in debris flow in its lower part. Layers of lacustrine carbonate silt of a relatively small thickness were observed in the material displaced during the landslide, and the question arose as to whether the presence of these layers was responsible for the landslide [5]. An investigation of the static and dynamic liquefaction potential of the lacustrine carbonate silt was initiated as a result [6, 7].

Several findings from the research mentioned above are presented in this paper. Saturated silty sand from the Sava river at Boštanj and the lacustrine carbonate silt from the Julian Alps are materials that forced the author of this paper as well as the geotechnical society in Slovenia to accept the danger of liquefaction as well as the occurrence of cyclic mobility in Slovenia as real possibilities. The findings from these two recent case histories have helped to introduce a more cautious treatment of dynamically loaded saturated soil response in daily practice. They are used in this paper as examples.

2 LIQUEFACTION OF SOIL

When dynamically loaded saturated soils are being considered, the term liquefaction is very important. Liquefaction is defined as the transformation of soil from the solid to the liquid state. It happens as a consequence of increased pore pressure and a reduced effective stress, mostly in saturated cohesionless soils. When such soil is subjected to rapid loading, e.g., earthquake loading or another kind of dynamic loading, the pore water is unable to drain in a very short time period. The loading conditions might be understood, therefore, as the undrained loading conditions. If it is not too dense, a cohesionless soil subjected to cyclic loading, especially cyclic loading in the shear mode, has a tendency to densify. As the pores between the soil grains are filled with water, which cannot drain sufficiently, the generation of excess pore pressure occurs. Figure 1 shows the changes in the soil skeleton caused by cyclic loading, which results in excess pore-water pressure being generated.

The term static liquefaction (flow failure) refers to the rapid increment of pore-water pressure followed by a sudden loss of strength after the peak value of the deviator stress is reached, until a residual/steady-state strength is reached. Flow liquefaction appears when the residual strength of the soil is smaller than the static shear stress required for the equilibrium of a soil mass. The liquefied stress state, in that case, is represented by the initial effective confining pressure, decreased by the excess pore pressure.

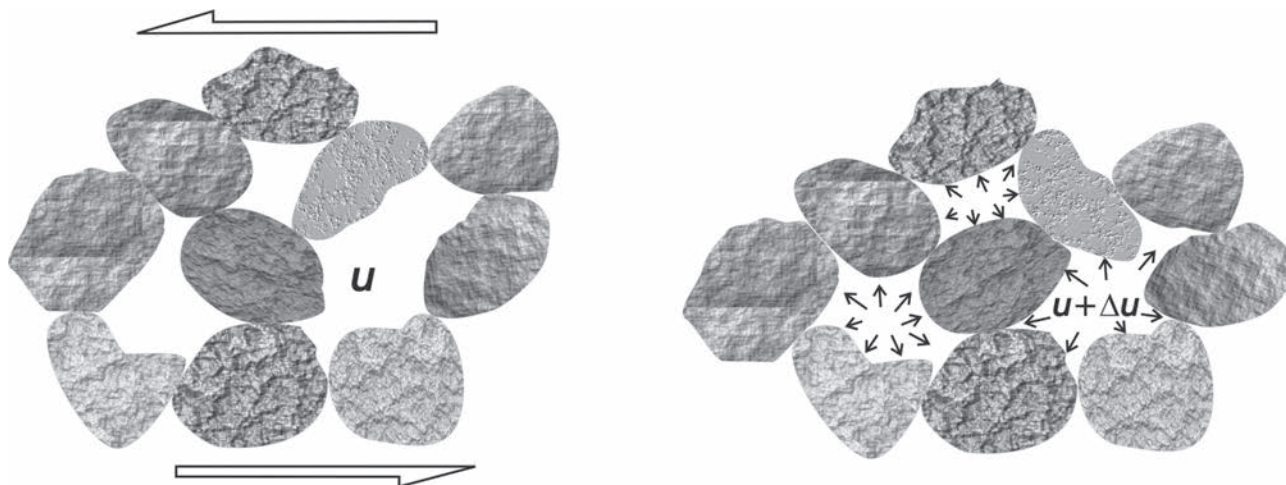


Figure 1. Cyclic loading in the shear mode causes grain movements and the generation of excess pore pressure.

2.1 SIMPLIFIED PROCEDURES FOR AN EVALUATION OF SOIL'S LIQUEFACTION POTENTIAL

Based on the findings of many previous case histories, with and without the occurrence of flow liquefaction, some simplified procedures were developed for evaluating the liquefaction potential in a specific case [8, 9, 10]. The procedures are based on different field measurements. The most widely used among them are SPT, CPT and shear-wave velocity measurements. The liquefaction potential for silty sand from the Sava river at Boštanj and lacustrine carbonate silt from the Julian Alps was evaluated in the manner of SPT and shear-wave velocity measurements. An earthquake with a magnitude of $M=7.0$ was proposed as the strongest possible type of dynamic load, and it can be seen from the results (Figure

2) that the estimated danger of the occurrence of liquefaction depends strongly on the procedure, and that the results differ. Thus, more detailed research was needed.

2.2 THE STATE-CRITERIA APPROACH

As described above, the occurrence of flow liquefaction depends upon the ability of a material to contract itself. This contractive behavior is the reason for the pore-pressure increase. Therefore, it is of interest to know where is the boundary, called the critical void ratio (CVR) line, between the contractive and dilative soil state. The states of the tested soil – silty sand from the Sava river and lacustrine carbonate silt from Julian Alps – were defined in terms of the void ratio. Tests at different effective confining pressures resulted in the CVR lines shown in Figure 3.

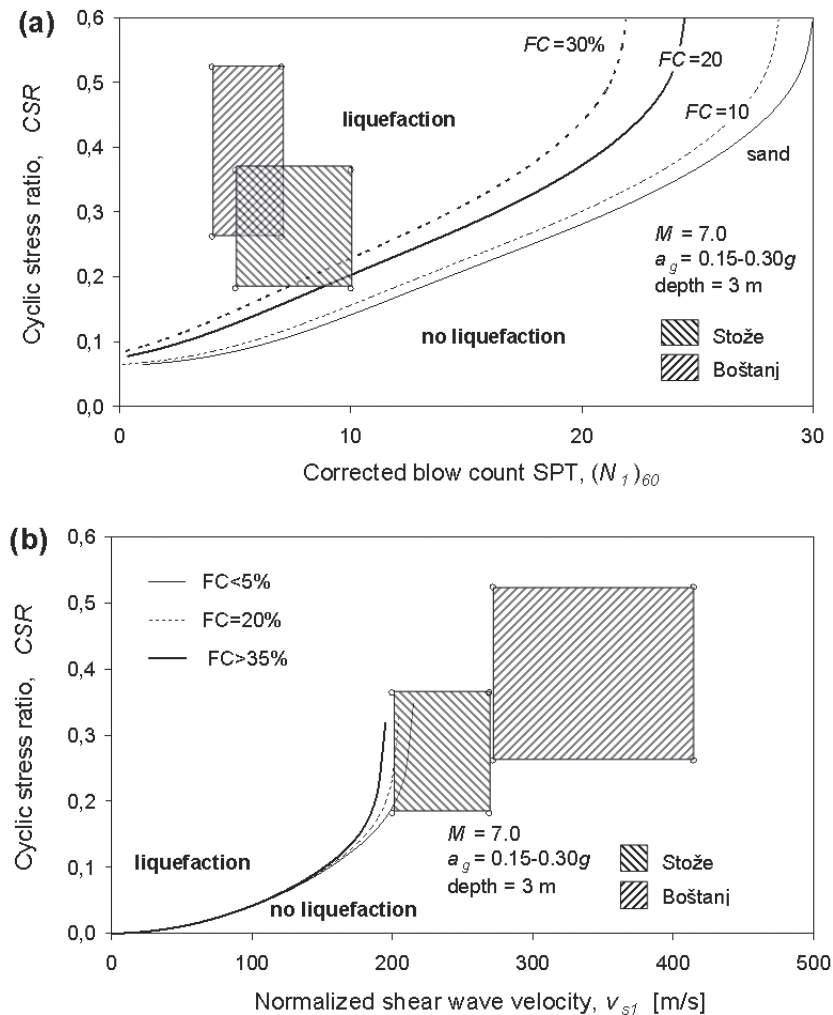


Figure 2. The danger of liquefaction occurring for silty sand from the Sava river and lacustrine carbonate silt from the Julian Alps. The CRR are based on (a) SPT measurements, (b) shear-wave velocity measurements.

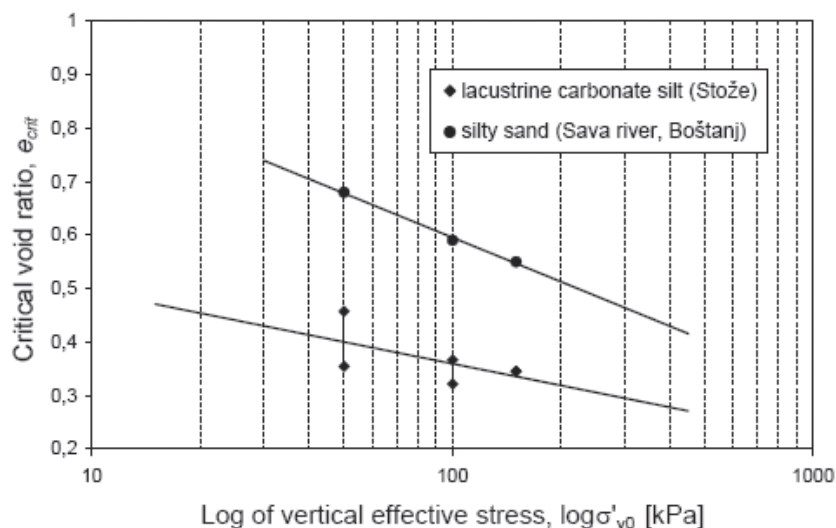


Figure 3. CVR line as a boundary between the loose contractive states and the dense dilative states of the two tested materials.

The generation of an excess pore-water pressure causes a decrease in the effective stresses. The effective-stress conditions leading to the occurrence of flow liquefaction can be most easily described in stress-path space. The response of five saturated cohesionless specimens isotropically consolidated to the same void ratio and different effective confining pressures, in undrained

stress-controlled triaxial compression is shown in Figure 4 [11]. Regarding the initial states of the specimens according to the steady-state line, specimens 1 and 2 exhibit dilative behavior when the shearing starts, while specimens 3, 4 and 5 exhibit contractive behaviors, which is necessary for flow liquefaction.

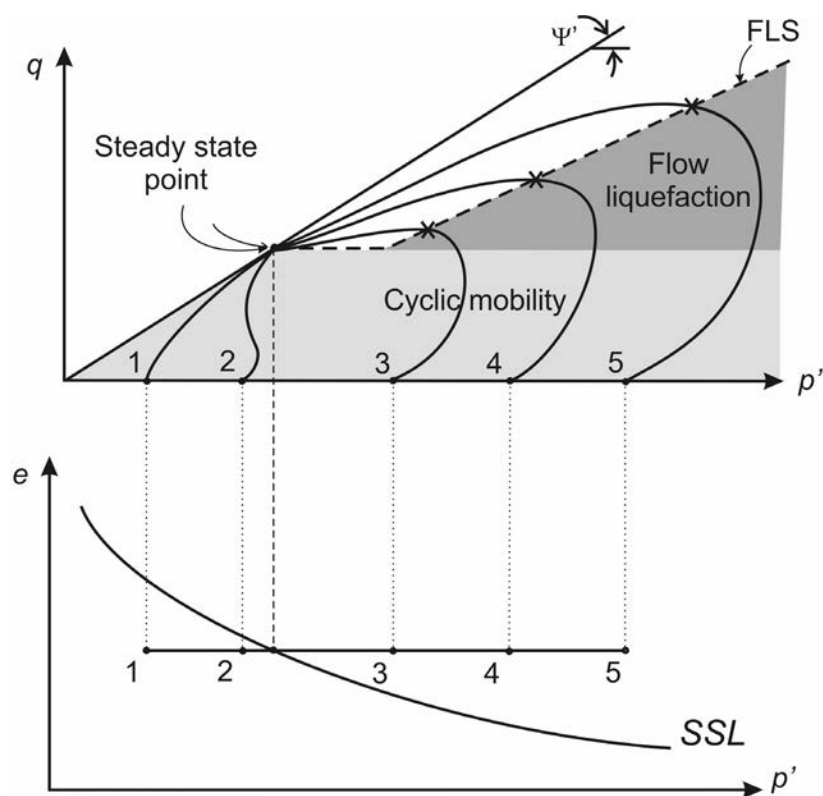


Figure 4. Initial conditions susceptible to either flow liquefaction or cyclic mobility (adapted from [11]).

The flow liquefaction is initiated at the peak of the stress path in the case of the latter three specimens. The locus of the points describing the effective stress conditions at the initiation of flow liquefaction is a straight line [11, 12] called the flow liquefaction surface (FLS). All the specimens reach the same steady-state point as they have the same void ratio. The FLS is truncated at the level of the steady-state point as flow liquefaction cannot occur if the stresses are below this point. The FLS therefore marks the boundary between the soil states at which either flow liquefaction or cyclic mobility can occur.

While cyclic mobility is described in more detail in

the next section, the flow-liquefaction potential of two investigated materials, silty sand from the Sava river at Boštanj and lacustrine carbonate silt from Julian Alps, is estimated on the basis of triaxial test results. Samples of lacustrine carbonate silt (Figure 5) were reconstituted at different initial states, while the samples of silty sand (Figure 6) were intact. The tested state of the silty sand seems unsuitable for contractive behavior and thus flow liquefaction is also not expected. Loose samples of lacustrine carbonate silt contracts remarkably during shearing. To trigger the flow liquefaction the static shear stress should exceed the shear strength of a soil in the liquefied state.

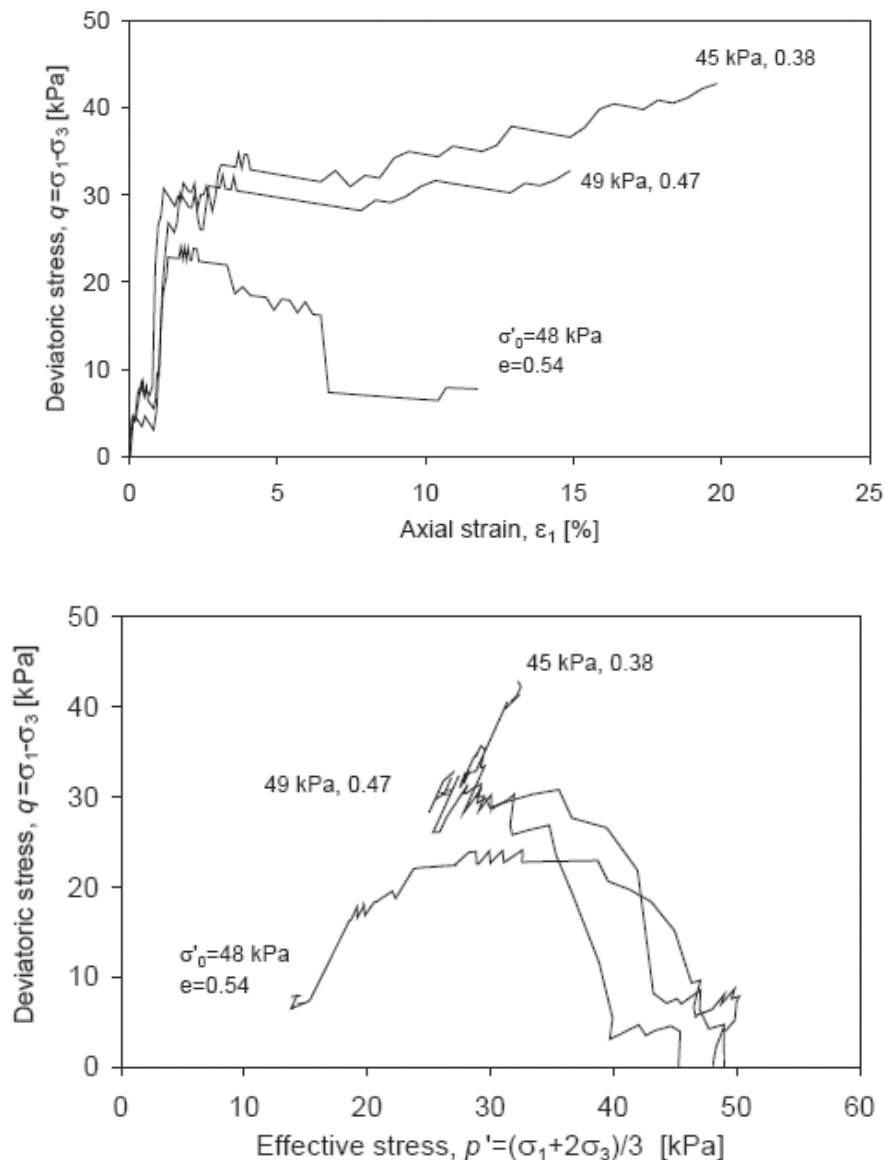


Figure 5. Undrained triaxial test of isotropic, consolidated, reconstituted samples of lacustrine carbonate silt from the Julian Alps.

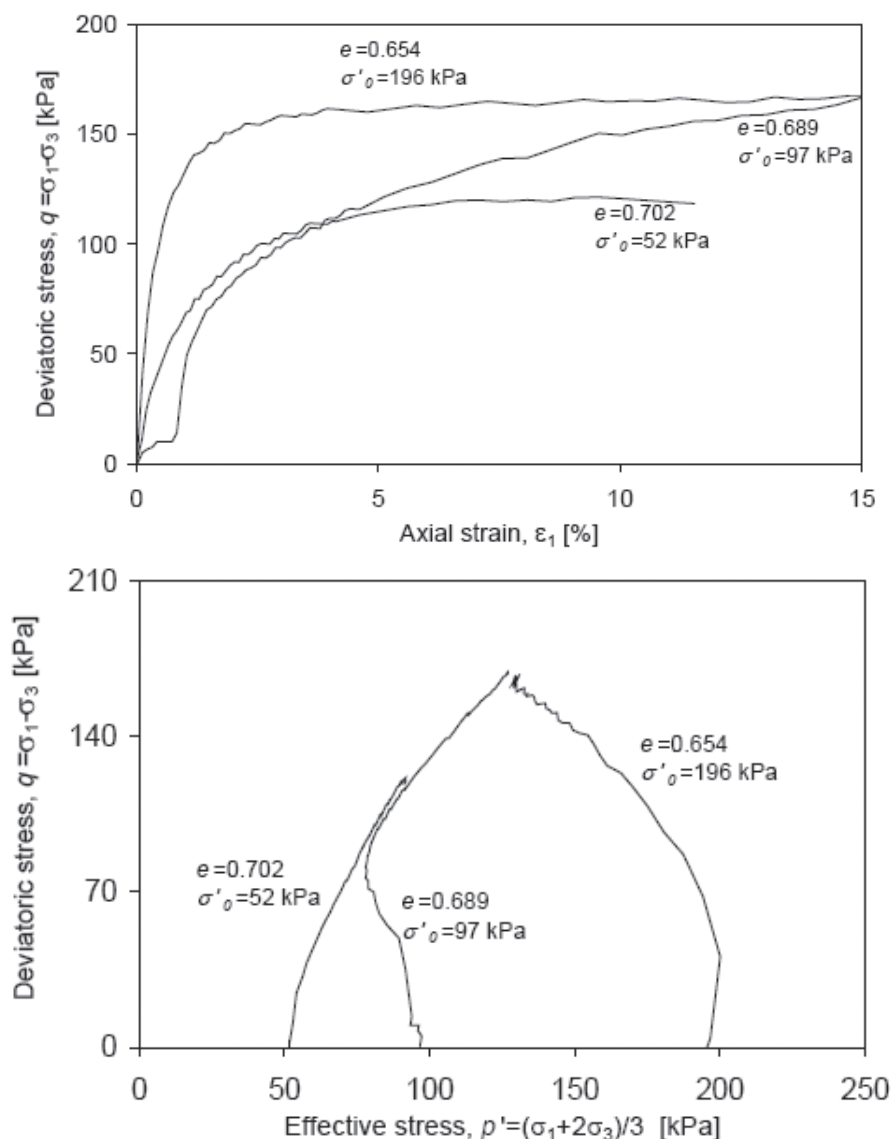


Figure 6. Undrained triaxial test of isotropic, consolidated, intact samples of silty sand from the Sava river at Boštanj.

3 CYCLIC MOBILITY

Cyclic mobility deformations are not of the flowing type and thus the damage would normally be smaller, but still severe, than in the case of flow liquefaction. Deformations due to cyclic mobility are developed incrementally during cyclic loading. The main reason for the dramatic increase of cyclic mobility deformations is the loss of stiffness caused by a decrease of the effective stresses.

An excess pore pressure generated during dynamic loading moves the stress path from its initial position in the direction of the failure envelope (Figure 7). If the cyclic stress is large enough, the steady-state strength might

be exceeded during the cyclic loading. If this happens near the FLS, the effective stress path can touch the FLS. Momentary instability can occur therefore, leading to significant strain development. If the static shear stress is smaller than the steady-state strength, the strain generally ceases when the shear stress returns to the values below the steady-state strength.

If steady-state strength is not exceeded during the cyclic loading, the effective stress path approaches the so-called phase transformation surface (PTS) [13]. The PTS represents a kind of boundary between the dilative and the contractive behavior of loaded soil. Above the PTS a dilative tendency increases the effective confinement (and consequently the shear strength), while below the

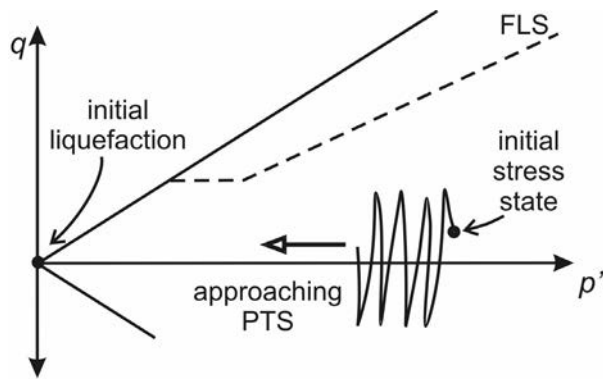


Figure 7. Generation of excess pore pressure due to the cyclic loading causes movement of the stress path from its initial position in the direction of the failure envelope.

PTS the soil exhibits a contractive behavior and thus a tendency to generate excess pore pressure. Youd [14] clearly described the rearrangements of soil grains that

happen in cyclically loaded soil when the stress path approaches and crosses the PTS from one side or the other. A significant shear strain may develop without an appreciable shear stress at the moment when the PTS is crossed (Figure 8). This, almost flowing, behavior of the soil when the stress path meets the PTS causes serious problems in the numerical modeling of cyclic mobility phenomena [15].

When the cyclic stresses are larger than the static shear stresses, stress reversal occurs. Thus, each load cycle includes compression and extension loading. Any excess pore pressure generated during the cyclic loading causes the movement of the stress path in the direction of a zero effective stress (origin of q - p graph). This state is called the initial liquefaction [16]. When the stress path reaches it, only further oscillations along the compression and extension portions of the drained failure surface are possible due to the continuation of the cyclic or monotonic loading [11].

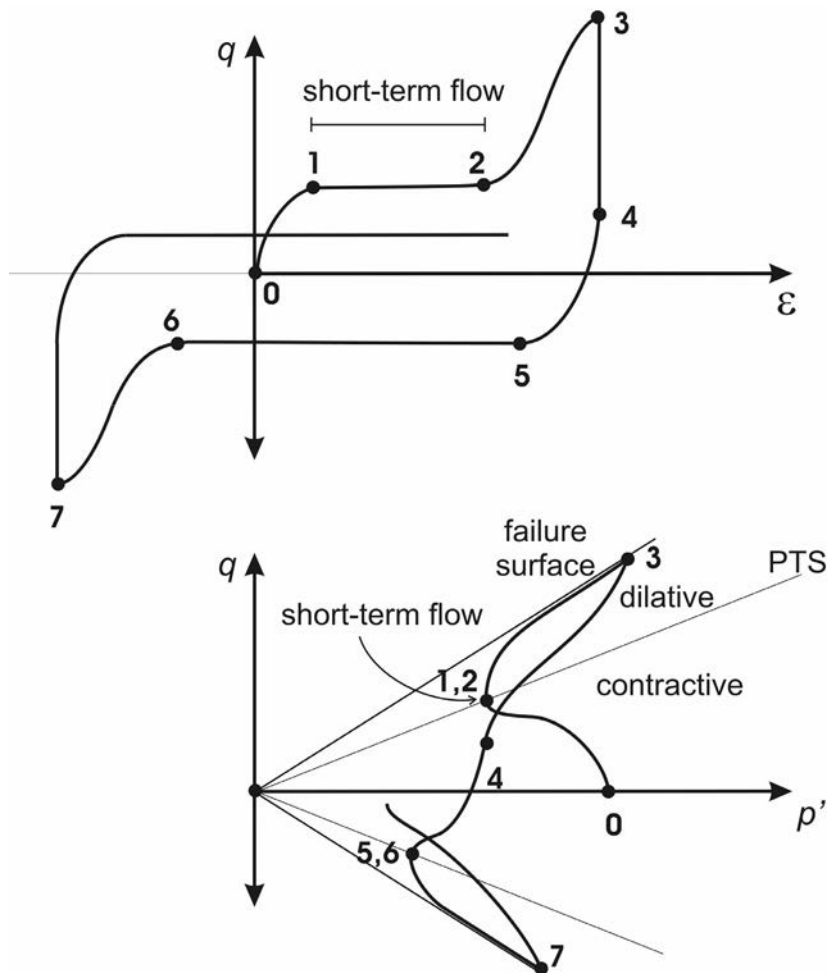


Figure 8. A typical stress path for cyclically loaded soil and the shear-strain relationship when it crosses the phase transformation surface (adapted from [15]).

It can be seen from the results of the two tested materials (Figure 5, Figure 6) that flow liquefaction is hardly likely to occur. There is a much higher risk of cyclic mobility, especially in the case of silty sand from the Sava river at Boštanj, which was found in the railway embankment. However, the dynamic load of a passing train might cause an increase in the pore pressure, leading to the occurrence of cyclic mobility. Two down-hole arrays with accelerometers and pore water-pressure sensors were established to enable monitoring of the dynamically loaded investigated soil response during and after the upheaval of the water and the saturation of the soil (Figure 9). The aim of the research was to define an effective procedure for an evaluation of the excess pore pressure. This would help to define a stress path during the dynamic loading and thus help with the prediction of any deformations.

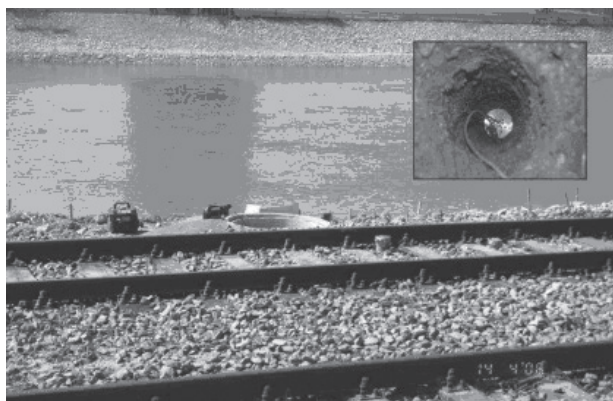


Figure 9. Railway embankment with a down-hole array and an accelerometer before the upheaval of the water.

4 AN ENERGY APPROACH TO EVALUATING THE EXCESS PORE PRESSURE

The stress path moves from its initial position due to changes in the shear stress, which are caused by loading, and due to the effective pressure decreasing during the cyclic loading (Figure 7). The effective pressure usually decreases due to the excess generation of pore pressure. We can be sure that an excess generation of pore pressure during the cyclic loading actually leads to stress-path movements and thus to changes in the soil strength and the stiffness.

Soil-grain rearrangements connected with soil-structure changes cause the pore pressure to increase when the soil contracts and decrease when it dilates. Changes

from contractive to dilative behavior and vice versa happen when the stress path crosses the PTS. Cyclic loading causes the irrecoverable contraction of the soil skeleton (Figure 1), which in the case of an undrained loading condition is accompanied by the permanent generation of excess pore pressure.

It is obvious that if a proper model for pore-pressure changes during dynamic loading were to exist, it would enable simple access to the modeling of the response of dynamically loaded saturated soils. The idea for the solution was taken from metal-fatigue analyses, for which purpose a cumulative damage hypothesis was developed [17]. Using this hypothesis an irregular dynamic loading can be converted into an equivalent damaging quantity, which makes it possible to evaluate a stress path's movement from its initial position, approaching the phase-transformation surface and the failure envelope. The energy dissipated during dynamic loading is chosen as the equivalent damaging quantity.

Quantification by seismologists of the energy released during earthquakes and the use of the energy dissipation in performance-based design in structural earthquake engineering argues for the use of energy for an excess pore-pressure evaluation procedure. The first steps toward the energy approach to excess pore-pressure evaluation were made using the relationships between the energy released during earthquakes and the sites where liquefaction occurred [18, 19]. Nemat-Nasser and Shokooh [20] presented governing differential equations relating energy dissipation to the densification of dry samples and to the generation of excess pore-water pressure in saturated samples. The dissipated energy density W was defined generally at time t as

$$W(t) = \frac{1}{\sigma'_0} \int_0^t \sigma_{ij} d\varepsilon_{ij}, \quad (1)$$

where σ_{ij} and ε_{ij} denote the stress and incremental strain tensors, respectively, t is the time in which the total dissipated energy is in question, and σ'_0 is an initial effective confining stress. In the case of the laboratory cyclic-loaded test results the dissipated energy density is defined as the area bounded by the hysteresis loops of the stress-strain curve (Figure 10).

Complementing the theoretical framework, several laboratory tests [21, 22, 23] as well as field measurements [24] have been performed to prove the relation. A typical general form, derived from the proposed expressions, could be written as

$$r_u = a \cdot W^b, \quad (2)$$

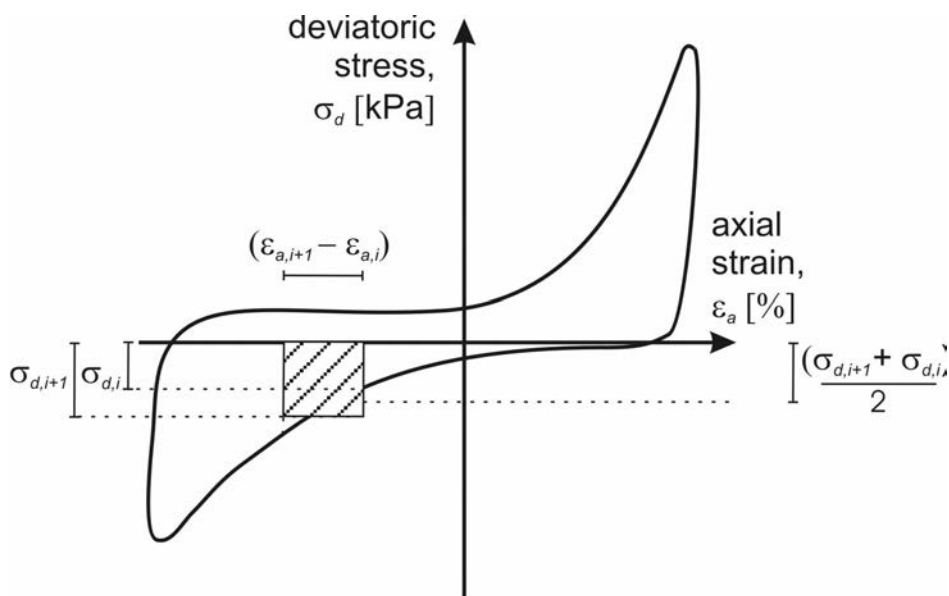


Figure 10. The dissipated energy per unit volume for a soil sample in case of cyclic triaxial test results.

where r_u denotes the pore-water pressure ratio ($=\Delta u/\sigma'_0$), Δu is the pore-water pressure change, while a and b are functions of the soil type, the relative density of the soil, the stress conditions, the initial soil-state parameters, etc. It should be mentioned again that the pore-water pressure change from Eq. 2 is caused only by the soil particles being rearranged and that this is a permanent change.

Lenart [25] divided the excess pore-water pressure generated during the dynamic loading into two parts: the temporary pore-pressure change and the residual pore-pressure change. Temporary pore-pressure changes can be observed as oscillations of the pore pressure in a normal pore-water pressure curve. They are caused by the transmission of compressive stresses onto the pore water. The origins of the pore-pressure oscillations and their effect upon the deformation behavior of the soil during dynamic loading are described in another paper [26].

Knowing the time function $F(t)$ of a normal component of dynamic loading to which the soil is subjected, it is possible to write the equation for evaluating the pore-pressure ratio, r_u (Eq. 3). The parameters k_r and k_t are the residual and temporary pore-pressure parameters, which depend upon the type of soil and its state. Their evaluation procedure is described in more detail in [25]. Using the least-square method, the best agreement between the proposed relationship and the empirical results

was found if a dissipated energy density, W , in Eq. 3 is raised to the power of $e/10$, where e means the base of the natural logarithm. As it is based on the dissipated energy density, the pore-pressure ratio calculated with Eq. 3 is independent of the loading frequency or the rate impacts in the case of the strain range typical for cyclic mobility or liquefaction [26].

$$r_u = (W)^{e/10} \cdot [k_r + k_t F(t)] \quad (3)$$

The proposed equation was tested in the case of two investigated materials. Figure 11 shows the approximated pore-water pressure changes compared to the experimental results in the case of the undrained cyclic triaxial test of the lacustrine carbonate silt sample. The loading took the form of a sine wave with the frequency of the loading being 1 Hz. To prove the proposed equations' independence from the frequency and the rate of loading, an irregular loading test was performed on a sample of silty sand from the Sava river. The loading simulated a seismic load recorded during the Petrovac earthquake in Montenegro in 1979. Good agreement was obtained between the results of the numerical analysis and the results of the laboratory tests (Figure 12).

Similar pore water pressure response due to dynamic loading was observed also, when other kind of materials were tested. An interesting increase in share of temporary pore water pressure changes was noticed in the case of highly porous snail soil [27].

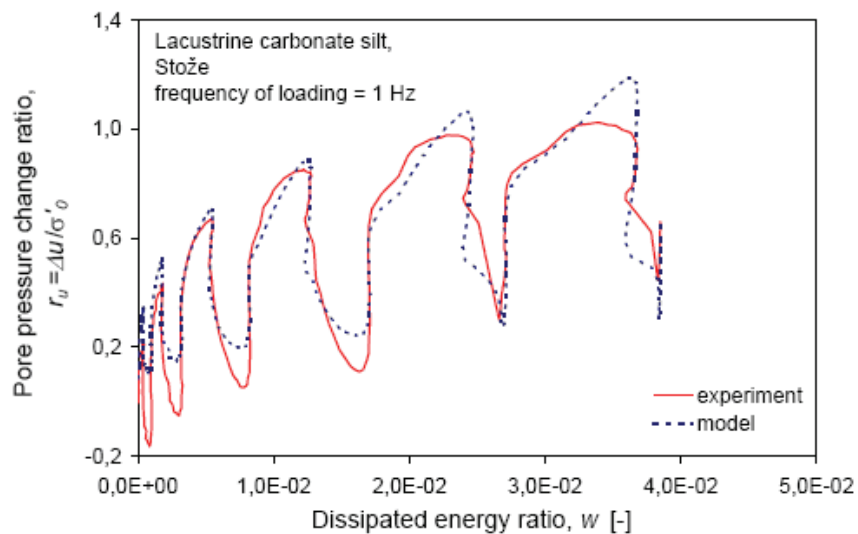


Figure 11. Pore-water pressure curve during an undrained cyclic triaxial test of lacustrine carbonate silt.

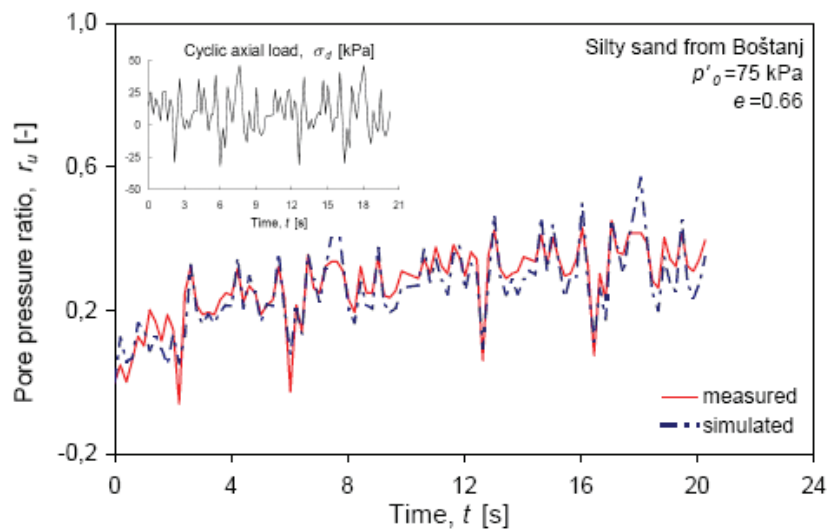


Figure 12. Results of an experiment compared to the modeling of an excess pore-water pressure generation.

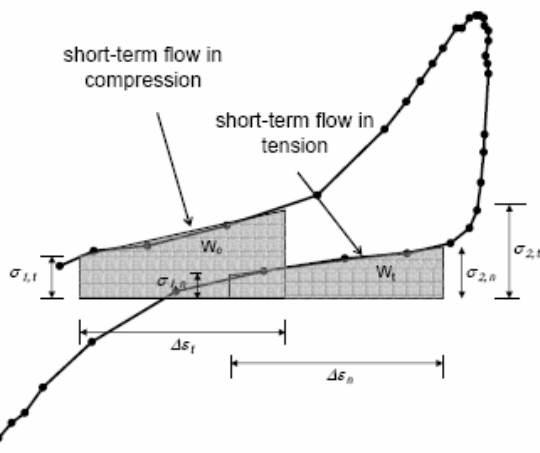


Figure 13. Evaluation of the energy dissipated during soil softening.

5 STRESS-STRAIN RELATION MODELING

If the generated excess pore-water pressure during the dynamic loading of saturated soil can be evaluated in the proper way, most of the work is done already. This makes it possible to evaluate the exact position of the stress path during the dynamic loading and thus to take into account the progressive degradation of the stiffness and the strength of the soil in an effective stress analysis.

The remaining problem is how to treat the phases of sudden soil softening and the significant regain in soil stiffness during cyclic loading at large deformations. Large deformations are limited by the soil hardening when the stress path crosses the PTS. A recent study [25]

showed that this highly yielded segment can be limited by the amount of dissipated energy. Figure 13 presents an evaluation of the energy dissipated during the softening phase. It has been found through research [25] that the dissipated energy during the softening phase in a single load cycle is linearly related to the residual pore-pressure ratio. Using this finding one can define the residual pore-pressure ratio at which soil softening due to the cyclic mobility effect starts.

The pore-pressure model presented in the previous section and the relation between the pore pressure and the energy dissipated during short-term flows when the cyclic mobility occurs were used [28] for simple stress-strain relation modeling. The results in case of the tested lacustrine carbonate samples are presented below.

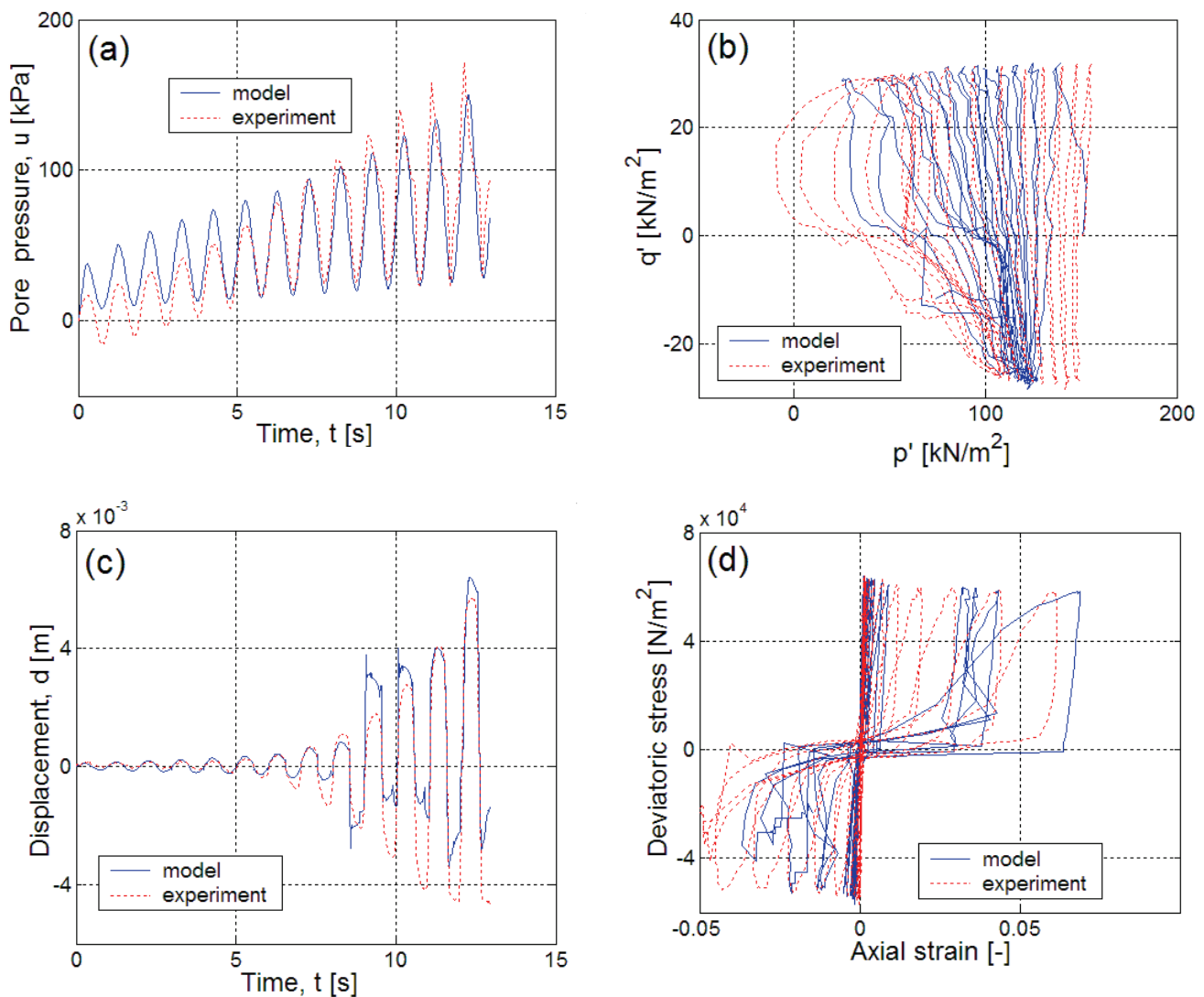


Figure 14. Typical simulation of the pore pressure (a), stress states (b), displacements (c) and stress-strain relation (d) for a cyclic triaxial test of a reconstituted sample of lacustrine carbonate silt.

6 CONCLUSION

Due to the large accompanying deformations and the possibility of severe damage, the response of dynamically loaded saturated soils has long attracted attention. Flow liquefaction and cyclic mobility are two phenomena that are often confused with each other. Their characteristics are described using two case histories from Slovenia: lacustrine carbonate silt from the Julian Alps and silty sand from the Sava river in Boštanj.

The effective stress decrease and the occurrence of large strain without any noticeable increase of the stress are common characteristics of flow liquefaction and cyclic mobility. An undrained loading condition, which is needed in both cases, is assumed to be present in saturated soil subjected to a rapid, dynamic load. Flow liquefaction appears suddenly when the residual strength of a soil is smaller than the static shear stress required for the equilibrium of a soil mass. On the other hand, cyclic mobility deformation develops incrementally during cyclic loading, mostly due to a decrease of the stiffness caused by a decrease of the effective stresses. It is important, therefore, to know the excess pore-water pressure generated during the cyclic loading of saturated soil, which impacts most upon the effective stresses in the soil.

An energy approach to saturated-soils response modeling during a dynamic load is presented in this paper. The energy concept is based on the idea that part of the energy of a dynamic load is dissipated into the soil. The density of the dissipated energy is represented by the area of the hysteretic strain-stress loop. The dissipated energy density is related to the generated excess pore-water pressure. The latter was divided into the temporary and residual generated excess pore-water pressure. Such a formulation helps to model very precisely the pore-water pressure oscillations during irregular dynamic loading.

The dissipated energy was evaluated during the soil-softening phase during cyclic mobility as well. Based on the observed linear relation between it and the residual excess pore-water pressure a promising attempt at modeling the response of dynamically loaded saturated soils was made.

ACKNOWLEDGMENTS

The author wishes to thank the Laboratory of Soil Mechanics and Prof. B. Žlender of the Faculty of Civil Engineering, University of Maribor, Slovenia, for supporting the study with experimental results. The

valuable help of G. Vilhar of the National Building and Civil Engineering Institute (ZAG) and the advice of Prof. J. Logar of the University of Ljubljana, were much appreciated. The financial support of the Ministry of Higher Education, Science and Technology of the Republic of Slovenia is gratefully acknowledged.

REFERENCES

- [1] Official web page of Holding Slovenske elektrarne HSE, <http://www.hse.si>, 2006
- [2] Lenart S, Petkovsek B (2006). Assessment of liquefaction potential of a loose soil in the base of a railroad, *Proceedings of the XIIIth Danube European Conference on Geotechnical Engineering*, Ljubljana, Vol. 2, 965-970
- [3] Lenart S, Fifer Bizjak K, Petkovsek B (2005). Report on the dynamic analysis of the critical cross section of the railway line at Bostanj accumulation basin. ZAG, P 810/05-750-2 (in Slovene)
- [4] Petkovšek, A. (2001). Geological-geotechnical Investigations of the Stože Landslide, *Ujma*, Ministrstvo za obrambo, Uprava RS za zaščito in reševanje, No. 14-15, 109-117
- [5] Lenart S. (2006). Deformation characteristics of lacustrine carbonate silt in the Julian Alps. *Soil Dynamics and Earthquake Engineering*, 26, 131-142
- [6] Lenart S., Žlender B. and Vilhar G. Liquefaction potential of lacustrine carbonate silt in the Julian Alps, *Soil Dynamics and Earthquake Engineering*, (to be published)
- [7] Žlender B. and Lenart S. (2005). Cyclic liquefaction potential of lacustrine carbonate silt from Julian Alps, *Acta Geotechnica Slovenica*, 2005/1, 22-31
- [8] Seed, H.B. and Idriss, I.M. (1971). Simplified procedure for evaluating soil liquefaction potential, *Jour. of the Soil Mechanics and Foundation Div.*, ASCE, Vol. 97, 1099-1119
- [9] Andrus, R.D., Stokoe, K.H. (2000). Liquefaction Resistance of Soils from Shear-Wave Velocity, *Journal of Geotechnical and Geoenvironmental Engineering*, Vol. 126, No. 11, 1015-1025
- [10] NCEER (1997). *Proceeding of the NCEER Workshop on Evaluation of Liquefaction Resistance of Soils*, Youd T.L. and Idriss I.M. (ed.), Technical Report NCEER-97-0022, National Center for Earthquake Engineering Research, State University of New York, Buffalo
- [11] Kramer, S.L. (1996). *Geotechnical Earthquake Engineering*, Publ. Prentice Hall, 348-422
- [12] Vaid, Y.P. and Chern, J.C. (1983) Effect of static shear on resistance of liquefaction, *Soils and Foundations*, Vol. 23, No. 1, 47-60

- [13] Ishihara, K. (1985). Stability of natural deposits during earthquakes, *Proceedings, 11th International Conference on Soil Mechanics and Foundation Engineering*, San Francisco, Vol. 1, 321-376
- [14] Youd, T.L. (1977). Discussion, *Soils and Foundations*, 17, No. 1, 82
- [15] Elgamal, A., Yang, Z., Parra, E., and Ragheb, A. (2003). Modeling of Cyclic Mobility in Saturated Cohesionless Soils, *Int. J. Plasticity*, 19, 883-905
- [16] Seed, H.B. and Lee, K.L. (1966). Liquefaction of saturated sands during cyclic loading, *J. Soil Mech. Found. Div.*, ASCE 92, SM6, 105-134
- [17] Miner, M.A. (1945). Cumulative damage in fatigue, *Trans. ASME* 67, A159-A164
- [18] Berrill, J.B. and Davis, R.O. (1985). Energy dissipation and seismic liquefaction of sands: Revised model, *Soils and Foundations*, Vol.25, No.2, 106-118
- [19] Trifunac, M.D. (1995). Empirical criteria for liquefaction in sands via standard penetration tests and seismic wave energy, *Soil Dynamics and Earthquake Engineering*, Vol. 14, 419-426
- [20] Nemat-Nasser, S. and Shokoh, A. (1979). A unified approach to densification and liquefaction of cohesionless sand in cyclic shearing, *Can. Geotech. J.*, 16(4), 659-678
- [21] Law, K.T., Cao, Y.L. and He, G.N. (1990). An energy approach for assessing seismic liquefaction potential, *Can. Geotech. J.*, 27, 320-329
- [22] Liang, L. (1995). *Development of an Energy Method for Evaluating the Liquefaction Potential of a Soil Deposit*, PhD Dissertation, Case Western Reserve University
- [23] Figueroa, J.L., Saada, A.S., Liang, L., and Dahisaria, N.M. (1994). Evaluation of Soil Liquefaction by Energy Principles, *Journal of Geotechnical Engineering*, ASCE, Vol. 120, No. 9, 1554-1569
- [24] Davis, R.O. and Berrill, J.B. (2001). Pore Pressure and Dissipated Energy in Earthquakes – Field Verification, *Journal of Geotechnical and Geoenvironmental Engineering*, Vol. 127, No. 3, 269-274
- [25] Lenart, S. (2006). *Numerical model for pore pressure change evaluation in soils with high liquefaction potential*, PhD Thesis, University of Ljubljana
- [26] Lenart, S. (2008). The use of dissipated energy at modeling of cyclic loaded saturated soils, *Earthquake Engineering: New Research*, Nova Science Publishers, Chapter 8
- [27] Žlender, B. and Trauner, L. (2007). The dynamic properties of the snail soil from the Ljubljana marsh, *Acta Geotechnica Slovenica*, 2007/2, Vol.4, 48-61
- [28] Lenart, S. and Logar, J. (2006). Numerical modeling of vertically loaded saturated soil, *Proc. of XIII. Danube-European Conference on Geotechnical Engineering*, 83-88

GREENOVA FUNKCIJA TANGENCIALNO OBREMENJENEGA HORIZONTALNO SLOJEVITEGA POLPROSTORA

TOMAŽ PLIBERŠEK IN ANDREJ UMEK

o avtorjih

Tomaž Pliberšek
Univerza v Mariboru,
Fakulteta za gradbeništvo
Smetanova 17, 2000 Maribor, Slovenija
E-pošta: tomaz.plibersek@uni-mb.si

Andrej Umek
Univerza v Mariboru,
Fakulteta za gradbeništvo
Smetanova 17, 2000 Maribor, Slovenija
E-pošta: umek@uni-mb.si

izvleček

V članku je obravnavan nov pristop k evalvaciji integralne predstavitve Greenove funkcije za slojevit pol-prostor, ki je na površini obremenjen s harmonično tangencialno točkovno silo. Enačbe gibanja razvežemo z uvedbo valovnih potencialov. Nevezane enačbe rešujemo tako, da jih s pomočjo predpostavljene odvisnosti od kotne koordinate in uvedbo Hanklove transformacije, pretvorimo v navadne diferencialne enačbe. Njihova rešitev in uvedba inverzne Hanklove transformacije vodita do integralne predstavitve za pomike na površini pol-prostora. Te nato izvedemo s pomočjo predlaganega tristopenjskega postopka. Najprej integrande razcepimo na dva dela, od katerih prvi po izvedeni integraciji vodi do singularnih pomikov, drugi del pa do regularnega dela pomikov. Opazimo, da je ta drugi del, potem ko uvedemo ustrezno izbrane razvejiščne reze in veljavnost integrandov s pomočjo analitičnega nadaljevanja razširimo s pozitivne realne osi Hanklovega parametra na njegovo celotno kompleksno ravnino, možno izvedemo s pomočjo konturne integracije za poljubno število slojev. Tako je ta del pomikov podan z rezidui integranda izvedenih v njegovih polih in integrali s končno razdaljo integracije vzdolž razvejiščih rezov. Te slednje z lahkoto izvedemo z zaželeno natančnostjo s pomočjo numerične integracije. Izbrani numerični rezultati dopolnjujejo matematična izvajanja.

ključne besede

elastodinamika, valovanje, Greenova funkcija, horizontalno slojevit polprostor, tangencialna koncentrirana sila

GREEN'S FUNCTION FOR TANGENTIALLY LOADED HORIZONTALY LAYERED HALF-SPACE

TOMAŽ PLIBERŠEK and ANDREJ UMEK

About the authors

Tomež Pliberšek
University of Maribor,
Faculty of Civil Engineering,
Smetanova 17, 2000 Maribor, Slovenia
E-mail: tomaz.plibersek@uni-mb.si

Andrej Umek
University of Maribor,
Faculty of Civil Engineering,
Smetanova 17, 2000 Maribor, Slovenia
E-mail: umek@uni-mb.si

Abstract

The topic of this paper is a novel evaluation of the integral representation of the surface Green's function for a layered half-space, loaded on its surface by a harmonic tangential point force. The equations of motions are reduced to wave equations by the introduction of wave potentials. The Hankel transform is applied to them and they are consecutively solved leading to the integral representation of surface displacements. They are consecutively evaluated by the proposed three step procedure. First the singularity is extracted. It is further noted that so obtained integrals, after suitably chosen branch cuts and analytic continuation of integrands are introduced, can be evaluated by contour integration for an arbitrary number of layers. They are, therefore, expressed by number of residues at the poles of integrand and the integrals along finite portions of the branch cuts. The latter ones can easily be evaluated to any desired accuracy leading to a closed form solution. Some numerical results corroborating the presented approach are given.

Keywords

elastodynamics, elastic wave propagation, Green's function, horizontally layered half-space, horizontal point load

1 INTRODUCTION

Modeling the elastodynamic characteristics of soil is required in a number of engineering problems, e.g. dynamic soil-structure interaction, dynamically loaded foundations etc. The soil is geometrically in prevalent number of cases modeled as a half space, which is, to be more realistic, endowed with some structure. As a starting point to determine the elastodynamic characteristics of soil one can use the fundamental solution or the Green's function. The use of the fundamental solution, which is known from the literature, results in the integrals over the whole surface of the half-space, interface between the soil and the superstructure and over the interfaces between the materials with different elastodynamic properties. Some of them are of infinite or semi-infinite extend. Their evaluations, which can be performed only numerically, represent the major difficulty of this approach. For practical evaluation the integration area has to be made finite, what results into introduction of the fictitious boundary, where the radiation conditions should be satisfied. The latter represent a demanding and not completely resolved problem e.g. Premrov [1]. The Green's function approach leads us to the integrals extending across the interface surface between the soil and the superstructure only. Their evaluation is straightforward and relatively easy to perform, once the Green's function is given. The difficulty of the problem is transferred to the determining and evaluating the Green's function itself.

The problematic of the homogeneous as well as the layered half-space has drawn the attention of considerable number of authors, not all of them can be mentioned here. The first elasticity solutions for whole- and half-space problems, static as well as dynamic ones have been obtained by Kelvin [2], Boussinesq [3], Cerruti [4], Lamb [5], Mindlin [6] and the others. The basic results on layered media were presented by Ewing et al. [7]. In more recent times the authors sought the solutions by two basically different approaches. On one side there are the approximate methods e.g. Luco's ray method [8, 9], Kausel's [10] thin layer method as well as BEM and FEM methods, their combinations e.g.

Gaitanaros et al. [11], Triantafyllidis [12], Auersch [13] and refinements e.g. Aubry et al. [14]. On the other hand we have methods leading to exact solutions in the form of integrals of semi- or infinite extend e.g. Vostroukhov [15] and Jin [16]. Their evaluation in the concept of FFT [17] concludes the latter approach. It, however, appears that the use of FFT like integration is a successful method to evaluate the Hankel transforms inversion integrals in the cases, where there are no singularities in the resulting displacement field. It must be however noted that in the case of the Green's function the vital information about its singularity comes from the portion of integration path, where the integration variable is very large or infinite. This fact makes in the case of the Green's function the FFT like evaluation of integrals less efficient.

Kobayashi et al. [18] considered the homogeneous, elastic half-space and succeeded to reduce the semi-infinite integrals representing the Green's function to a part containing the singularity, the residue at the Rayleigh pole and the integrals of finite extend along the properly chosen branch cut, which can be easily evaluated with any desired accuracy. Štrukelj et al. [19] succeeded to modify the Kobayashi's approach, so that it could be applied to the problem of vertically loaded layered half-space. The authors have first derived the Green's function for a single layer [20] and have demonstrated that under the assumption of infinite thickness of the layer their solutions lead to the Kobayashi's ones. Our decision to focus on the layer has also been motivated by the investigations of the mechanical properties of soils e.g. Žlender et al. [21] and [22], which are given at a point and can be easily generalized to a layer. This paper continues and completes the method to determine the surface Green's function for a layered half-space loaded with the harmonic force acting in any direction. It is motivated by the previous works by Kobayashi et al. [18, 23], Štrukelj et al. [19] and Pliberšek et al. [20]. The load acting in a general direction is decomposed into normal and tangential components with respect to the surface of the half-space, so that the problem of the latter one has to be dealt with only. First the general equations of motion for a single layer in Hankel transform domain are derived by adapting the Vostroukhov's [15] approach and then transformed back into the geometrical domain. These single layer solutions are then combined into the solution for a layered half-space making use of the continuity conditions on the interfaces between the layers and boundary conditions on the surface of the half-space. It is proven that the basic mathematical properties of these solutions do not depend on the number of layers. They are the same for a homogeneous half-space as well as for the half-space with any number of layers.

The inverse Hankel transform integrals appearing in the Green's function can be therefore for any number of layers expressed with part proportional to r^{-1} , integrals of finite extend along the properly chosen branch cut and some residues at the poles of the integrand. The closed form solutions, obtained by our approach, for the Green's function of the tangentially loaded layered half-space are consecutively presented graphically for some selected number of cases.

2 METHOD OF ANALYSIS

2.1 GOVERNING EQUATIONS FOR A LAYER

We consider a horizontally layered half-space, which consist of n layers on a half-space, as shown on the Fig. 1. The material properties of each layer and of the underlying half-space are assumed to be isotropic and homogeneous. Shear modulus μ_i , Poisson's ratio ν_i , mass density ρ_i and the dumping coefficient $\hat{\mu}_i$ are the material constants of i -th layer. The homogeneous half-space is labeled as the layer number H .

The global, cylindrical co-ordinate system and the local cylindrical co-ordinate systems having their origins at the top of each layer are introduced. The model is subjected on its free surface to a concentrated tangential point load, which varies harmonically in time. Without loss of generality, it is assumed that it acts in the direction of positive x -axis. The governing equation for each homogeneous, elastic layer is the well known [24] reduced Navier's equation of motion in frequency domain:

$$\frac{\mu_i}{\rho_i} \nabla^2 \bar{u}_i + \frac{\lambda_i + \mu_i}{\rho_i} \bar{\nabla} \bar{\nabla} \cdot \bar{u}_i = -\omega^2 \bar{u}_i \quad ; \quad i \in [1, 2, \dots, n, H]. \quad (1)$$

The boundary conditions on the free surface of the half-space can be in the cylindrical coordinates written as:

$$\sigma_{rz,1}(r, \vartheta, 0, \omega) = \bar{\sigma}_{rz}(r, 0, \omega) \cdot \cos(\vartheta) = -\frac{Q(\omega) \cdot \delta(r)}{2 \cdot \pi \cdot r} \cdot \cos(\vartheta) \quad (2)$$

$$\sigma_{\vartheta z,1}(r, \vartheta, z, \omega) = \bar{\sigma}_{\vartheta z}(r, z, \omega) \cdot \sin(\vartheta) = \frac{Q(\omega) \cdot \delta(r)}{2 \cdot \pi \cdot r} \cdot \sin(\vartheta) \quad (3)$$

$$\sigma_{zz,1}(r, \vartheta, 0, \omega) = 0 \quad (4)$$

where $\delta(r)$ is the Dirac delta function. The continuity equation along the interfaces of consecutive layers, where perfect bonding is assumed, and radiation conditions for $r \rightarrow \infty$ complete the definition of boundary value problem under consideration.

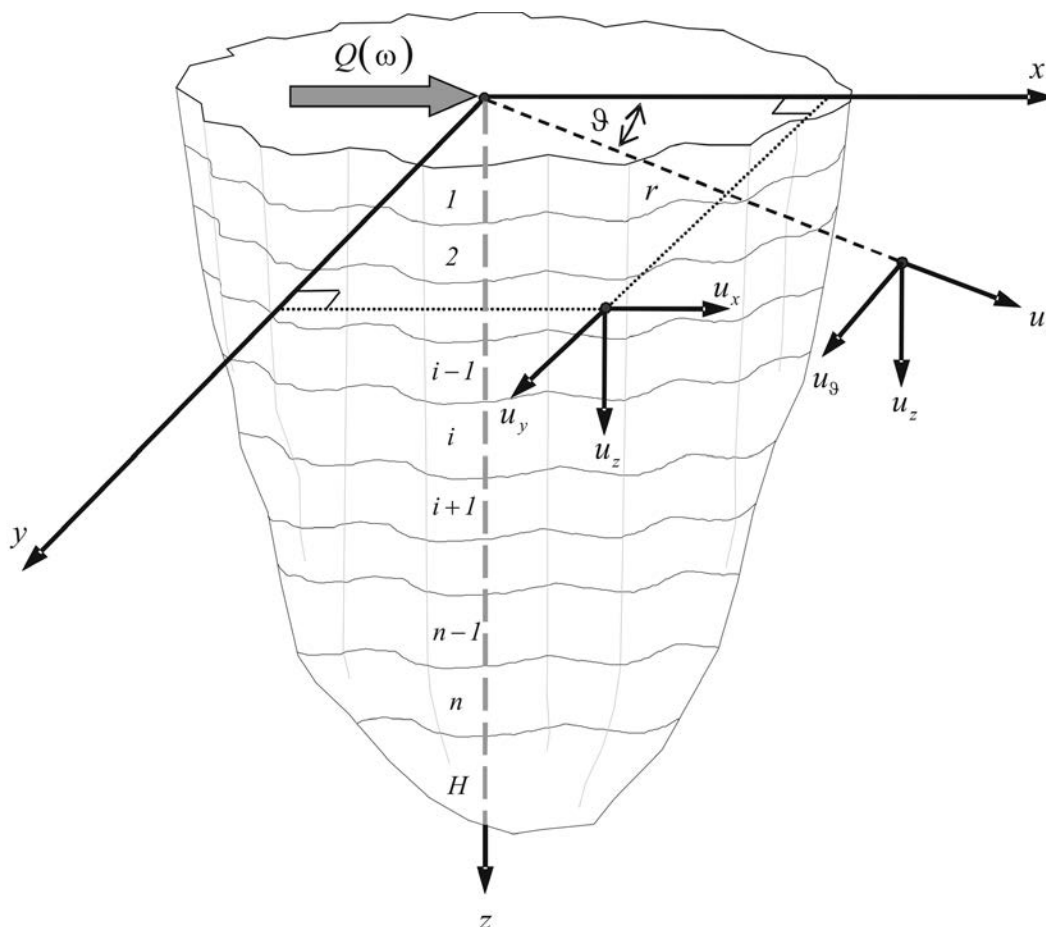


Figure 1. A horizontally layered half-space subjected to a surface horizontal harmonic point load.

The geometry of the above defined boundary-value problem is axi-symmetric. Therefore the ϑ -dependence of the problem is governed by the ϑ -dependence of the loading only. Due to very simple ϑ -dependence as a first step in the solution procedure reduced stresses:

$$\sigma_{rz,i}(r, \vartheta, z, \omega) = \bar{\sigma}_{rz,i}(r, z, \omega) \cdot \cos(\vartheta) \quad ; \quad i \in [1, 2, \dots, n, H] \quad (5)$$

$$\sigma_{\vartheta z,i}(r, \vartheta, z, \omega) = \bar{\sigma}_{\vartheta z,i}(r, z, \omega) \cdot \sin(\vartheta) \quad ; \quad i \in [1, 2, \dots, n, H] \quad (6)$$

$$\sigma_{zz,i}(r, \vartheta, z, \omega) = \bar{\sigma}_{zz,i}(r, z, \omega) \cdot \cos(\vartheta) \quad ; \quad i \in [1, 2, \dots, n, H] \quad (7)$$

and reduced displacements:

$$u_{r,i}(r, \vartheta, z, \omega) = \bar{u}_{r,i}(r, z, \omega) \cdot \cos(\vartheta) \quad ; \quad i \in [1, 2, \dots, n, H] \quad (8)$$

$$u_{\vartheta,i}(r, \vartheta, z, \omega) = \bar{u}_{\vartheta,i}(r, z, \omega) \cdot \sin(\vartheta) \quad ; \quad i \in [1, 2, \dots, n, H] \quad (9)$$

$$u_{z,i}(r, \vartheta, z, \omega) = \bar{u}_{z,i}(r, z, \omega) \cdot \cos(\vartheta) \quad ; \quad i \in [1, 2, \dots, n, H] \quad (10)$$

are introduced. In the second step we make use of the Helmholtz wave potentials [25] to decouple the equations of motion (1):

$$\bar{u}_i = \bar{\nabla} \cdot \bar{\varphi}_i + \bar{\nabla} \times \bar{\psi}_i \quad ; \quad i \in [1, 2, \dots, n, H] \quad (11)$$

The vector potential $\bar{\psi}_i$ should in addition satisfy the constraint condition:

$$\bar{\nabla} \bullet \bar{\psi}_i = 0 \quad . \quad (12)$$

As in the case of displacements and stresses we introduce the reduced wave potentials:

$$\varphi_i(r, \vartheta, z, \omega) = \bar{\varphi}_i(r, z, \omega) \cdot \cos(\vartheta) \quad ; \quad i \in [1, 2, \dots, n, H] \quad (13)$$

$$\psi_{r,i}(r, \vartheta, z, \omega) = \bar{\psi}_{r,i}(r, z, \omega) \cdot \sin(\vartheta) \quad ; \quad i \in [1, 2, \dots, n, H] \quad (14)$$

$$\psi_{\vartheta,i}(r, \vartheta, z, \omega) = \bar{\psi}_{\vartheta,i}(r, z, \omega) \cdot \cos(\vartheta) \quad ; \quad i \in [1, 2, \dots, n, H] \quad (15)$$

$$\psi_{z,i}(r, \vartheta, z, \omega) = \bar{\psi}_{z,i}(r, z, \omega) \cdot \sin(\vartheta) \quad ; \quad i \in [1, 2, \dots, n, H] \quad (16)$$

The substitution of Eqs. (13) to (16) into equations of motion (1) yields:

$$\left[\frac{\partial^2 \bar{\varphi}_i}{\partial r^2} + \frac{1}{r} \cdot \frac{\partial \bar{\varphi}_i}{\partial r} - \frac{1}{r^2} \cdot \bar{\varphi}_i + \frac{\partial^2 \bar{\varphi}_i}{\partial z^2} \right] + k_{L,i}^2 \cdot \bar{\varphi}_i = 0 \quad ; \quad i \in [1, 2, \dots, n, H] \quad (17)$$

$$\left[\frac{\partial^2}{\partial r^2} + \frac{1}{r} \cdot \frac{\partial}{\partial r} - \frac{2}{r^2} + \frac{\partial^2}{\partial z^2} \right] \cdot \bar{\psi}_{r,i} + \frac{2}{r^2} \cdot \bar{\psi}_{\theta,i} + k_{T,i}^2 \cdot \bar{\psi}_{r,i} = 0 \quad ; \quad i \in [1, 2, \dots, n, H] \quad (18)$$

$$\left[\frac{\partial^2}{\partial r^2} + \frac{1}{r} \cdot \frac{\partial}{\partial r} - \frac{2}{r^2} + \frac{\partial^2}{\partial z^2} \right] \cdot \bar{\psi}_{\theta,i} + \frac{2}{r^2} \cdot \bar{\psi}_{r,i} + k_{T,i}^2 \cdot \bar{\psi}_{\theta,i} = 0 \quad ; \quad i \in [1, 2, \dots, n, H] \quad (19)$$

$$\left[\frac{\partial^2}{\partial r^2} + \frac{1}{r} \cdot \frac{\partial}{\partial r} - \frac{1}{r^2} + \frac{\partial^2}{\partial z^2} \right] \cdot \bar{\psi}_{z,i} + k_{T,i}^2 \cdot \bar{\psi}_{z,i} = 0 \quad ; \quad i \in [1, 2, \dots, n, H] \quad (20)$$

$$\bar{\psi}_{r,i} - \bar{\psi}_{\theta,i} + r \cdot \left[\frac{\partial \bar{\psi}_{r,i}}{\partial r} + \frac{\partial \bar{\psi}_{z,i}}{\partial z} \right] = 0 \quad ; \quad i \in [1, 2, \dots, n, H] \quad . \quad (21)$$

We note that the above equation system contains two decoupled equations (17) and (20) and two still coupled equations (18) and (19). To decouple the latter ones we add them and subtract them and introduce two new reduced wave potentials $\bar{\chi}_i$ and $\bar{\kappa}_i$ as:

$$\bar{\chi}_i = \bar{\psi}_{r,i} + \bar{\psi}_{\theta,i} \quad ; \quad \bar{\kappa}_i = \bar{\psi}_{r,i} - \bar{\psi}_{\theta,i} \quad , \quad (22)$$

where $i \in [1, 2, \dots, n, H]$ and the equations (18) and (19) are replaced by:

$$\left[\frac{\partial^2}{\partial r^2} + \frac{1}{r} \cdot \frac{\partial}{\partial r} + \frac{\partial^2}{\partial z^2} \right] \cdot \bar{\chi}_i + k_{T,i}^2 \cdot \bar{\chi}_i = 0 \quad ; \quad i \in [1, 2, \dots, n, H] \quad (23)$$

$$\left[\frac{\partial^2}{\partial r^2} + \frac{1}{r} \cdot \frac{\partial}{\partial r} - \frac{4}{r^2} + \frac{\partial^2}{\partial z^2} \right] \cdot \bar{\kappa}_i + k_{T,i}^2 \cdot \bar{\kappa}_i = 0 \quad ; \quad i \in [1, 2, \dots, n, H] \quad (24)$$

and the compatibility condition becomes:

$$\bar{\kappa}_i + r \cdot \left[\frac{1}{2} \cdot \frac{\partial (\bar{\chi}_i + \bar{\kappa}_i)}{\partial r} + \frac{\partial \bar{\psi}_{z,i}}{\partial z} \right] = 0 \quad ; \quad i \in [1, 2, \dots, n, H] \quad . \quad (25)$$

The most efficient way to solve the boundary value problem under consideration is by the introduction of Hankel integral transform.

2.2 HANKEL TRANSFORM AND SOLUTIONS IN HANKEL TRANSFORM DOMAIN

To solve the equations of motion (17), (20), (23) and (24) for each layer with appropriate boundary conditions (2) to (4) and continuity conditions Hankel integral transform $r \rightarrow \xi$:

$$\check{f}^{Hn}(\xi) = H_n[f(r)] = \int_0^\infty f(r) \cdot J_n(\xi r) \cdot r \cdot dr \quad (26)$$

and its inverse $\xi \rightarrow r$:

$$f(r) = H_n^{-1}[\check{f}^{Hn}(\xi)] = \int_0^\infty \check{f}^{Hn}(\xi) \cdot J_n(\xi r) \cdot \xi \cdot d\xi \quad , \quad (27)$$

are introduced [26]. n is the order of the transform and $J_n(\xi r)$ is Bessel function of the first kind and order n . To transform the equations of motion to their canonical form the integral transforms of different orders are employed. Equations (17) and (20) are transformed through Hankel transform of order 1, equation (23) of order 0 and equation (24) of order 2. This yields the following system of equations:

$$\frac{d^2 \check{\varphi}_i^{H_1}(\xi)}{d\xi^2} - (\xi^2 - k_{L,i}^2) \cdot \check{\varphi}_i^{H_1}(\xi) = 0 \quad ; \quad i \in [1, 2, \dots, n, H] \quad (28)$$

$$\frac{d^2 \check{\chi}_i^{H_0}(\xi)}{d\xi^2} - (\xi^2 - k_{T,i}^2) \cdot \check{\chi}_i^{H_0}(\xi) = 0 \quad ; \quad i \in [1, 2, \dots, n, H] \quad (29)$$

$$\frac{d^2 \check{\kappa}_i^{H_2}(\xi)}{d\xi^2} - (\xi^2 - k_{T,i}^2) \cdot \check{\kappa}_i^{H_2}(\xi) = 0 \quad ; \quad i \in [1, 2, \dots, n, H] \quad (30)$$

$$\frac{d^2 \check{\psi}_{z,i}^{H_1}(\xi)}{d\xi^2} - (\xi^2 - k_{T,i}^2) \cdot \check{\psi}_{z,i}^{H_1}(\xi) = 0 \quad ; \quad i \in [1, 2, \dots, n, H] \quad . \quad (31)$$

The solutions of the above equations can be written as:

$$\check{\varphi}_i^{H_1} = C_{1,i} \cdot e^{\alpha_i \cdot z_i} + C_{2,i} \cdot e^{-\alpha_i \cdot z_i} \quad ; \quad i \in [1, 2, \dots, n, H] \quad (32)$$

$$\check{\chi}_i^{H_0} = C_{3,i} \cdot e^{\beta_i \cdot z_i} + C_{4,i} \cdot e^{-\beta_i \cdot z_i} \quad ; \quad i \in [1, 2, \dots, n, H] \quad (33)$$

$$\check{\kappa}_i^{H_2} = C_{5,i} \cdot e^{\beta_i \cdot z_i} + C_{6,i} \cdot e^{-\beta_i \cdot z_i} \quad ; \quad i \in [1, 2, \dots, n, H] \quad (34)$$

$$\check{\psi}_{z,i}^{H_1} = C_{7,i} \cdot e^{\beta_i \cdot z_i} + C_{8,i} \cdot e^{-\beta_i \cdot z_i} \quad ; \quad i \in [1, 2, \dots, n, H] \quad , \quad (35)$$

where:

$$\alpha_i = \sqrt{\xi^2 - k_{L,i}^2} \quad ; \quad \beta_i = \sqrt{\xi^2 - k_{T,i}^2} \quad ; \quad i \in [1, 2, \dots, n, H] \quad . \quad (36)$$

The constraint condition the transformed wave potentials must satisfy is obtained from equation (25). This yields:

$$\xi \cdot \check{\check{\kappa}}_i^{H_2}(\xi, z, \omega) - \xi \cdot \check{\check{\chi}}_i^{H_0}(\xi, z, \omega) + 2 \cdot \frac{\partial \check{\check{\psi}}_{z,i}^{H_1}(\xi, z, \omega)}{\partial z} = 0 \quad ; \quad i \in [1, 2, \dots, n, H] \quad (37)$$

The yet unknown integration constants C_{ij} ; $i \in [1, 2, \dots, 8]$ and $j \in [1, 2, \dots, n, H]$ will be determined from boundary, continuity and radiation conditions. For this purpose the reduced displacement components are expressed through the transformed wave potentials as:

$$\begin{aligned} \bar{u}_{r,i}(r, z, \omega) = & \frac{1}{2} \cdot \int_0^\infty \xi \cdot \left\{ \left[\xi \cdot \check{\check{\varphi}}_i^{H_1}(\xi, z, \omega) + \xi \cdot \check{\check{\psi}}_{z,i}^{H_1}(\xi, z, \omega) - \frac{\partial \check{\check{\kappa}}_i^{H_2}(\xi, z, \omega)}{\partial z} + \right. \right. \\ & \left. \left. - \frac{2}{\xi} \cdot \frac{\partial^2 \check{\check{\psi}}_{z,i}^{H_1}(\xi, z, \omega)}{\partial z^2} \right] \cdot J_0(\xi r) + \left[-\xi \cdot \check{\check{\varphi}}_i^{H_1}(\xi, z, \omega) + \xi \cdot \check{\check{\psi}}_{z,i}^{H_1}(\xi, z, \omega) + \right. \right. \\ & \left. \left. + \frac{\partial \check{\check{\kappa}}_i^{H_2}(\xi, z, \omega)}{\partial z} \right] \cdot J_2(\xi r) \right\} \cdot d\xi \quad ; \quad i \in [1, 2, \dots, n, H] \end{aligned} \quad (38)$$

$$\begin{aligned} \bar{u}_{\theta,i}(r, z, \omega) = & \frac{1}{2} \cdot \int_0^\infty \xi \cdot \left\{ - \left[\xi \cdot \check{\check{\varphi}}_i^{H_1}(\xi, z, \omega) - \frac{\partial \check{\check{\kappa}}_i^{H_2}(\xi, z, \omega)}{\partial z} + \right. \right. \\ & \left. \left. - \frac{2}{\xi} \cdot \frac{\partial^2 \check{\check{\psi}}_{z,i}^{H_1}(\xi, z, \omega)}{\partial z^2} + \xi \cdot \check{\check{\psi}}_{z,i}^{H_1}(\xi, z, \omega) \right] \cdot J_0(\xi r) + \left[-\xi \cdot \check{\check{\varphi}}_i^{H_1}(\xi, z, \omega) \right. \right. \\ & \left. \left. + \frac{\partial \check{\check{\kappa}}_i^{H_2}(\xi, z, \omega)}{\partial z} + \xi \cdot \check{\check{\psi}}_{z,i}^{H_1}(\xi, z, \omega) \right] \cdot J_2(\xi r) \right\} \cdot d\xi \quad ; \quad i \in [1, 2, \dots, n, H] \end{aligned} \quad (39)$$

$$\begin{aligned} \bar{u}_{z,i}(r, z, \omega) = & \int_0^\infty \xi \cdot \left[\frac{\partial \check{\check{\varphi}}_i^{H_1}(\xi, z, \omega)}{\partial z} - \frac{\partial \check{\check{\psi}}_{z,i}^{H_1}(\xi, z, \omega)}{\partial z} + \right. \\ & \left. - \xi \cdot \check{\check{\kappa}}_i^{H_2}(\xi, z, \omega) \right] \cdot J_1(\xi r) \cdot d\xi \quad ; \quad i \in [1, 2, \dots, n, H]. \end{aligned} \quad (40)$$

From the above expressions strains are derived and introduced into the constitutive equation for linear,

homogeneous and isotropic solid. The pertinent reduced stresses are then given as:

$$\begin{aligned} \bar{\sigma}_{rz,i}(r, z, \omega) = & \frac{\mu_i}{2} \cdot \left\{ \int_0^\infty \xi \cdot \left\{ \left[2 \cdot \xi \cdot \frac{\partial \check{\check{\varphi}}_i^{H_1}(\xi, z, \omega)}{\partial z} - \frac{2}{\xi} \cdot \frac{\partial^3 \check{\check{\psi}}_{z,i}^{H_1}(\xi, z, \omega)}{\partial z^3} + \right. \right. \right. \\ & \left. \left. - \frac{\partial^2 \check{\check{\kappa}}_i^{H_2}(\xi, z, \omega)}{\partial z^2} - \xi^2 \cdot \check{\check{\kappa}}_i^{H_2}(\xi, z, \omega) \right] \cdot J_0(\xi r) + \right. \\ & \left. + \left[-2 \cdot \xi \cdot \frac{\partial \check{\check{\varphi}}_i^{H_1}(\xi, z, \omega)}{\partial z} + 2 \cdot \xi \cdot \frac{\partial \check{\check{\psi}}_{z,i}^{H_1}(\xi, z, \omega)}{\partial z} + \right. \right. \\ & \left. \left. + \frac{\partial^2 \check{\check{\kappa}}_i^{H_2}(\xi, z, \omega)}{\partial z^2} + \xi^2 \cdot \check{\check{\kappa}}_i^{H_2}(\xi, z, \omega) \right] \cdot J_2(\xi r) \right\} \cdot d\xi \quad ; \quad i \in [1, 2, \dots, n, H] \end{aligned} \quad (41)$$

$$\begin{aligned} \bar{\sigma}_{z\vartheta,i}(r,z,\omega) = & \frac{\mu_i}{2} \cdot \left\{ \int_0^\infty \xi \cdot \left[-2 \cdot \xi \cdot \frac{\partial \check{\check{\varphi}}_i^{H_1}(\xi,z,\omega)}{\partial z} + \xi^2 \cdot \check{\check{\kappa}}_i^{H_2}(\xi,z,\omega) + \right. \right. \\ & \left. \left. + \frac{2}{\xi} \cdot \frac{\partial^3 \check{\check{\psi}}_{z,i}^{H_1}(\xi,z,\omega)}{\partial z^3} + \frac{\partial^2 \check{\check{\kappa}}_i^{H_2}(\xi,z,\omega)}{\partial z^2} \right] \cdot J_0(\xi r) + \right. \\ & \left. + \left[-2 \cdot \xi \cdot \frac{\partial \check{\check{\varphi}}_i^{H_1}(\xi,z,\omega)}{\partial z} + \frac{\partial^2 \check{\check{\kappa}}_i^{H_2}(\xi,z,\omega)}{\partial z^2} + 2 \cdot \xi \cdot \frac{\partial \check{\check{\psi}}_{z,i}^{H_1}(\xi,z,\omega)}{\partial z} + \right. \right. \\ & \left. \left. + \xi^2 \cdot \check{\check{\kappa}}_i^{H_2}(\xi,z,\omega) \right] \cdot J_2(\xi r) \right\} \cdot d\xi \quad ; \quad i \in [1,2,\dots,n,H] \end{aligned} \tag{42}$$

$$\begin{aligned} \bar{\sigma}_{zz,i}(r,z,\omega) = & \mu_i \cdot \int_0^\infty \xi \cdot \left\{ \left(\frac{\lambda_i + 2 \cdot \mu_i}{\mu_i} \right) \cdot \left[\frac{\partial^2 \check{\check{\varphi}}_i^{H_1}(\xi,z,\omega)}{\partial z^2} - \xi^2 \cdot \check{\check{\varphi}}_i^{H_1}(\xi,z,\omega) \right] + \right. \\ & \left. + 2 \cdot \xi^2 \cdot \check{\check{\varphi}}_i^{H_1}(\xi,z,\omega) - 2 \cdot \xi \cdot \frac{\partial \check{\check{\kappa}}_i^{H_2}(\xi,z,\omega)}{\partial z} + \right. \\ & \left. - 2 \cdot \frac{\partial^2 \check{\check{\psi}}_{z,i}^{H_1}(\xi,z,\omega)}{\partial z^2} \right\} \cdot J_1(\xi r) \cdot d\xi \quad ; \quad i \in [1,2,\dots,n,H]. \end{aligned} \tag{43}$$

The equations (38) to (43) permit us to construct a linear, algebraic equation system in integration constants C_{ij} as unknowns. It is worth-while to note that in these equations due to constraint condition (37) only three wave potentials are appearing, what results in six integration constants per layer or underlying half-space. If a branch cut in the complex ξ -plane is introduced, which makes $\text{Re}(\alpha_i) > 0$ and $\text{Re}(\beta) > 0$ on the real positive ξ -axis, then the radiation conditions demand:

$$C_{1,H} = C_{5,H} = C_{7,H} = 0 \quad . \tag{44}$$

The boundary conditions on the surface of the half-space are given by equations (2) to (4) and for the continuity condition perfect bonding between the layers and the underlying half-space i.e. the continuity of displacements and stresses across the interfaces, is

assumed. Thus the boundary and continuity conditions result in $6 \cdot n + 3$ equations for the same number of unknown integration constants C_{ij} . For the reason of in the forthcoming paragraph introduced solution procedure we must study some properties of the matrix of this equation system and its submatrices. To simplify the further mathematical derivation some dimensionless variables and constants are introduced:

$$\begin{aligned} \xi = \eta \cdot k_{T1} \quad ; \quad \vartheta_i = \frac{k_{Ti}}{k_{T1}} \quad ; \quad \gamma_i = \frac{k_{Li}}{k_{T1}} \quad ; \quad \mu_{i,1} = \frac{\mu_i}{\mu_1} \\ \alpha_i = k_{T1} \cdot \bar{\alpha}_i \quad ; \quad \beta_i = k_{T1} \cdot \bar{\beta}_i \quad ; \quad t_i = k_{T1} \cdot h_i \quad ; \quad i \in [1,2,\dots,n,H]. \end{aligned} \tag{45}$$

We begin the derivation of the equation system with the boundary conditions defined on the upper surface of the first layer shown on the Fig. 2.

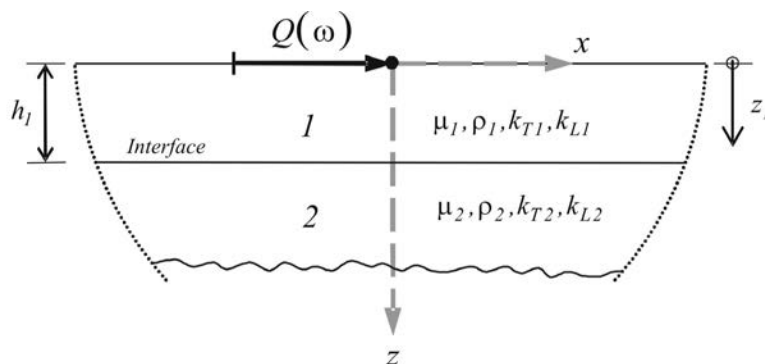


Figure 2. Material and geometrical properties of the first layer.

We introduce the expressions for stresses (41) to (43) into the transformed boundary conditions (2) to (4) and take into account the equation (45). This yields:

$$\mu_1 \cdot k_{T1}^2 \cdot \left\{ -2 \cdot \eta \cdot \bar{\alpha}_1 \cdot [C_{1,1} - C_{1,2}] + (\eta^2 + \bar{\beta}_1^2) \cdot [C_{1,3} + C_{1,4}] + \frac{2}{\eta} \cdot \bar{\beta}_1^3 \cdot [C_{1,5} - C_{1,6}] \right\} = \frac{Q(\omega)}{\pi} \quad (46)$$

$$\mu_1 \cdot k_{T1}^2 \cdot \left\{ -2 \cdot \eta \cdot \bar{\alpha}_1 \cdot [C_{1,1} - C_{1,2}] + (\eta^2 + \bar{\beta}_1^2) \cdot [C_{1,3} + C_{1,4}] + 2 \cdot \eta \cdot \bar{\beta}_1 \cdot [C_{1,5} - C_{1,6}] \right\} = 0 \quad (47)$$

$$\mu_1 \cdot k_{T1}^2 \cdot \left\{ \left[\frac{1}{2} \cdot \frac{(\lambda_1 + 2 \cdot \mu_1)}{\mu_1} \cdot (\bar{\alpha}_1^2 - \eta^2) + \eta^2 \right] \cdot [C_{1,1} + C_{1,2}] + -\eta \cdot \bar{\beta}_1 \cdot [C_{1,3} - C_{1,4}] - \bar{\beta}_1^2 \cdot [C_{1,5} + C_{1,6}] \right\} = 0 \quad (48)$$

The other equations follow from continuity conditions on the interfaces between layers and the n^{th} layer and the underlying half-space respectively. The interface between the i^{th} and the $(i+1)^{st}$ layer is depicted in Fig. 3.

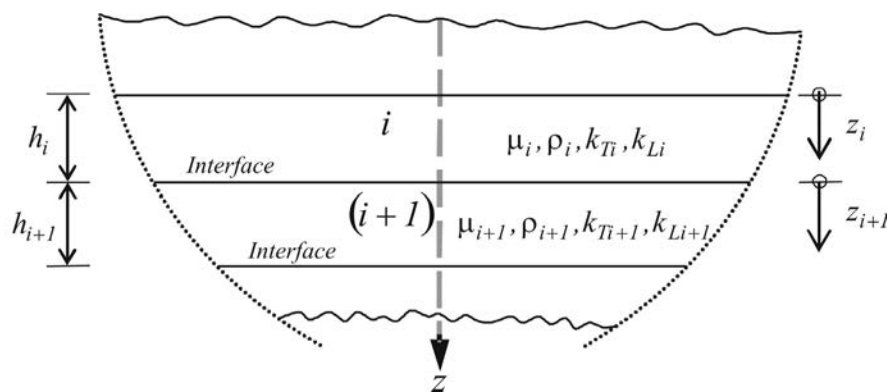


Figure 3. Material and geometrical properties of i^{th} and $(i+1)^{st}$ layer.

Introduction of equations for the displacements and the stresses (38) to (43) into continuity equations leads to:

$$\begin{aligned} \check{\sigma}_{zz,1} \Big|_{z_i=h_i} - \check{\sigma}_{zz,i+1} \Big|_{z_{i+1}=0} &= \mu_{i,1} \cdot \left\{ \left[\frac{1}{2} \cdot \frac{(\lambda_i + 2 \cdot \mu_i)}{\mu_i} \cdot (\bar{\alpha}_i^2 - \eta^2) + \eta^2 \right] \cdot [C_{i,1} \cdot e^{\bar{\alpha}_i \cdot t_i} + C_{i,2} \cdot e^{-\bar{\alpha}_i \cdot t_i}] - \eta \cdot \bar{\beta}_i \cdot [C_{i,3} \cdot e^{\bar{\beta}_i \cdot t_i} - C_{i,4} \cdot e^{-\bar{\beta}_i \cdot t_i}] - \bar{\beta}_i^2 \cdot [C_{i,5} \cdot e^{\bar{\beta}_i \cdot t_i} + C_{i,6} \cdot e^{-\bar{\beta}_i \cdot t_i}] \right\} + \\ -\mu_{i+1,1} \cdot \left\{ \left[\frac{1}{2} \cdot \frac{(\lambda_{i+1} + 2 \cdot \mu_{i+1})}{\mu_{i+1}} \cdot (\bar{\alpha}_{i+1}^2 - \eta^2) + \eta^2 \right] \cdot [C_{i+1,1} + C_{i+1,2}] + \right. & \quad (49) \\ \left. -\eta \cdot \bar{\beta}_{i+1} \cdot [C_{i+1,3} - C_{i+1,4}] - \bar{\beta}_{i+1}^2 \cdot [C_{i+1,5} + C_{i+1,6}] \right\} &= 0 \end{aligned}$$

$$\begin{aligned} \check{\sigma}_{z\theta,i} \Big|_{z_i=h_i} - \check{\sigma}_{z\theta,i+1} \Big|_{z_{i+1}=0} &= -\mu_{i,1} \cdot \left\{ -2 \cdot \eta \cdot \bar{\alpha}_i \cdot [C_{i,1} \cdot e^{\bar{\alpha}_i \cdot t_i} - C_{i,2} \cdot e^{-\bar{\alpha}_i \cdot t_i}] + (\eta^2 + \bar{\beta}_i^2) \cdot \right. \\ [C_{i,3} \cdot e^{\bar{\beta}_i \cdot t_i} + C_{i,4} \cdot e^{-\bar{\beta}_i \cdot t_i}] + \frac{2}{\eta} \cdot \bar{\beta}_i^3 \cdot [C_{i,5} \cdot e^{\bar{\beta}_i \cdot t_i} - C_{i,6} \cdot e^{-\bar{\beta}_i \cdot t_i}] & \quad (50) \\ \left. + \mu_{i+1,1} \cdot \left\{ -2 \cdot \eta \cdot \bar{\alpha}_{i+1} \cdot [C_{i+1,1} - C_{i+1,2}] + (\eta^2 + \bar{\beta}_{i+1}^2) \cdot [C_{i+1,3} + C_{i+1,4}] + \frac{2}{\eta} \cdot \bar{\beta}_{i+1}^3 \cdot [C_{i+1,5} - C_{i+1,6}] \right\} \right\} &= 0 \end{aligned}$$

$$\begin{aligned} \check{\check{\sigma}}_{zr,i} \Big|_{z_i=h_i} - \check{\check{\sigma}}_{zr,i+1} \Big|_{z_{i+1}=0} &= \mu_{i,1} \cdot \left\{ -2 \cdot \eta \cdot \bar{\alpha}_i \cdot [C_{i,1} \cdot e^{\bar{\alpha}_i \cdot t_i} - C_{i,2} \cdot e^{-\bar{\alpha}_i \cdot t_i}] + (\eta^2 + \bar{\beta}_i^2) \cdot \right. \\ & \left. [C_{i,3} \cdot e^{\bar{\beta}_i \cdot t_i} + C_{i,4} \cdot e^{-\bar{\beta}_i \cdot t_i}] + 2 \cdot \eta \cdot \bar{\beta}_i \cdot [C_{i,5} \cdot e^{\bar{\beta}_i \cdot t_i} - C_{i,6} \cdot e^{-\bar{\beta}_i \cdot t_i}] \right\} - \mu_{i+1,1} \cdot \left\{ -2 \cdot \eta \cdot \bar{\alpha}_{i+1} \cdot \right. \\ & \left. [C_{i+1,1} - C_{i+1,2}] + (\eta^2 + \bar{\beta}_{i+1}^2) \cdot [C_{i+1,3} + C_{i+1,4}] + 2 \cdot \eta \cdot \bar{\beta}_{i+1} \cdot [C_{i+1,5} - C_{i+1,6}] \right\} = 0 \end{aligned} \quad (51)$$

$$\begin{aligned} \check{\check{u}}_{r,i} \Big|_{z_i=h_i} - \check{\check{u}}_{r,i+1} \Big|_{z_{i+1}=0} &= \left\{ \bar{\alpha}_i \cdot [C_{i,1} \cdot e^{\bar{\alpha}_i \cdot t_i} - C_{i,2} \cdot e^{-\bar{\alpha}_i \cdot t_i}] + \right. \\ & \left. - \eta \cdot [C_{i,3} \cdot e^{\bar{\beta}_i \cdot t_i} + C_{i,4} \cdot e^{-\bar{\beta}_i \cdot t_i}] - \bar{\beta}_i \cdot [C_{i,5} \cdot e^{\bar{\beta}_i \cdot t_i} - C_{i,6} \cdot e^{-\bar{\beta}_i \cdot t_i}] \right\} + \\ & \left. - \left\{ \bar{\alpha}_{i+1} \cdot [C_{i+1,1} - C_{i+1,2}] - \eta \cdot [C_{i+1,3} + C_{i+1,4}] - \bar{\beta}_{i+1} \cdot [C_{i+1,5} - C_{i+1,6}] \right\} = 0 \end{aligned} \quad (52)$$

$$\begin{aligned} \check{\check{u}}_{\vartheta,i} \Big|_{z_i=h_i} - \check{\check{u}}_{\vartheta,i+1} \Big|_{z_{i+1}=0} &= \left\{ \eta \cdot [C_{i,1} \cdot e^{\bar{\alpha}_i \cdot t_i} + C_{i,2} \cdot e^{-\bar{\alpha}_i \cdot t_i}] - \bar{\beta}_i \cdot \right. \\ & \left. [C_{i,3} \cdot e^{\bar{\beta}_i \cdot t_i} - C_{i,4} \cdot e^{-\bar{\beta}_i \cdot t_i}] + \left(\eta - \frac{2}{\eta} \cdot \bar{\beta}_i^2 \right) \cdot [C_{i,5} \cdot e^{\bar{\beta}_i \cdot t_i} + C_{i,6} \cdot e^{-\bar{\beta}_i \cdot t_i}] \right\} + \\ & \left. - \left\{ \eta \cdot [C_{i+1,1} + C_{i+1,2}] - \bar{\beta}_{i+1} \cdot [C_{i+1,3} - C_{i+1,4}] + \left(\eta - \frac{2}{\eta} \cdot \bar{\beta}_{i+1}^2 \right) \cdot [C_{i+1,5} + C_{i+1,6}] \right\} = 0 \end{aligned} \quad (53)$$

$$\begin{aligned} \check{\check{u}}_{z,i} \Big|_{z_i=h_i} - \check{\check{u}}_{z,i+1} \Big|_{z_{i+1}=0} &= \\ & \left\{ -\eta \cdot [C_{i,1} \cdot e^{\bar{\alpha}_i \cdot t_i} + C_{i,2} \cdot e^{-\bar{\alpha}_i \cdot t_i}] + \bar{\beta}_i \cdot [C_{i,3} \cdot e^{\bar{\beta}_i \cdot t_i} - C_{i,4} \cdot e^{-\bar{\beta}_i \cdot t_i}] + \eta \cdot [C_{i,5} \cdot e^{\bar{\beta}_i \cdot t_i} + \right. \\ & \left. + C_{i,6} \cdot e^{-\bar{\beta}_i \cdot t_i}] \right\} - \left\{ -\eta \cdot [C_{i+1,1} + C_{i+1,2}] + \bar{\beta}_{i+1} \cdot [C_{i+1,3} - C_{i+1,4}] + \eta \cdot [C_{i+1,5} + C_{i+1,6}] \right\} = 0 \end{aligned} \quad (54)$$

where $i \in [1, 2, \dots, n, n+1 \equiv H]$ and the equation (44) has to be accounted for. The above created system of $6 \cdot n + 3$ equations can be written in the matrix form:

$$\mathbf{A} \bullet \vec{C} = \vec{b} \quad (55)$$

The matrix A in the above equation is a band matrix with the bandwidth of maximum 9 terms. \vec{C} is a properly ordered vector of integration constants $C_{i,j}$. The right side of the system is a vector, where each term except the first one equals to zero. As we have limited our interest to motion at the surface, only the first six integration constants are needed. They are obtained by Cramer's rule. The value of the determinant of the matrix A is determined by its development along the first row. According to the fact, that only first six terms of the first row are different from zero the expression of the determinant $|A|$ has the following form:

$$|A| = \sum_{j=1}^{j=6} (-1)^{j+1} \cdot a_{1,j} \cdot |A_j| \quad (56)$$

where $a_{1,j}; j \in [1, 2, \dots, 6]$ represent the first six non-zero terms of first row of matrix $[A]$ and $|A_j|; j \in [1, 2, \dots, 6]$ represent corresponding sub matrices. Due to the fact that the vector on the right side of the system equations (55) has the following form:

$$b_1 = \frac{Q(\omega)}{\pi \cdot \mu_1 \cdot k_{T1}} \quad ; \quad b_j = 0 \quad ; \quad j \in [2, 3, \dots, 6n+2], \quad (57)$$

the six constants, which determine the surface motion of the half-space, can be written as:

$$C_{1,k} = (-1)^{j+1} \cdot \frac{|A_j|}{|A|} \cdot \frac{Q(\omega)}{\pi \cdot \mu_1 \cdot k_{T1}} \quad ; \quad k \in [1, 2, 5, 6, 7, 8] \quad ; \quad (58)$$

$$j \in [1, 2, \dots, 6].$$

Introducing the equations (32), (33), (35) and (58) into equations (38) to (40) and evaluating the latter at $z = 0$ lead to the displacements on the surface of the half-space as:

$$\begin{aligned} \bar{u}_r(a,0) = & \frac{Q(\omega)}{2\pi \cdot \mu_1} \cdot \frac{\omega}{c_{T,1}} \cdot \left\{ \int_0^\infty \frac{\eta}{|A|} \cdot \left[\eta \cdot (|A_1| - |A_2|) - \sqrt{\eta^2 - 1} \cdot (|A_3| + |A_4|) + \right. \right. \\ & \left. \left. + \left[\eta - \frac{2}{\eta} \cdot (\eta^2 - 1) \right] \cdot (|A_5| - |A_6|) \right] \cdot J_0(a\eta) \cdot d\eta + \int_0^\infty \frac{\eta}{|A|} \cdot \left[-\eta \cdot (|A_1| - |A_2|) + \right. \right. \\ & \left. \left. + \sqrt{\eta^2 - 1} \cdot (|A_3| + |A_4|) + \eta \cdot (|A_5| - |A_6|) \right] \cdot J_2(a\eta) \cdot d\eta \right\} \end{aligned} \quad (59)$$

$$\begin{aligned} \bar{u}_\vartheta(a,0) = & \frac{Q(\omega)}{2\pi \cdot \mu_1} \cdot \frac{\omega}{c_{T,1}} \cdot \left\{ \int_0^\infty \frac{(-\eta)}{|A|} \cdot \left[\eta \cdot (|A_1| - |A_2|) - \sqrt{\eta^2 - 1} \cdot (|A_3| + |A_4|) + \right. \right. \\ & \left. \left. + \left[\eta - \frac{2}{\eta} \cdot (\eta^2 - 1) \right] \cdot (|A_5| - |A_6|) \right] \cdot J_0(a\eta) \cdot d\eta + \int_0^\infty \frac{\eta}{|A|} \cdot \left[-\eta \cdot (|A_1| - |A_2|) + \right. \right. \\ & \left. \left. + \sqrt{\eta^2 - 1} \cdot (|A_3| + |A_4|) + \eta \cdot (|A_5| - |A_6|) \right] \cdot J_2(a\eta) \cdot d\eta \right\} \end{aligned} \quad (60)$$

$$\begin{aligned} \bar{u}_z(a,0) = & \frac{Q(\omega)}{\pi \cdot \mu_1} \cdot \frac{\omega}{c_{T,1}} \cdot \int_0^\infty \frac{\eta}{|A|} \cdot \left[\sqrt{\eta^2 - \gamma_1^2} \cdot (|A_1| + |A_2|) - \eta \cdot (|A_3| - |A_4|) + \right. \\ & \left. - \sqrt{\eta^2 - 1} \cdot (|A_5| + |A_6|) \right] \cdot J_1(a\eta) \cdot d\eta, \end{aligned} \quad (61)$$

where following change of variable has been introduced:

$$a = k_{T,1} \cdot r = \frac{\omega \cdot r}{c_{T,1}} \quad (62)$$

For further analysis it is worth vilit to note that in the above equations only three distinct integrals appear. They are denoted as I_1 , I_2 and I_3 and are given as:

$$\begin{aligned} I_1 = & \int_0^\infty \frac{\eta}{|A|} \cdot \left\{ \eta \cdot (|A_1| - |A_2|) - \sqrt{\eta^2 - 1} \cdot (|A_3| + |A_4|) + \left[\eta - \frac{2}{\eta} \cdot (\eta^2 - 1) \right] \cdot \right. \\ & \left. (|A_5| - |A_6|) \right\} \cdot J_0(a\eta) \cdot d\eta = \int_0^\infty B_1(\eta) \cdot J_0(a\eta) \cdot d\eta \end{aligned} \quad (63)$$

$$\begin{aligned} I_2 = & \int_0^\infty \frac{\eta}{|A|} \cdot \left[-\eta \cdot (|A_1| - |A_2|) + \sqrt{\eta^2 - 1} \cdot (|A_3| + |A_4|) + \eta \cdot (|A_5| - |A_6|) \right] \\ & \cdot J_2(a\eta) \cdot d\eta = \int_0^\infty B_2(\eta) \cdot J_2(a\eta) \cdot d\eta \end{aligned} \quad (64)$$

$$\begin{aligned} I_3 = & \int_0^\infty \frac{\eta}{|A|} \cdot \left[\sqrt{\eta^2 - \gamma_1^2} \cdot (|A_1| + |A_2|) - \eta \cdot (|A_3| - |A_4|) + \right. \\ & \left. - \sqrt{\eta^2 - 1} \cdot (|A_5| - |A_6|) \right] \cdot J_1(a\eta) \cdot d\eta = \int_0^\infty B_3(\eta) \cdot J_1(a\eta) \cdot d\eta. \end{aligned} \quad (65)$$

The newly introduced functions $B_i(\eta)$, $i = 1, 2, 3$ can be identified from the above equations. They also allow

us to write the reduced surface displacements in a more compact form. They are given as:

$$\begin{aligned} \bar{u}_r(a,0) &= \frac{Q(\omega)}{2\pi \cdot \mu_1} \cdot \frac{\omega}{c_{T,1}} \cdot (I_1 + I_2) \\ &= \frac{\bar{Q}(\omega)}{2\pi \cdot \mu_1} \cdot \frac{\omega}{c_{T,1}} \cdot \left[\int_0^\infty B_1(\eta) \cdot J_0(a\eta) \cdot d\eta + \int_0^\infty B_2(\eta) \cdot J_2(a\eta) \cdot d\eta \right] \end{aligned} \quad (66)$$

$$\begin{aligned} \bar{u}_\theta(a,0) &= \frac{Q(\omega)}{2\pi \cdot \mu_1} \cdot \frac{\omega}{c_{T,1}} \cdot (-I_1 + I_2) \\ &= \frac{\bar{Q}(\omega)}{2\pi \cdot \mu_1} \cdot \frac{\omega}{c_{T,1}} \cdot \left[-\int_0^\infty B_1(\eta) \cdot J_0(a\eta) \cdot d\eta + \int_0^\infty B_2(\eta) \cdot J_2(a\eta) \cdot d\eta \right] \end{aligned} \quad (67)$$

$$\bar{u}_z(a,0) = \frac{Q(\omega)}{\pi \cdot \mu_1} \cdot \frac{\omega}{c_{T,1}} \cdot I_3 = \frac{\bar{Q}(\omega)}{\pi \cdot \mu_1} \cdot \frac{\omega}{c_{T,1}} \cdot \int_0^\infty B_3(\eta) \cdot J_1(a\eta) \cdot d\eta. \quad (68)$$

3 EVALUATION OF THE INVERSION INTEGRALS

As it is known from the literature [27] and it was already demonstrated in the previous paper by the authors [19] the leading term of singularity depends on the local conditions only. Due to this fact the singularity at the

surface of the layered half-space can be determined by considering the homogeneous half-space with the material properties of the uppermost layer, what considerably simplifies the analysis. The integrals I_i , $i=1,2,3$ equations (63) to (65) are first reduced to the case of a homogeneous half-space and consecutively their limits are evaluated. This yield:

$$\begin{aligned} \frac{\omega}{2c_{T,1}} I_{s,1} &= \frac{\omega}{2c_{T,1}} \cdot \lim_{a \rightarrow 0} \int_0^\infty \left[\frac{\eta}{\sqrt{\eta^2 - 1}} - \frac{\eta \cdot \sqrt{\eta^2 - 1}}{|F_H(\eta)|} \right] \cdot J_0(a\eta) \cdot d\eta \\ &= \frac{\omega}{2c_{T,1}} \cdot \int_0^\infty \lim_{\eta \rightarrow \infty} \left[\frac{\eta}{\sqrt{\eta^2 - 1}} - \frac{\eta \cdot \sqrt{\eta^2 - 1}}{|F_H(\eta)|} \right] \cdot J_0(a\eta) \cdot d\eta \\ &= \frac{\omega}{2c_{T,1}} \cdot \frac{3 - 2\gamma^2}{2 - 2\gamma^2} \cdot \int_0^\infty J_0(a\eta) \cdot d\eta = \frac{2 - \nu_1}{2r} \end{aligned} \quad (69)$$

and in an analogous way:

$$\frac{\omega}{2c_{T,1}} I_{s,2} = \frac{\omega}{2c_{T,1}} \cdot \lim_{a \rightarrow 0} \int_0^\infty \left[\frac{\eta}{\sqrt{\eta^2 - 1}} + \frac{\eta \cdot \sqrt{\eta^2 - 1}}{|F_H(\eta)|} \right] \cdot J_0(a\eta) \cdot d\eta = \frac{\nu_1}{2r} \quad (70)$$

where:

$$|F_H(\eta)| = (2 \cdot \eta^2 - 1)^2 - 4 \cdot \eta^2 \cdot \sqrt{\eta^2 - 1} \cdot \sqrt{\eta^2 - \gamma^2}. \quad (71)$$

The limit of the integral I_3 as $a \rightarrow 0$ is zero and therefore it remains regular for all values of a . The singularity

given by equations (69) and (70) are now subtracted from integrals I_1 and I_2 respectively and taken under the integral sign. This yields:

$$\begin{aligned} \bar{I}_1 &= I_1 - I_{s,1} = \int_0^\infty \frac{\eta}{|A|} \cdot \left\{ \eta \cdot (|A_1| - |A_2|) - \sqrt{\eta^2 - 1} \cdot (|A_3| + |A_4|) + \right. \\ &\quad \left. + \left[\eta - \frac{2}{\eta} \cdot (\eta^2 - 1) \right] \cdot (|A_5| - |A_6|) - (2 - \nu_1) \right\} \cdot J_0(a\eta) \cdot d\eta \quad (72) \\ &= \int_0^\infty \bar{B}_1(\eta) \cdot J_0(a\eta) \cdot d\eta \end{aligned}$$

$$\begin{aligned} \bar{I}_2 &= I_2 - I_{s,2} = \int_0^\infty \frac{\eta}{|A|} \cdot \left\{ -\eta \cdot (|A_1| - |A_2|) + \sqrt{\eta^2 - 1} \cdot (|A_3| + |A_4|) + \right. \\ &\quad \left. + \eta \cdot (|A_5| - |A_6|) - \nu_1 \right\} \cdot J_2(a\eta) \cdot d\eta \quad (73) \\ &= \int_0^\infty \bar{B}_2(\eta) \cdot J_2(a\eta) \cdot d\eta. \end{aligned}$$

The horizontal displacements components are now given by:

$$\begin{aligned} \bar{u}_r(a,0) &= \frac{Q(\omega)}{2\pi \cdot \mu_1} \cdot \left[\frac{1}{r} + \frac{\omega}{c_{T,1}} \cdot (\bar{I}_1 + \bar{I}_2) \right] \\ &= \frac{Q(\omega)}{2\pi \cdot \mu_1} \cdot \left[\frac{1}{r} + \frac{\omega}{c_{T,1}} \cdot \left[\int_0^\infty \bar{B}_1(\eta) \cdot J_0(a\eta) \cdot d\eta + \int_0^\infty \bar{B}_2(\eta) \cdot J_2(a\eta) \cdot d\eta \right] \right] \quad (74) \end{aligned}$$

$$\begin{aligned} \bar{u}_\theta(a,0) &= \frac{\bar{Q}(\omega)}{2\pi \cdot \mu_1} \cdot \left[-\frac{1-\nu}{r} + \frac{\omega}{c_{T,1}} \cdot (-\bar{I}_1 + \bar{I}_2) \right] \\ &= \frac{\bar{Q}(\omega)}{2\pi \cdot \mu_1} \cdot \left[-\frac{1-\nu}{r} + \frac{\omega}{c_{T,1}} \cdot \left[-\int_0^\infty \bar{B}_1(\eta) \cdot J_0(a\eta) \cdot d\eta + \int_0^\infty \bar{B}_2(\eta) \cdot J_2(a\eta) \cdot d\eta \right] \right]. \quad (75) \end{aligned}$$

We note that the singular terms, which appear in the horizontal displacement components, are given explicitly. The values of the integrals \bar{I}_1 and \bar{I}_2 are bounded for all values of the parameter a or r respectively. And what is also important for a numerical evaluation and of course for our later considerations $\bar{B}_1(\eta)$, $\bar{B}_2(\eta)$ and $B_3(\eta)$ tend to zero as $\eta \rightarrow \infty$.

3.1 EXTENDING THE RANGE OF INTEGRATION

To transform the integrals \bar{I}_i , $i = 1, 2$ and I_3 into a form permitting their evaluation by contour integration in a complex η -plane we must make their integrands single valued and extend the range of integration from $-\infty$ to

∞ . Thus we note that the functions $\bar{B}_1(\eta)$, $\bar{B}_2(\eta)$ and $B_3(\eta)$ are not single-valued due to the terms $\bar{\alpha}_i$ and $\bar{\beta}_i$ appearing in them. They are made single valued by introducing the branch cuts in the complex η -plane. In the selection of a suitable branch cut we are however limited by the following requirements: imposed radiation conditions, which require that the real parts of $\bar{\alpha}_i(\eta)$ and $\bar{\beta}_i(\eta)$ are positive on the positive real η -axis; that it does not intersect the big semi-circle in the upper η -half-plane and by the demand that $\bar{\alpha}_i(\eta)$ and $\bar{\beta}_i(\eta)$ are odd functions of η on the real η -axis. The latter is needed to extend the range of integration from semi-infinite to infinite. The branch-cut fulfilling the above stated requirements is shown in Fig. 4.

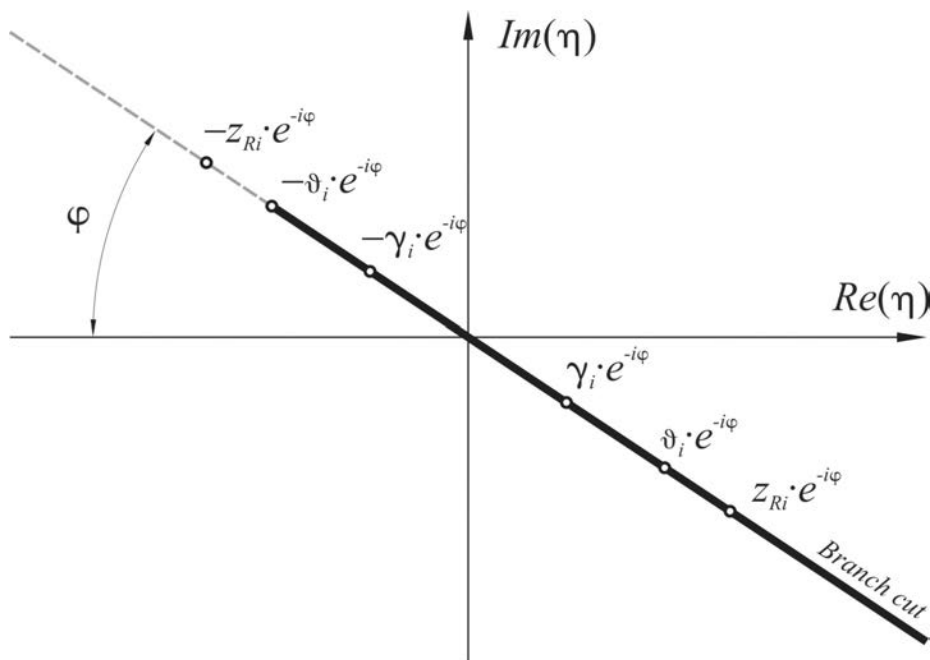


Figure 4. Branch points of expressions $\bar{\alpha}_i$ and $\bar{\beta}_i$ with introduced branch cut and the corresponding Rayleigh pole. For greater clarity of the figure some material damping has been assumed and expressed by complex shear module $\mu_i = \mu_{0i} \cdot e^{i\varphi}$.

We realize that the chosen branch-cut indeed makes $\bar{\alpha}_i(\eta)$ and $\bar{\beta}_i(\eta)$ odd functions of η on the real η -axis and does not intersect the big semi-circle in the upper η -half-plane. We further note that all terms of matrix A , equation (55), except the exponential functions:

$$\begin{aligned}
 p_i^\pm(\eta) &= e^{\pm \bar{\alpha}_i t_i} = e^{\pm \sqrt{\eta^2 - \gamma_i^2} t_i} \quad \text{and} \\
 q_i^\pm(\eta) &= e^{\pm \bar{\beta}_i t_i} = e^{\pm \sqrt{\eta^2 - \vartheta_i^2} t_i} \quad (76)
 \end{aligned}$$

which are neither odd nor even. To make the terms in matrix A determined with respect to evenness or oddness respectively we replace them by their analytic continuations, which do not change their values on positive η -axis and are even functions on the real η -axis. As functions satisfying the stated requirements we have chosen:

$$\begin{aligned}
 \tilde{p}_i^\pm(\eta) &= e^{\pm \frac{\eta}{|\eta|} \sqrt{\eta^2 - \gamma_i^2} t_i} = e^{\pm \bar{\alpha}_i t_i} \quad \text{and} \\
 \tilde{q}_i^\pm(\eta) &= e^{\pm \frac{\eta}{|\eta|} \sqrt{\eta^2 - \vartheta_i^2} t_i} = e^{\pm \bar{\beta}_i t_i} \quad (77)
 \end{aligned}$$

The replacement of the functions $p_i^\pm(\eta)$ and $q_i^\pm(\eta)$ in equations (49)-(54) through $\tilde{p}_i^\pm(\eta)$ and $\tilde{q}_i^\pm(\eta)$ leads

to the matrix \tilde{A} , which has on the integration path of inverse Hankel transform exactly the same values as the original matrix A . The terms of matrix \tilde{A} have interesting and for further analysis very useful properties. It can be seen from equations (46) to (48) that all the terms in the first three rows of matrix \tilde{A} are even functions of η on the real η -axis. The further rows of matrix \tilde{A} are coming from continuity conditions on interfaces between layers, six rows for each interface. From equations (49) to (54) it is easy to recognize that the first three of these six rows contain only terms, which are even functions of η , and the next three only terms, which are odd functions of η on the real η -axis. Matrix \tilde{A} therefore has $3 \cdot (n+1)$ rows, where all the terms are even, and $3 \cdot n$ rows, where all the terms are odd and n is the number of layers. This implies that all the determinants $|\tilde{A}|$ and $|\tilde{A}_i|$, $i \in [1, 2, \dots, 6]$ are in the case of odd number of layers n odd functions and on the other hand in the case of even number of layers n are even functions on the real η -axis. We now derive functions $\tilde{B}_i(\eta)$ exactly the same way as we have derived functions $B_i(\eta)$ only that we make use of determinants $|\tilde{A}|$ and $|\tilde{A}_i|$, $i \in [1, 2, \dots, 6]$, instead of the determinants $|A|$ and $|A_i|$, $i \in [1, 2, \dots, 6]$. This yields:

$$\begin{aligned} \tilde{B}_1(\eta) = & \frac{\eta}{|\tilde{A}_1|} \cdot \left[\eta \cdot (|\tilde{A}_1| - |\tilde{A}_2|) - \sqrt{\eta^2 - 1} \cdot (|\tilde{A}_3| + |\tilde{A}_4|) + \right. \\ & \left. + \left(\eta - \frac{2}{\eta} \cdot (\eta^2 - 1) \right) \cdot (|\tilde{A}_5| - |\tilde{A}_6|) \right] - (2 - \nu_1) \end{aligned} \quad (78)$$

$$\begin{aligned} \tilde{B}_2(\eta) = & \frac{\eta}{|\tilde{A}_1|} \cdot \left[-\eta \cdot (|\tilde{A}_1| - |\tilde{A}_2|) + \sqrt{\eta^2 - 1} \cdot (|\tilde{A}_3| + |\tilde{A}_4|) + \right. \\ & \left. + \eta \cdot (|\tilde{A}_5| - |\tilde{A}_6|) \right] - \nu_1 \end{aligned} \quad (79) \text{ and}$$

$$\tilde{B}_3(\eta) = \frac{\eta}{|\tilde{A}_1|} \cdot \left[\sqrt{\eta^2 - \gamma_1^2} \cdot (|\tilde{A}_1| + |\tilde{A}_2|) - \eta \cdot (|\tilde{A}_3| - |\tilde{A}_4|) - \sqrt{\eta^2 - 1} \cdot (|\tilde{A}_5| + |\tilde{A}_6|) \right]. \quad (80)$$

where all the $\tilde{B}_i(\eta)$, $i \in [1, 2, 3]$ are even functions of η on the real η -axis and $\tilde{B}_i(\eta) = \bar{B}_i(\eta)$, $i \in [1, 2]$ and $\tilde{B}_3(\eta) = B_i(\eta)$ on the real, positive η -axis. Taking into account these equalities, the equations (72), (73) and (65) can be written as:

$$\bar{I}_1 = \int_0^\infty \bar{B}_1(\eta) \cdot J_0(a\eta) \cdot d\eta = \int_0^\infty \tilde{B}_1(\eta) \cdot J_0(a\eta) \cdot d\eta = \tilde{I}_1 \quad (81)$$

$$\bar{I}_2 = \int_0^\infty \bar{B}_2(\eta) \cdot J_2(a\eta) \cdot d\eta = \int_0^\infty \tilde{B}_2(\eta) \cdot J_2(a\eta) \cdot d\eta = \tilde{I}_2 \quad (82)$$

and

$$I_3 = \int_0^\infty B_3(\eta) \cdot J_1(a\eta) \cdot d\eta = \int_0^\infty \tilde{B}_3(\eta) \cdot J_1(a\eta) \cdot d\eta = \tilde{I}_3. \quad (83)$$

At this point we make use of integral representations of Bessel functions known from the literature e.g. Gradshteyn et al. [28]:

$$J_i(a\eta) = h_i(a\eta) + h_i(-a\eta); \quad i = 1, 2, 3 \quad (84)$$

where:

$$h_0(a\eta) = \frac{1}{2\pi} \int_0^\pi e^{i a \eta \sin \vartheta} d\vartheta \quad (85)$$

$$h_1(a\eta) = \frac{1}{2} H_1^1(a\eta) \quad (86)$$

$$h_2(a\eta) = \frac{1}{2\pi} \int_0^\pi e^{i(a\eta \sin \vartheta - 2\vartheta)} d\vartheta \quad (87)$$

and $H_1^1(a\eta)$ is the Hankel's function of the first order and the first kind. Making use of the relationship (84) equation (81) yields:

$$\begin{aligned} \bar{I}_1 = \tilde{I}_1 = & \int_0^\infty \tilde{B}_1(\eta) \cdot J_0(a\eta) \cdot d\eta = \int_0^\infty \tilde{B}_1(\eta) \cdot h_0(a\eta) \cdot d\eta + \int_0^\infty \tilde{B}_1(\eta) \cdot h_0(-a\eta) \cdot d\eta \\ = & \int_0^\infty \tilde{B}_1(\eta) \cdot h_0(a\eta) \cdot d\eta + \int_0^\infty \tilde{B}_1(-\eta) \cdot h_0(a\eta) \cdot (-d\eta) = \int_{-\infty}^\infty \tilde{B}_1(\eta) \cdot h_0(a\eta) \cdot d\eta = \check{I}_1. \end{aligned} \quad (88)$$

Where we have made use of the change of variables $\eta \rightarrow -\eta$ and the symmetry of the function $\tilde{B}_1(\eta)$. In a very analogous fashion we obtain for the other two pertinent integrals given by equations (82) and (83) following expressions:

$$\bar{I}_2 = \check{I}_2 = \int_0^\infty \tilde{B}_2(\eta) \cdot J_2(a\eta) \cdot d\eta = \int_{-\infty}^\infty \tilde{B}_2(\eta) \cdot h_2(a\eta) \cdot d\eta = \check{I}_2 \quad (89)$$

$$I_3 = \int_0^\infty B_3(\eta) \cdot J_1(a\eta) \cdot d\eta = \int_{-\infty}^\infty \tilde{B}_3(\eta) \cdot h_1(a\eta) \cdot d\eta = \check{I}_3. \quad (90)$$

The equations (88) to (90) clearly show that we have successfully replaced the original inverse Hankel transform integrals with the range of integration from 0 to $+\infty$ with newly defined integrals having the range of integration from $-\infty$ to $+\infty$. The integrals \check{I}_i , $i = 1, 2, 3$ can be evaluated by contour integration in the complex η -plane as it will be shown in the next paragraph.

3.2 EVALUATION OF INTEGRALS BY CONTOUR INTEGRATION

Integrals \check{I}_1 , \check{I}_2 and \check{I}_3 , are finally in the form permitting their evaluation by the contour integration in the complex η -plane. The most suitable contour is shown in Fig. 5. By the residue theorem it can be written:

$$\check{I}_{i+} + \check{I}_{iR} + \check{I}_{i-} + \check{I}_{ib1} + \check{I}_{iR} + \check{I}_{ib2} = 2\pi i \sum \text{res}_i; \quad i = 1, 2, 3. \quad (91)$$

It can be easily shown that the value of the integral along the big semi-circle in the upper η -half plane is identi-

cally zero. This is due to the behaviour of integrands, which are dominated by $h_i(a\eta)$ functions. On the big

semi-circle η can be given as $\eta = R \cdot e^{i\varphi}$, where φ takes the values from 0 to π . Equations (85) and (87) yield:

$$\begin{aligned} \lim_{\substack{|\eta| \rightarrow \infty \\ \text{Im}(\eta) > 0}} h_0(a\eta) &= \lim_{R \rightarrow \infty} \frac{1}{\pi} \int_0^\pi \exp[iR(\cos\varphi + i\sin\varphi)\sin\vartheta] d\vartheta = \\ &= \frac{1}{\pi} \lim_{R \rightarrow \infty} \int_0^\pi \exp(-R\sin\varphi + iR\cos\varphi)\sin\vartheta d\vartheta \rightarrow 0 \end{aligned} \tag{92}$$

$$\begin{aligned} \lim_{\substack{|\eta| \rightarrow \infty \\ \text{Im}(\eta) > 0}} h_2(z) &= \lim_{R \rightarrow \infty} \frac{1}{\pi} \int_0^\pi \exp[iR(\cos\varphi + i\sin\varphi)\sin\vartheta - 2i\vartheta] d\vartheta = \\ &= \frac{1}{\pi} \lim_{R \rightarrow \infty} \int_0^\pi \exp[(-R\sin\varphi + iR\cos\varphi)\sin\vartheta - 2i\vartheta] d\vartheta \rightarrow 0 \end{aligned} \tag{93}$$

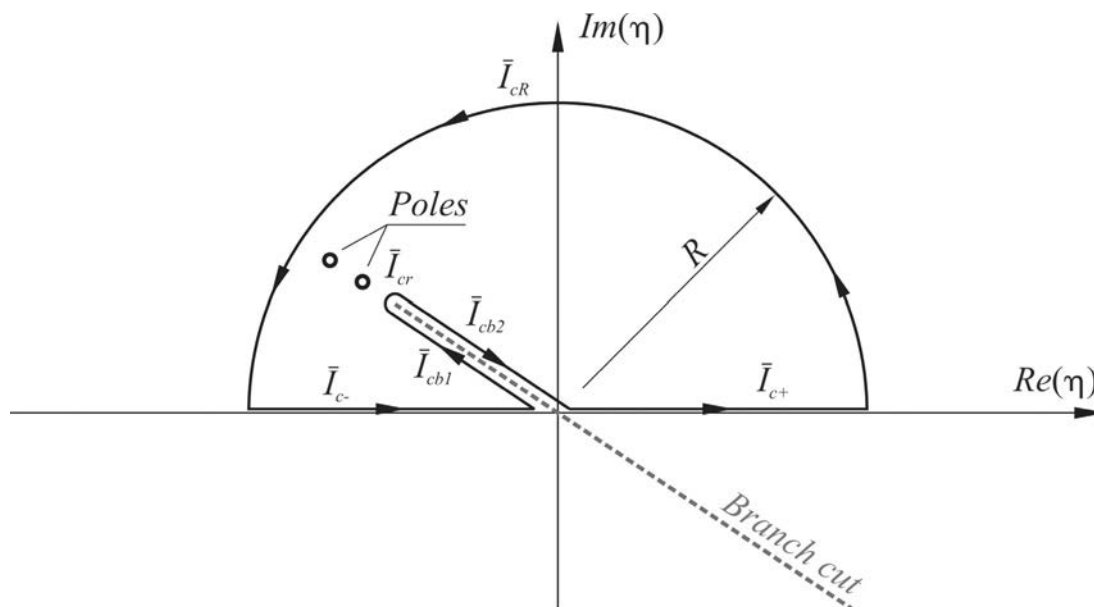


Figure 5. Integration path for the evaluation of integrals \check{I}_1 , \check{I}_2 and \check{I}_3 . Some material damping is assumed to make the picture clearer.

And the same behavior for $h_1(a\eta) = H_1^{(1)}(a\eta)$, namely that $\lim_{R \rightarrow \infty} H_1^{(1)}(R \cdot e^{i\varphi}) \rightarrow 0$ for $0 \leq \varphi \leq \pi$ is well documented in the literature [29]. Therefore it can be concluded:

$$\check{I}_{iR} = 0; \quad i = 1, 2, 3. \tag{94}$$

Taking in account the above equation the equation (91) can be rewritten as:

$$\check{I}_i = \check{I}_{i+} + \check{I}_{i-} = 2\pi i \sum \text{res}_i - \check{I}_{ib1} - \check{I}_{ir} - \check{I}_{ib2}; \quad i = 1, 2, 3. \tag{95}$$

It is clear from Fig. 5 that all three integrals appearing in the right hand term of the above equation have finite integration path. Therefore by the equation (95) our

fundamental goal has been achieved. It can be further noted that if the integrals \check{I}_{ib1} and \check{I}_{ib2} are led along one and the other side of the branch cut and the value of the integral \check{I}_{ir} is equal zero. For the numerical calculation it is advantageous to express the integrals \check{I}_{ib1} and \check{I}_{ib2} through a sum of integrals of even shorter integration range stretching from one singularity on the branch cut to the other. These singularities are either branch points of functions $\bar{\alpha}_i$ and $\bar{\beta}_i$ defined through the equation (45) or the poles defined by the zeros of the determinant $|A|$, which lie on the branch cut. Introducing the equation (95) and considering the equations (88)-(90) into equations (74), (75) and (68) yields the surface displacements as:

$$\bar{u}_r(a,0) = \frac{Q(\omega)}{2\pi \cdot \mu_1} \cdot \left\{ \frac{1}{r} + \frac{\omega}{c_{T,1}} \cdot \left[2\pi i \cdot \sum (res_1 + res_2) - \check{I}_{1b1} - \check{I}_{2b1} - \check{I}_{1b2} - \check{I}_{2b2} \right] \right\} \quad (96)$$

$$\bar{u}_\theta(a,0) = \frac{Q(\omega)}{2\pi \cdot \mu_1} \cdot \left\{ \frac{1-\nu}{r} + \frac{\omega}{c_{T,1}} \cdot \left[2\pi i \cdot \sum (-res_1 + res_2) + \check{I}_{1b1} - \check{I}_{2b1} + \check{I}_{1b2} - \check{I}_{2b2} \right] \right\} \quad (97)$$

$$\bar{u}_z(a,0) = \frac{Q(\omega)}{2\pi \cdot \mu_1} \cdot \frac{\omega}{c_{T,1}} \cdot \left(2\pi i \sum res_3 - \check{I}_{3b1} - \check{I}_{3b2} \right) \quad (98)$$

The above three equations are the final result of our analysis. In them the surface displacements of a layered half-space due to a tangential point load are given by a singular term, in the components, which become singular as $r \rightarrow 0$, a sum of the residues and a sum of integrals with the finite integration path. The latter ones can be evaluated numerically with any desired accuracy. We can further note that the residues represent the surface waves and the integrals are due to body waves.

4 NUMERICAL EXAMPLE

As an illustrative example a one-layer half-space with the same geometrical and material characteristics as the one considered by Štrukelj et al. [19] has been chosen. It is shown in Fig. 1 with $n = 1$. On its surface a horizontal, harmonic point-load is applied. The material properties of this half-space are as follows: ratio of material densities in the underlying half-space and the layer is $\rho_H/\rho_1 = 1.5$, the ratio of shear modules $\mu_H/\mu_1 = 2.0$, the Poisson's ratio for the layer is $\nu_1 = 1/3$ and the

Poisson's ratio for underlying half-space is $\nu_H = 1/4$. The materials in the layer and in the underlying half-space are assumed to have no material damping. The ratio of the layer thickness h_1 and the wave length of shear waves in the layer λ_1 is taken to be $h_1/\lambda_1 = 2.0$.

As it can be seen from equations (96) to (98), the displacement components are expressed as sums of several terms. It is worthwhile to note that in the both horizontal displacements components the same terms appear with exception of the singular term. In the vertical displacement, however, completely different terms are forthcoming. The numerical effort can be, therefore, considerably reduced by computing first each of these terms separately and later combine them into displacement components as given by equations (96) to (98). In the Fig. 6 and 7 as an example three such characteristic terms are given.

Our choice of the geometrical and material properties of the half-space is based on the fact that it is nearly impossible to obtain the data in the pertinent literature, with which our results could be compared to prove their valid-

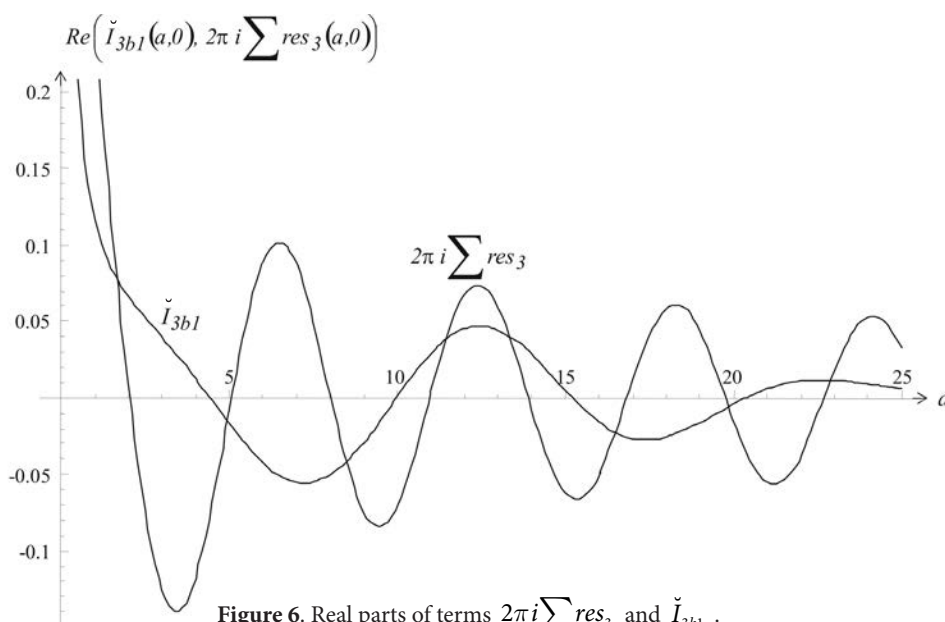


Figure 6. Real parts of terms $2\pi i \sum res_3$ and \check{I}_{3b1} .

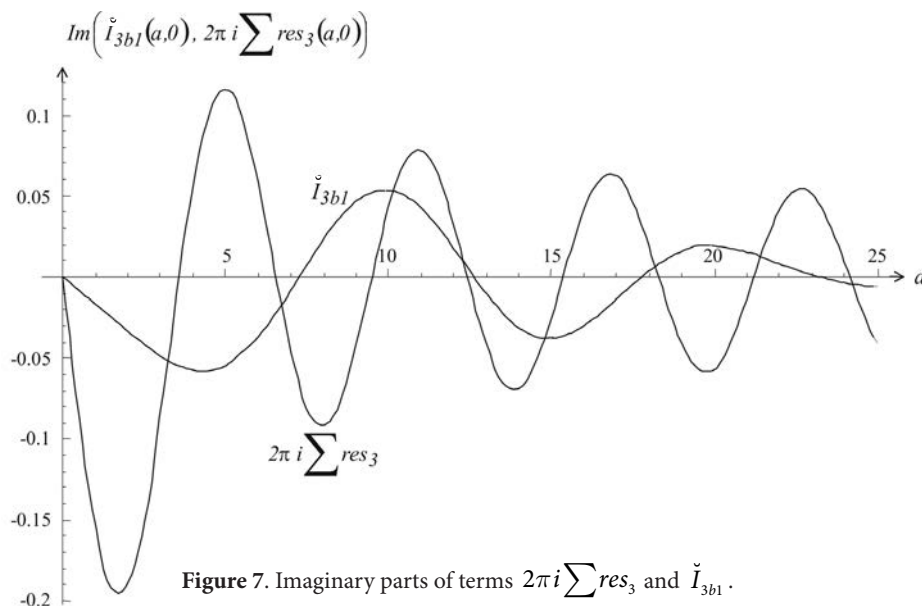


Figure 7. Imaginary parts of terms $2\pi i \sum res_3$ and \check{I}_{3b1} .

ity and accuracy. Therefore we have decided to make use of the principle of reciprocity in elastodynamics, which is well described in the literature e.g. by Achenbach [30]. It can be concluded from this principle, that the vertical displacements along the ray $\vartheta = 0$ in a half-space loaded with a horizontal, harmonic, unit point-load are equal to the radial displacements in an identical half-space loaded with a vertical, harmonic and unit point-load. Therefore we can state that for our above described choice of the layered half-space the displacement component $\bar{u}_z(a,0)$, as given by equation (98), should equal the radial component of the surface displacements presented by Štrukelj et al. [19]. It is however worth vile to note that this equivalence can not be seen from the two expressions before their numerical evaluation. The integrals in equation (98)

have integrands, which are based on the determinant and sub-determinants of a 9x9 matrix A . The corresponding integrals are in the case of the vertically loaded half-space based on a 6x6 matrix.

The real and imaginary parts of both displacement functions are shown in Fig. 8 and 9. It can be seen from both figures that they are in an excellent agreement with the results presented by Štrukelj et al [19].

The results of the evaluation of the radial displacement component $\bar{u}_r(a,0)$ are shown in the Fig. 10 and 11. In exactly the same way the circumferential displacement component $\bar{u}_\vartheta(a,0)$ can be evaluated through a different combination of terms appearing in $\bar{u}_r(a,0)$. The results of this evaluation will not be presented in this paper.

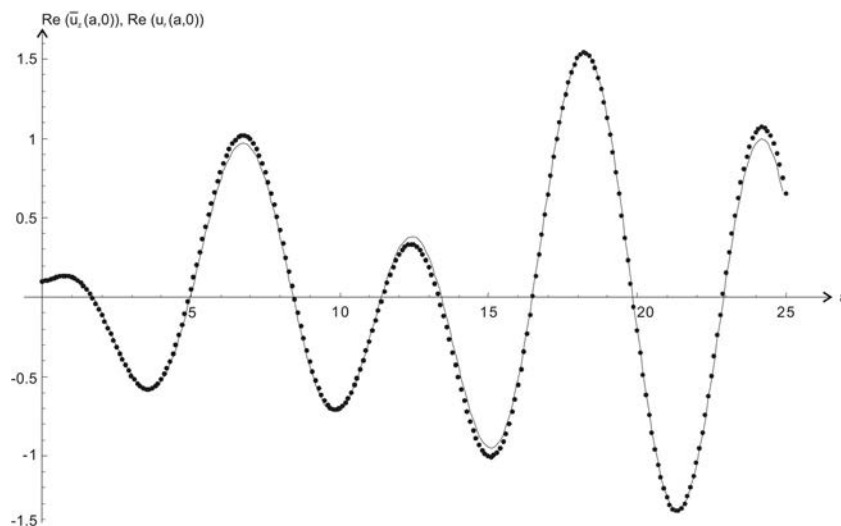


Figure 8. The real part of the displacement function $\bar{u}_z(a,0)$ given by the dotted line and the real part of the function $u_r(a,0)$ presented through the solid line.

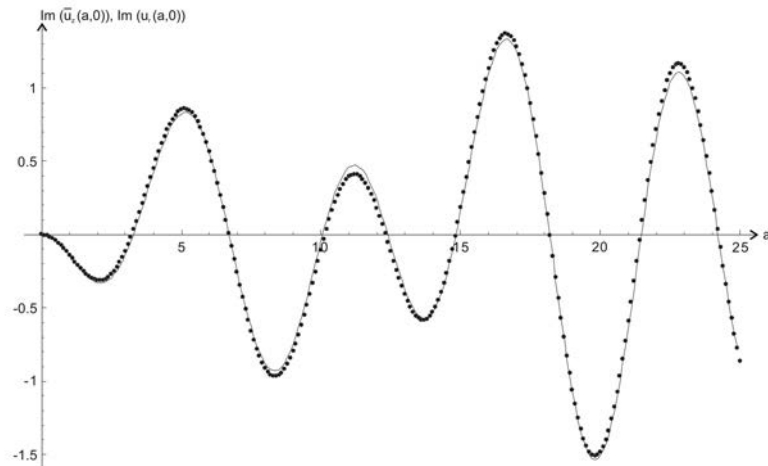


Figure 9. The imaginary part of the displacement function $\bar{u}_z(a,0)$ given by the dotted line and the real part of the function $u_r(a,0)$ presented through the solid line.

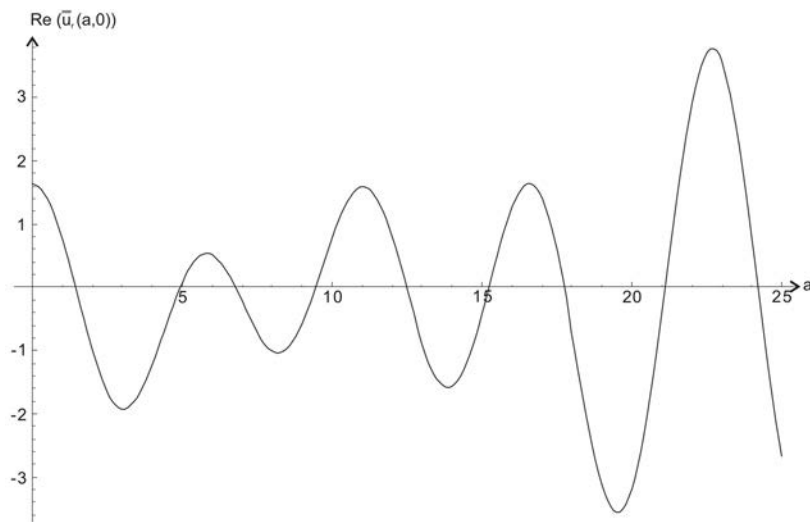


Figure 10. The real part of the displacement function $\bar{u}_r(a,0)$.

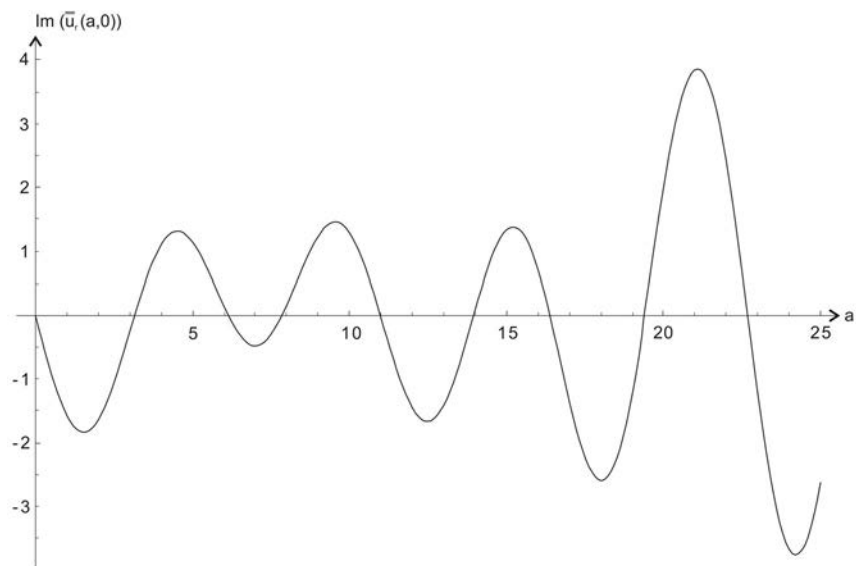


Figure 11. The imaginary part of the displacement function $\bar{u}_r(a,0)$.

5 CONCLUSION

The displacement components on the surface of a horizontally layered half-space due to a tangential point-load were expressed through a combination of three distinct Hankel's inverse integrals and trigonometric functions with the circumferential coordinate as argument. For the evaluation of these Hankel's integrals a novel three step procedure is employed. In the first step the singularity at the generic point from the integrals, where it exists is extracted and the resulting new integrals are made regular. In the second step we replaced the new integrands functions with their suitable analytic continuations, by which we were able to extend the integration range of Hankel's integrals to $-\infty$ to $+\infty$. By this extension of the integration range we were in the last step permitted to evaluate them by contour integration.

Through these three steps we were able to transform the Hankel's integrals into sum of three terms. The first one contains the singularity in the form C/r , the second one is given by a sum of the residues of the integrand and finally the third term consists of finite number of integrals along the suitable chosen branch-cut. The latter ones regular and finite in their integration range can be easily evaluated numerically.

The results presented in this paper together with the our previous results, Štrukelj et al. [19], constitute, what we believe, a robust and numerically efficient method to evaluate the displacements on the surface of the horizontally layered half-space due to a point force of any direction. The method of evaluation presented in this paper provides us with exact and closed form expressions for the singularities of displacement field, what makes our results very suitable to be used in soil-structure interaction problems.

We are convinced that an even more efficient integration line around the branch cut from the one used in this paper can be developed. Before we could come up with a definite recommendation concerning the integration path more numerical research is needed. It is however believed that this problem is beyond the scope of this paper, where we succeeded to demonstrate that the Green's function for a layered half-space can be expressed as a combination of terms, which can be easily, especially in comparison with original Hankel's inversion integrals, and accurately evaluated.

REFERENCES

- [1] Premrov M, Špacapan I. (2004). Solving exterior problems of wave propagation based on an iterative variation of local DtN operators. *Appl. Math. Model.*, 28, 3, 291-305.
- [2] Kelvin (Lord) (1843). Displacements due to a point load in an indefinitely extended solid. Citation no. 66 in Love's Treatise on the Mathematical Theory of Elasticity, 4th ed. Dover Press, New York.
- [3] Boussinesq J. (1878-1885). Citation no. 67 in Love's Treatise on the Mathematical Theory of Elasticity, 4th ed. Dover Press, New York.
- [4] Cerruti V. (1882). Citation no. 68 in Love's Treatise on the Mathematical Theory of Elasticity, 4th ed. Dover Press, New York.
- [5] Lamb H. (1904). On the propagation of tremors over the surface of an elastic solid. *Phil. Trans. Royal Soc. Lond.*; A 203, 1-42.
- [6] Midlin RD. (1936). Force at a point in the interior of a semi-infinite solid. *J. Appl. Phys.*, 7, 195-202.
- [7] Ewing MW, Jardetzky WS, Press F. (1957). *Elastic waves in layered media*. McGraw-Hill Book Company New York.
- [8] Apsel J, Luco J.E. (1983). On the Green's functions for a layered half-space, Part I. *Bull. Seismol. Soc. Am.*, 73(4), 909-929.
- [9] Apsel J, Luco J.E. (1983). On the Green's functions for a layered half-space, Part II. *Bull. Seismol. Soc. Am.*, 73(4), 931-951.
- [10] Kausel E, Peek R. (1984). Dynamic loads in the interior of a layered stratum, An explicit solution. *Bull. Seismol. Soc. Am.*, 74, 1459-1481.
- [11] Gaitanaros AP, Karabalis DL. (1988). Dynamic analysis of 3D flexible embedded foundations by a frequency domain BEM-FEM. *Earthquake Engng. Struct. Dyn.*, 16, 653-674.
- [12] Triantafyllidis T. (1991). 3D time domain BEM using half-space Green's functions. *Engng. Anal. Bound. Elem.*, 8 (3), 115-124.
- [13] Auersch L. (1994). Wave propagation in layered soils, Theoretical solution in wave number domain and experimental results of hammer and railway traffic excitation. *J. Sound Vibration*, 173(2), 233-264.
- [14] Aubry D., Clouteau D. (1991). A regularized boundary element method for stratified media. In: Cohen G., Halpen L., Joly P., editors: *Proceedings of the First International Conference on Mathematical and Numerical Aspects of Wave Propagation Phenomena*, 660-668.
- [15] Vostroukhov A.V., Verichev S.N. (2004). Kok A.W.M., Esveld C., Steady-state response of a stratified half-space subjected to a horizontal arbitrary

- buried uniform load applied at a circular area. *Soil Dyna. Earth. Engng.*, 24, 449-459.
- [16] Jin B., Lia H. (1999). Exact solution for horizontal displacement at center of surface of an elastic half-space under horizontal impulsive punch loading. *Soil Dyna. Earth. Engng.*, 18, 495-498.
- [17] Bringham E.O. (1974). *The Fast Fourier Transform*. Prentice – Hall, New York.
- [18] Kobayashi T, Sasaki F. (1991). Evaluation of Green's function on semi-infinite elastic medium. *KICT Report No. 86*, Kajima Technical Research Institute, Kajima Corporation.
- [19] Štrukelj A., Pliberšek T., Umek A. (2006). Evaluation of Green's function for vertical point load excitation applied to the surface of a layered semi-infinite elastic medium. *Arch. Appl. Mech.*, 76, 465-479.
- [20] Pliberšek T., Štrukelj A., Umek A. (2005). Green's function for an elastic layer loaded harmonically on its surface. *Acta Geotechnica Slovenica*, 2, 4-21.
- [21] Žlender B., Lenart S. (2005). Cyclic liquefaction potential of lacustrine carbonate silt from Julian alps. *Acta Geotechnica Slovenica*, 1, 22-31.
- [22] Žlender B., Trauner L. (2007). The dynamic properties of the snail soil from the Ljubljana marsh. *Acta Geotechnica Slovenica*, 2, 48-61.
- [23] Kobayashi T. (1981). Evaluation of response to point load excitation on semi-infinite elastic medium (in Japanese). *Tran. Archi. Institute.*, Japan, 302, 29-35.
- [24] Achenbach J.D. (1973). *Wave propagation in elastic solids*. North-Holland, Amsterdam, London.
- [25] Miklowitz J. (1980). *The theory of elastic waves and waveguides*. North-Holland, Amsterdam, New York, Oxford.
- [26] Sneddon I.H. (1972). *The use of integral transforms*. McGraw-Hill Book Company, New York, Toronto.
- [27] Pao Y.H., Mow C.C. (1971). *Diffraction of elastic waves and dynamic stress concentrations*. Crane Russak, New York.
- [28] Gradshteyn I.S., Ryzhik, I.M. (1994). *Table of Integrals, Series, and Products*, Academic Press Limited, London.
- [29] Abramowitz M., Stegun I.A. (1972). *Handbook of mathematical functions*. New York, Dover publications.
- [30] Achenbach J.D. (2003). *Reciprocity in Elastodynamics*, Cambridge University Press, Cambridge.

NAVODILA AVTORJEM

Članki so objavljeni v angleškem jeziku s prevodom izvlečka v slovenski jezik.

VSEBINA ČLANKA

Članek naj bo napisan v naslednji obliki:

- Naslov, ki primerno opisuje vsebino članka in ne presega 80 znakov.
- Izvleček, ki naj bo skrajšana oblika članka in naj ne presega 250 besed. Izvleček mora vsebovati osnove, jedro in cilje raziskave, uporabljeno metodologijo dela, povzetek izidov in osnovne sklepe.
- Uvod, v katerem naj bo pregled novejšega stanja in zadostne informacije za razumevanje ter pregled izidov dela, predstavljenih v članku.
- Teorija.
- Eksperimentalni del, ki naj vsebuje podatke o postavitvi preiskusa in metode, uporabljene pri pridobitvi izidov.
- Izidi, ki naj bodo jasno prikazani, po potrebi v obliki slik in preglednic.
- Razprava, v kateri naj bodo prikazane povezave in posplošitve, uporabljene za pridobitev izidov. Prikazana naj bo tudi pomembnost izidov in primerjava s poprej objavljenimi deli.
- Sklepi, v katerih naj bo prikazan en ali več sklepov, ki izhajajo iz izidov in razprave.
- Literatura, ki mora biti v besedilu oštevilčena zaporedno in označena z oglatimi oklepaji [1] ter na koncu članka zbrana v seznamu literature.

OBLIKA ČLANKA

Besedilo naj bo pisano na listih formata A4, z dvojnimi presledki med vrstami in s 3.0 cm širokim robom, da je dovolj prostora za popravke lektorjev. Najbolje je, da pripravite besedilo v urejevalniku Microsoft Word. Hkrati dostavite odtis članka na papirju, vključno z vsemi slikami in preglednicami ter identično kopijo v elektronski obliki.

Enačbe naj bodo v besedilu postavljene v ločene vrstice in na desnem robu označene s tekočo številko v okroglih oklepajih.

ENOTE IN OKRAJŠAVE

V besedilu, preglednicah in slikah uporabljajte le standardne označbe in okrajšave SI. Simbole fizikalnih

veličin v besedilu pišite poševno (npr. v , T itn.). Simbole enot, ki sestojijo iz črk, pa pokončno (npr. Pa, m itn.).

Vse okrajšave naj bodo, ko se prvič pojavijo, izpisane v celoti.

SLIKE

Slike morajo biti zaporedno oštevilčene in označene, v besedilu in podnaslovu, kot sl. 1, sl. 2 itn. Posnete naj bodo v kateremkoli od razširjenih formatov, npr. BMP, JPG, GIF. Za pripravo diagramov in risb priporočamo CDR format (CorelDraw), saj so slike v njem vektorske in jih lahko pri končni obdelavi preprosto povečujemo ali pomajšujemo.

Pri označevanju osi v diagramih, kadar je le mogoče, uporabite označbe veličin (npr. v , T). V diagramih z več krivuljami mora biti vsaka krivulja označena. Pomen oznake mora biti razložen v podnapisu slike.

Za vse slike po fotografskih posnetkih je treba priložiti izvirne fotografije ali kakovostno narejen posnetek.

PREGLEDNICE

Preglednice morajo biti zaporedno oštevilčene in označene, v besedilu in podnaslovu, kot preglednica 1, preglednica 2 itn. V preglednicah ne uporabljajte izpisanih imen veličin, ampak samo ustrezne simbole. K fizikalnim količinam, npr. t (pisano poševno), pripišite enote (pisano pokončno) v novo vrsto brez oklepajev.

Vse opombe naj bodo označene z uporabo dvignjene številke¹.

SEZNAM LITERATURE

Vsa literatura mora biti navedena v seznamu na koncu članka v prikazani obliki po vrsti za revije, zbornike in knjige:

- [1] Feng, T. W. (2000). Fall-cone penetration and water content relationship of clays. *Geotechnique* 50, No. 2, 181-187.
- [2] Ortolan, Ž. and Mihalinec, Z. (1998). Plasticity index-Indicator of shear strength and a major axis of geotechnical modelling. *Proceedings of the Elev-*

enth Danube-European conference on soil mechanics and geotechnical engineering, Poreč, 25 –29 May 1998.

- [3] Toporišič, J. (1994). *Slovenski pravopis*. 2nd.ed., DZS, Ljubljana.

PODATKI O AVTORJIH

Članku priložite tudi podatke o avtorjih: imena, nazive, popolne poštne naslove, številke telefona in faksa, naslove elektronske pošte. Navedite kontaktno osebo.

SPREJEM ČLANKOV IN AVTORSKE PRAVICE

Uredništvo si pridržuje pravico do odločanja o sprejemu članka za objavo, strokovno oceno mednarodnih recenzentov in morebitnem predlogu za krajšanje ali izpopolnitev ter terminološke in jezikovne korekture.

Avtor mora predložiti pisno izjavo, da je besedilo njegovo izvirno delo in ni bilo v dani obliki še nikjer objavljeno. Z objavo preidejo avtorske pravice na revijo ACTA GEOTECHNICA SLOVENICA. Pri morebitnih kasnejših objavah mora biti AGS navedena kot vir.

Rokopisi člankov ostanejo v arhivu AGS.

Vsa nadaljnja pojasnila daje:

Uredništvo
ACTA GEOTECHNICA SLOVENICA
Univerza v Mariboru
Fakulteta za gradbeništvo
Smetanova ulica 17
2000 Maribor
Slovenija
E-pošta: ags@uni-mb.si

INSTRUCTIONS FOR AUTHORS

The papers are published in English with a translation of the abstract into Slovene.

FORMAT OF THE PAPER

The paper should have the following structure:

- A Title that adequately describes the content of the paper and should not exceed 80 characters;
- An Abstract, which should be viewed as a mini version of the paper and should not exceed 250 words. The Abstract should state the principal objectives and the scope of the investigation and the methodology employed, it should also summarise the results and state the principal conclusions;
- An Introduction, which should provide a review of recent literature and sufficient background information to allow the results of the paper to be understood and evaluated;
- A Theoretical section;
- An Experimental section, which should provide details of the experimental set-up and the methods used for obtaining the results;
- A Results section, which should clearly and concisely present the data using figures and tables where appropriate;
- A Discussion section, which should describe the relationships shown and the generalisations made

possible by the results and discuss the significance of the results, making comparisons with previously published work;

- Conclusions, which should present one or more conclusions that have been drawn from the results and subsequent discussion;
- References, which must be numbered consecutively in the text using square brackets [1] and collected together in a reference list at the end of the paper.

LAYOUT OF THE TEXT

The text should be written in A4 format, with double spacing and margins of 3 cm, to provide editors with space to write in their corrections. Microsoft Word for Windows is the preferred format for submission. One hard copy, including all figures, tables and illustrations and an identical electronic version of the manuscript must be submitted simultaneously.

Equations should be on a separate line in the main body of the text and marked on the right-hand side of the page with numbers in round brackets.

UNITS AND ABBREVIATIONS

Only standard SI symbols and abbreviations should be used in the text, tables and figures. Symbols for physical

quantities in the text should be written in Italics (e.g. v , T , etc.). Symbols for units that consist of letters should be in plain text (e.g. Pa, m, etc.).

All abbreviations should be spelt out in full on first appearance.

FIGURES

Figures must be cited in consecutive numerical order in the text and referred to in both the text and the caption as Fig. 1, Fig. 2, etc. Figures may be saved in any common format, e.g. BMP, JPG, GIF. However, the use of CDR format (CorelDraw) is recommended for graphs and line drawings, since vector images can be easily reduced or enlarged during final processing of the paper.

When labelling axes, physical quantities (e.g. v , T) should be used whenever possible. Multi-curve graphs should have individual curves marked with a symbol; the meaning of the symbol should be explained in the figure caption.

Good quality black-and-white photographs or scanned images should be supplied for illustrations.

TABLES

Tables must be cited in consecutive numerical order in the text and referred to in both the text and the caption as Table 1, Table 2, etc. The use of names for quantities in tables should be avoided if possible: corresponding symbols are preferred. In addition to the physical quantity, e.g. t (in Italics), units (normal text), should be added on a new line without brackets.

Any footnotes should be indicated by the use of the superscript¹.

LIST OF REFERENCES

References should be collected at the end of the paper in the following styles for journals, proceedings and books, respectively:

- [1] Feng, T. W. (2000). Fall-cone penetration and water content relationship of clays. *Geotechnique* 50, No. 2, 181-187.
- [2] Ortolan, Ž. and Mihalinec, Z. (1998). Plasticity index-Indicator of shear strength and a major axis of geotechnical modelling. *Proceedings of the Eleventh Danube-European conference on soil mechanics and geotechnical engineering*, Poreč, 25 -29 May 1998.

- [3] Toporišič, J. (1994). *Slovenski pravopis*. 2nd.ed., DZS, Ljubljana.

AUTHOR INFORMATION

The following information about the authors should be enclosed with the paper: names, complete postal addresses, telephone and fax numbers and E-mail addresses. Indicate the corresponding person.

ACCEPTANCE OF PAPERS AND COPYRIGHT

The Editorial Committee of the Slovenian Geotechnical Review reserves the right to decide whether a paper is acceptable for publication, to obtain peer reviews for submitted papers, and if necessary, to require changes in the content, length or language.

Authors must also enclose a written statement that the paper is original unpublished work, and not under consideration for publication elsewhere. On publication, copyright for the paper shall pass to the ACTA GEOTECHNICA SLOVENICA. The AGS must be stated as a source in all later publication.

Papers will be kept in the archives of the AGS.

For further information contact:

Editorial Board
 ACTA GEOTECHNICA SLOVENICA
 University of Maribor
 Faculty of Civil Engineering
 Smetanova ulica 17
 2000 Maribor
 Slovenia
 E-mail: ags@uni-mb.si

NAMEN REVIJE

Namen revije ACTA GEOTECHNICA SLOVENICA je objavljane kakovostnih teoretičnih člankov z novih pomembnih področij geomehanike in geotehnike, ki bodo dolgoročno vplivali na temeljne in praktične vidike teh področij.

ACTA GEOTECHNICA SLOVENICA objavlja članke s področij: mehanika zemljin in kamnin, inženirska geologija, okoljska geotehnika, geosintetika, geotehnične konstrukcije, numerične in analitične metode, računalniško modeliranje, optimizacija geotehničnih konstrukcij, terenske in laboratorijske preiskave.

Revija redno izhaja dvakrat letno.

AVTORSKE PRAVICE

Ko uredništvo prejme članek v objavo, prosi avtorja(je), da prenese(jo) avtorske pravice za članek na izdajatelja, da bi zagotovili kar se da obsežno razširjanje informacij. Naša revija in posamezni prispevki so zaščiteni z avtorskiimi pravicami izdajatelja in zanje veljajo naslednji pogoji:

fotokopiranje

V skladu z našimi zakoni o zaščiti avtorskih pravic je dovoljeno narediti eno kopijo posameznega članka za osebno uporabo. Za naslednje fotokopije, vključno z večkratnim fotokopiranjem, sistematičnim fotokopiranjem, kopiranjem za reklamne ali predstavitvene namene, nadaljnjo prodajo in vsemi oblikami nedobičkonosne uporabe je treba pridobiti dovoljenje izdajatelja in plačati določen znesek.

Naročniki revije smejo kopirati kazalo z vsebino revije ali pripraviti seznam člankov z izvlečki za rabo v svojih ustanovah.

elektronsko shranjevanje

Za elektronsko shranjevanje vsakršnega gradiva iz revije, vključno z vsemi članki ali deli članka, je potrebno dovoljenje izdajatelja.

ODGOVORNOST

Revija ne prevzame nobene odgovornosti za poškodbe in/ali škodo na osebah in na lastnini na podlagi odgovornosti za izdelke, zaradi malomarnosti ali drugače, ali zaradi uporabe kakršnekoli metode, izdelka, navodil ali zamisli, ki so opisani v njej.

AIMS AND SCOPE

ACTA GEOTECHNICA SLOVENICA aims to play an important role in publishing high-quality, theoretical papers from important and emerging areas that will have a lasting impact on fundamental and practical aspects of geomechanics and geotechnical engineering.

ACTA GEOTECHNICA SLOVENICA publishes papers from the following areas: soil and rock mechanics, engineering geology, environmental geotechnics, geosynthetic, geotechnical structures, numerical and analytical methods, computer modelling, optimization of geotechnical structures, field and laboratory testing.

The journal is published twice a year.

COPYRIGHT

Upon acceptance of an article by the Editorial Board, the author(s) will be asked to transfer copyright for the article to the publisher. This transfer will ensure the widest possible dissemination of information. This review and the individual contributions contained in it are protected by publisher's copyright, and the following terms and conditions apply to their use:

photocopying

Single photocopies of single articles may be made for personal use, as allowed by national copyright laws. Permission of the publisher and payment of a fee are required for all other photocopying, including multiple or systematic copying, copying for advertising or promotional purposes, resale, and all forms of document delivery.

Subscribers may reproduce tables of contents or prepare lists of papers, including abstracts for internal circulation, within their institutions.

electronic storage

Permission of the publisher is required to store electronically any material contained in this review, including any paper or part of the paper.

RESPONSIBILITY

No responsibility is assumed by the publisher for any injury and/or damage to persons or property as a matter of product liability, negligence or otherwise, or from any use or operation of any methods, products, instructions or ideas contained in the material herein.